Title
Development and applications of CRISPR-based functional genomics platforms in human iPSC-derived neurons

Author
Tian, Ruilin

Publication Date
2020

Peer reviewed|Thesis/dissertation

Development and applications of CRISPR-based functional genomics platforms in human iPSC-derived neurons

by
Ruilin Tian

DISSERTATION
Submitted in partial satisfaction of the requirements for degree of
DOCTOR OF PHILOSOPHY

in

Biophysics

in the

GRADUATE DIVISION
of the
UNIVERSITY OF CALIFORNIA, SAN FRANCISCO

Approved:

DocuSigned by:
Martin Kampmann
03BA4012CC044AF...
Martin Kampmann
Chair

DocuSigned by:
Bruce Conklin
[illegible]
Bruce Conklin

DocuSigned by:
Li Gan
4B293EC353444D2...
Li Gan

Committee Members

ACKNOWLEDGEMENTS

I would like to thank my advisor Martin Kampmann for his guidance and support throughout my PhD, for providing me space and opportunities to explore and develop my scientific interests, and for always being encouraging. He is not only a great scientist but also a model mentor. I am very fortunate to work with and learn from him in the past five years.

I would also like to thank all the members past and present in the Kampmann lab for making the lab an amazing place to work in everyday. In particular, I would like to thank Connor Ludwig, Jason Hong and Anthony Abarientos for their tremendous contributions to this project, and Poornima Ramkumar, Xiaoyan Guo, Kun Leng, Emmy Li and Stephanie See for giving me advice and ideas, discussing questions and sharing reagents with me and encouraging me when I was depressed. I would also like to thank Jaime Leong for taking care of my reagents orders, receipts for reimbursement and other logistics so that I can focus on my research.

I would also like to thank my thesis committee members, Li Gan and Bruce Conklin for their invaluable advice and ideas throughout my PhD, and their generous support during my academic job application.

Lastly but most importantly, this dissertation would not have been possible without my family. My parents, Jing Wang and Jinyuan Tian, have always been supportive and encouraging. They came to the US from China to help me take care of my baby so that I could focus on my study. My wife, Ling Zhu, has always been my

biggest cheerleader and a constant source of love. And to my son, David T. Tian, who brings me endless joy and from his eyes I see light.

Chapter 2 is reprinted as it appears in:

Tian, R., Gachechiladze, M. A., Ludwig, C. H., Laurie, M. T., Hong, J. Y., Nathaniel, D., Prabhu, A. V., Fernandopulle, M. S., Patel, R., Abshari, M., Ward, M. E., & Kampmann, M. (2019). CRISPR Interference-Based Platform for Multimodal Genetic Screens in Human iPSC-Derived Neurons. Neuron 104, 239-255.e12.

Author contributions:

R.T., M.A.G., C.H.L., M.E.W., and M.K. contributed to the study's overall conception, design, and interpretation and wrote the manuscript and created the figures with input from the other authors. R.T. designed and conducted the validation screens and CROP-seq screens and designed and conducted computational analyses for all screens (including survival screens, CROP- seq, and longitudinal imaging screens), with guidance from M.K. M.A.G. designed and conducted imaging screens with guidance from M.E.W. and M.K. C.H.L. established CRISPRi in iPSC-derived neurons and designed and conducted the primary screens with guidance from R.T. and M.K. C.H.L. also conducted and analyzed Quant-seq experiments and created the iNeuronRNASeq web application. M.A.G., M.T.L., M.S.F., and R.P. designed, generated, and characterized constructs and cell lines, with guidance from M.E.W. and M.K. J.Y.H. and D.N. generated and characterized con- structs and cell lines, with guidance from R.T. and M.K. A.V.P. contributed to validation experiments and M.A. optimized FACS for iPSC line construction.

Chapter 3 is reprinted as a manuscript in preparation:

Tian, R., Abarientos, A., Hong, J., Yan, R., Xu, K., Kampmann, M. (2020). Genome-wide CRISPRi/a screens in human neurons link lysosomal failure to ferroptosis

Author contributions:

R.T and M.K. designed the project; R.T., A.A., J.H. and R.Y. performed experiments; R.T. analyzed data; R.T. and M.K. wrote the manuscript

Development and applications of CRISPR-based functional genomics platforms in human iPSC-derived neurons

By

Ruilin Tian

ABSTRACT

CRISPR/Cas9-based functional genomics have transformed our ability to elucidate mammalian cell biology. However, most previous CRISPR-based screens were conducted in cancer cell lines rather than healthy, differentiated cells such as neurons. Neurons possess unique cell biological properties that enable them to exert highly specialized physiological functions. To enable systematic characterization of neuronal cell biology, we established CRISPR interference (CRISPRi)- and CRISPR activation (CRISPRa)-based platforms in human neurons derived from induced pluripotent stem cells (iPSCs) that allow robust repression or activation of endogenous genes and large-scale genetic screens in human neurons. Using this toolkit, we performed multiple genome-wide screens to identity genes controlling neuronal survival under unstressed and oxidative stress conditions and genes regulating neuronal redox homeostasis. These screens provide numerous novel biological insights. We also demonstrate that our platforms can be coupled with single-cell RNA sequencing and longitudinal high-content imaging to reveal consequences of genetic perturbations on gene expression and neuronal morphology respectively. Our results highlight the power of unbiased genetic screens in iPSC-derived differentiated cell types and provide a platform for systematic interrogation of normal and disease states of neurons.

TABLE OF CONTENTS

LIST OF FIGURES

LIST OF TABLES

CHAPTER ONE

Introduction

Introduction

The human body comprises hundreds of different cell types. Even though their genomes are nearly identical, cell types are characterized by vastly different cell biologies, enabling them to fulfill diverse physiological functions. Transcriptomic profiling, fueled by recent advances in single-cell- and single-nucleus-RNA sequencing technologies, has revealed cell-type specific gene expression signatures (Gao et al., 2018; Han et al., 2020; Lake et al., 2018; Muraro et al., 2016). In addition to gene expression, gene function can also be cell type-specific, as evidenced by the fact that mutations in broadly expressed or housekeeping genes can lead to strongly cell-type specific defects and disease states. Striking examples are familial mutations causing neurodegenerative diseases, which are often characterized by the selective vulnerability of specific neuronal subtypes, even if the mutated gene is expressed throughout the brain or even throughout the body. Cell-type specific gene function is also supported by our recent finding that knockdown of certain genes can have remarkably different impacts on cell survival and gene expression in different isogenic human cell types, including stem cells and neurons (Tian et al., 2019). Therefore, understanding the function of human genes in different cell types is the next step toward elucidating tissue-specific cell biology and uncovering disease mechanisms.

A powerful approach to functionally annotate the human genome is genetic screening in cultured cells. The robustness of such screens has improved substantially through the recent introduction of CRISPR/Cas9-based approaches. Cas9 nuclease can be targeted by single guide RNAs (sgRNAs) to introduce DNA breaks in coding regions

of genes, which are subsequently repaired by non-homologous end-joining pathways. This process frequently causes short deletions or insertions that disrupt gene function. This CRISPR nuclease (CRISPRn) strategy has enabled genetic screens through the use of pooled sgRNA libraries targeting large numbers of genes (Koike-Yusa et al., 2014; Shalem et al., 2014; Wang et al., 2014; Zhou et al., 2014). We previously developed an alternative platform for loss-of-function screens in mammalian cells based on CRISPR interference (CRISPRi) (Gilbert et al., 2014). In CRISPRi screens, sgRNAs target catalytically dead Cas9 (dCas9) fused to a KRAB transcriptional repression domain to transcription start sites in the genome, thereby inhibiting gene transcription. CRISPRn and CRISPRi screening platforms each have their advantages for specific applications (Kampmann, 2018); (Rosenbluh et al., 2017), but generally yield similar results (Horlbeck et al., 2016). Most previous CRISPR-based screens were implemented in cancer cell lines or stem cells rather than healthy differentiated human cells such as neurons, thereby limiting potential insights into cell type-specific roles of human genes.

To address this need, we developed CRISPRi- and CRISPRa-based platforms for genetic screens in human induced pluripotent stem cell (iPSC)-derived neurons. To our knowledge, this is the first description of a large-scale CRISPR-based screening platform in any differentiated, human iPSC-derived cell type. We focused on neurons as our first application, since functional genomic screens in human neurons have the potential to reveal mechanisms of selective vulnerability in neurodegenerative diseases (Kampmann, 2017) and convergent mechanisms of neuropsychiatric disorders (Willsey

et al., 2018), thus addressing urgent public health issues. iPSC technology is particularly relevant to the study of human neurons, since primary neurons are difficult to obtain from human donors, and non-expandable due to their post-mitotic nature.

We integrated CRISPRi and CRISPRa technologies with our previously described i^{3}Neuron platform (Fernandopulle et al., 2018, Wang et al., 2017), which yields large quantities of highly homogeneous neurons, a prerequisite for robust population-based screens. We decided to use CRISPRi rather than CRISPRn, since CRISPRn-associated DNA damage is highly toxic to iPSCs and untransformed cells (Haapaniemi et al., 2018, Schiroli et al., 2019, Ihry et al., 2018). Furthermore, CRISPRi perturbs gene function by partial knockdown, rather than knockout, thereby enabling the investigation of the biology of essential genes. While large-scale genetic screens in mouse primary neurons have previously been implemented using RNA interference (RNAi) technology (Nieland et al., 2014; Sharma et al., 2013), CRISPRi represents an important advance over RNAi, since it lacks the pervasive off-target effects (Gilbert et al., 2014) inherent to RNAi-based screening approaches (Adamson et al., 2012; Jackson et al., 2003; Kaelin, 2012).

We demonstrate the versatility of our approach in three complementary genetic screens, based on neuronal survival, single-cell RNA sequencing (scRNA-Seq), and neuronal morphology. These screens revealed striking examples of cell-type specific gene functions and identified new genetic modifiers of neuronal biology.

Neurons, as one of the longest-living cell types in the human body, are challenged by various stresses in aging and disease. Due to their post-mitotic nature,

neurons do not have the ability to ‘self-renew’ by cell division. Therefore, robust stress response mechanisms are required for neurons to maintain long-term health. One of the predominant stresses in aging and neurodegenerative diseases is oxidative stress (Barnham et al., 2004; Finkel and Holbrook, 2000), which is induced by excessive accumulation of reactive oxygen species (ROS) in the cell. ROS are highly reactive oxygen-derived molecules that are generated as by-products of normal oxygen metabolism. At low levels, ROS have physiological functions in cellular signaling and activate pro-survival pathways such as MAPK pathways (Kim et al., 2015).

Various antioxidant systems have evolved to control ROS levels and maintain redox homeostasis, including non-enzymatic antioxidants such as vitamin E, vitamin C and glutathione, and enzymatic antioxidants such as superoxide dismutase (SOD), glutathione peroxidases (GPX), peroxiredoxins (PRX) and catalase (Kim et al., 2015). There are also dedicated cellular pathways that sense and respond to ROS levels such as the Keap1-Nrf2 pathway (Sies et al., 2017). An imbalance of ROS production and antioxidant defenses leads to excessive accumulation of ROS, which can cause oxidative damage to proteins, lipids and DNA and ultimately lead to cell death (Kim et al., 2015; Sies et al., 2017). In particular, peroxidation of lipids containing polyunsaturated fatty acids (PUFAs) can cause a non-apoptotic cell death termed ferroptosis, which is iron-dependent (Li et al., 2020).

The brain is highly susceptible to ROS and ferroptosis, due to its high levels of oxygen consumption, abundant redox-active metals such as iron and copper, limited antioxidants and high levels of PUFAs (Patel, 2016). A large body of evidence has

indicated the implications of oxidative stress, iron accumulation and ferroptosis in many neurodegenerative diseases, including Alzheimer's disease (AD), Parkinson's disease (PD) and Amyotrophic Lateral Sclerosis (ALS) (Lin and Beal, 2006; Niedzielska et al., 2016; Rouault, 2013), yet a comprehensive understanding of how neurons regulate redox homeostasis and maintain survival under oxidative stress is lacking.

We applied our functional genomics platforms to systematically identify genetic modifiers of ROS levels, lipid peroxidation, and neuronal survival under oxidative stress. These screens uncovered an unexpected role for prosaposin (*PSAP*), knockdown of which strongly induced ROS and lipid peroxidation levels in neurons and led to neuronal ferroptosis under oxidative stress. We elucidated the underlying mechanism: depletion of PSAP and resulting defects in glycosphingolipids (GSLs) degradation lead to the formation of lipofuscin in the lysosome, which is a hallmark of aged neurons,, driving the accumulation of iron and generation of ROS that oxidize lipids. Intriguingly, the strong phenotypes of PSAP depletion are only presented in neurons, but not iPSCs or HEK293s. These results demonstrate the power of our platforms in uncovering novel cell-type specific human cell biology.

REFERENCES

Adamson, B., Smogorzewska, A., Sigoillot, F.D., King, R.W., and Elledge, S.J. (2012). A genome-wide homologous recombination screen identifies the RNA-binding protein RBMX as a component of the DNA-damage response. Nat. Cell Biol. *14*, 318–328.

Barnham, K.J., Masters, C.L., and Bush, A.I. (2004). Neurodegenerative diseases and oxidative stress. Nat. Rev. Drug Discov. *3*, 205–214.

Fernandopulle, M.S., Prestil, R., Grunseich, C., Wang, C., Gan, L., and Ward, M.E. (2018). Transcription Factor-Mediated Differentiation of Human iPSCs into Neurons. Curr. Protoc. Cell Biol. *79*, e51.

Finkel, T., and Holbrook, N.J. (2000). Oxidants, oxidative stress and the biology of ageing. Nature *408*, 239–247.

Gao, S., Yan, L., Wang, R., Li, J., Yong, J., Zhou, X., Wei, Y., Wu, X., Wang, X., Fan, X., et al. (2018). Tracing the temporal-spatial transcriptome landscapes of the human fetal digestive tract using single-cell RNA-sequencing. Nat. Cell Biol. *20*, 721–734.

Gilbert, L.A., Horlbeck, M.A., Adamson, B., Villalta, J.E., Chen, Y., Whitehead, E.H., Guimaraes, C., Panning, B., Ploegh, H.L., Bassik, M.C., et al. (2014). Genome-scale CRISPR-mediated control of gene repression and activation. Cell *159*, 647–661.

Haapaniemi, E., Botla, S., Persson, J., Schmierer, B., and Taipale, J. (2018).

CRISPR-Cas9 genome editing induces a p53-mediated DNA damage response. Nat. Med. *24*, 927–930.

Han, X., Zhou, Z., Fei, L., Sun, H., Wang, R., Chen, Y., Chen, H., Wang, J., Tang, H., Ge, W., et al. (2020). Construction of a human cell landscape at single-cell level. Nature.

Horlbeck, M.A., Gilbert, L.A., Villalta, J.E., Adamson, B., Pak, R.A., Chen, Y., Fields, A.P., Park, C.Y., Corn, J.E., Kampmann, M., et al. (2016). Compact and highly active next-generation libraries for CRISPR-mediated gene repression and activation. Elife *5*.

Ihry, R.J., Worringer, K.A., Salick, M.R., Frias, E., Ho, D., Theriault, K., Kommineni, S., Chen, J., Sondey, M., Ye, C., et al. (2018). p53 inhibits CRISPR-Cas9 engineering in human pluripotent stem cells. Nat. Med. *24*, 939–946.

Jackson, A.L., Bartz, S.R., Schelter, J., Kobayashi, S.V., Burchard, J., Mao, M., Li, B., Cavet, G., and Linsley, P.S. (2003). Expression profiling reveals off-target gene regulation by RNAi. Nat. Biotechnol. *21*, 635–637.

Kaelin, W.G. (2012). Molecular biology. Use and abuse of RNAi to study mammalian gene function. Science *337*, 421–422.

Kampmann, M. (2017). A CRISPR approach to neurodegenerative diseases. Trends Mol. Med. *23*, 483–485.

Kampmann, M. (2018). Crispri and crispra screens in mammalian cells for precision biology and medicine. ACS Chem. Biol. *13*, 406–416.

Kim, G.H., Kim, J.E., Rhie, S.J., and Yoon, S. (2015). The role of oxidative stress in neurodegenerative diseases. Exp. Neurobiol. *24*, 325–340.

Koike-Yusa, H., Li, Y., Tan, E.-P., Velasco-Herrera, M.D.C., and Yusa, K. (2014). Genome-wide recessive genetic screening in mammalian cells with a lentiviral CRISPR-guide RNA library. Nat. Biotechnol. *32*, 267–273.

Lake, B.B., Chen, S., Sos, B.C., Fan, J., Kaeser, G.E., Yung, Y.C., Duong, T.E., Gao, D., Chun, J., Kharchenko, P.V., et al. (2018). Integrative single-cell analysis of transcriptional and epigenetic states in the human adult brain. Nat. Biotechnol. *36*, 70–80.

Lin, M.T., and Beal, M.F. (2006). Mitochondrial dysfunction and oxidative stress in neurodegenerative diseases. Nature *443*, 787–795.

Li, J., Cao, F., Yin, H.-L., Huang, Z.-J., Lin, Z.-T., Mao, N., Sun, B., and Wang, G. (2020). Ferroptosis: past, present and future. Cell Death Dis. *11*, 88.

Muraro, M.J., Dharmadhikari, G., Grün, D., Groen, N., Dielen, T., Jansen, E., van Gurp, L., Engelse, M.A., Carlotti, F., de Koning, E.J.P., et al. (2016). A Single-Cell Transcriptome Atlas of the Human Pancreas. Cell Syst. *3*, 385-394.e3.

Niedzielska, E., Smaga, I., Gawlik, M., Moniczewski, A., Stankowicz, P., Pera, J., and Filip, M. (2016). Oxidative stress in neurodegenerative diseases. Mol. Neurobiol. *53*, 4094–4125.

Nieland, T.J.F., Logan, D.J., Saulnier, J., Lam, D., Johnson, C., Root, D.E., Carpenter, A.E., and Sabatini, B.L. (2014). High content image analysis identifies novel

regulators of synaptogenesis in a high-throughput RNAi screen of primary neurons. PLoS ONE *9*, e91744.

Patel, M. (2016). Targeting oxidative stress in central nervous system disorders. Trends Pharmacol. Sci. *37*, 768–778.

Rosenbluh, J., Xu, H., Harrington, W., Gill, S., Wang, X., Vazquez, F., Root, D.E., Tsherniak, A., and Hahn, W.C. (2017). Complementary information derived from CRISPR Cas9 mediated gene deletion and suppression. Nat. Commun. *8*, 15403.

Rouault, T.A. (2013). Iron metabolism in the CNS: implications for neurodegenerative diseases. Nat. Rev. Neurosci. *14*, 551–564.

Schiroli, G., Conti, A., Ferrari, S., Della Volpe, L., Jacob, A., Albano, L., Beretta, S., Calabria, A., Vavassori, V., Gasparini, P., et al. (2019). Precise Gene Editing Preserves Hematopoietic Stem Cell Function following Transient p53-Mediated DNA Damage Response. Cell Stem Cell *24*, 551-565.e8.

Shalem, O., Sanjana, N.E., Hartenian, E., Shi, X., Scott, D.A., Mikkelson, T., Heckl, D., Ebert, B.L., Root, D.E., Doench, J.G., et al. (2014). Genome-scale CRISPR-Cas9 knockout screening in human cells. Science *343*, 84–87.

Sharma, K., Choi, S.-Y., Zhang, Y., Nieland, T.J.F., Long, S., Li, M., and Huganir, R.L. (2013). High-throughput genetic screen for synaptogenic factors: identification of LRP6 as critical for excitatory synapse development. Cell Rep. *5*, 1330–1341.

Sies, H., Berndt, C., and Jones, D.P. (2017). Oxidative Stress. Annu. Rev. Biochem. *86*,

715–748.

Tian, R., Gachechiladze, M.A., Ludwig, C.H., Laurie, M.T., Hong, J.Y., Nathaniel, D., Prabhu, A.V., Fernandopulle, M.S., Patel, R., Abshari, M., et al. (2019). CRISPR Interference-Based Platform for Multimodal Genetic Screens in Human iPSC-Derived Neurons. Neuron *104*, 239-255.e12.

Wang, C., Ward, M.E., Chen, R., Liu, K., Tracy, T.E., Chen, X., Xie, M., Sohn, P.D., Ludwig, C., Meyer-Franke, A., et al. (2017). Scalable Production of iPSC-Derived Human Neurons to Identify Tau-Lowering Compounds by High-Content Screening. Stem Cell Reports *9*, 1221–1233.

Wang, T., Wei, J.J., Sabatini, D.M., and Lander, E.S. (2014). Genetic screens in human cells using the CRISPR-Cas9 system. Science *343*, 80–84.

Willsey, A.J., Morris, M.T., Wang, S., Willsey, H.R., Sun, N., Teerikorpi, N., Baum, T.B., Cagney, G., Bender, K.J., Desai, T.A., et al. (2018). The psychiatric cell map initiative: A convergent systems biological approach to illuminating key molecular pathways in neuropsychiatric disorders. Cell *174*, 505–520.

Zhou, Y., Zhu, S., Cai, C., Yuan, P., Li, C., Huang, Y., and Wei, W. (2014). High-throughput screening of a CRISPR/Cas9 library for functional genomics in human cells. Nature *509*, 487–491.

CHAPTER TWO

CRISPR interference-based platform for multimodal genetic screens in human iPSC-derived neurons

INTRODUCTION

While DNA sequencing has provided us with an inventory of human genes, and RNA sequencing is revealing when and where these genes are expressed, the next challenge is to systematically understand the function of human genes in different cell types. A powerful approach to functionally annotate the human genome is genetic screening in cultured cells. The robustness of such screens has improved substantially through the recent introduction of CRISPR/Cas9-based approaches. Cas9 nuclease can be targeted by single guide RNAs (sgRNAs) to introduce DNA breaks in coding regions of genes, which are subsequently repaired by non-homologous end-joining pathways. This process frequently causes short deletions or insertions that disrupt gene function. This CRISPR nuclease (CRISPRn) strategy has enabled genetic screens through the use of pooled sgRNA libraries targeting large numbers of genes (Koike-Yusa et al., 2014; Shalem et al., 2014; Wang et al., 2014; Zhou et al., 2014). We previously developed an alternative platform for loss-of-function screens in mammalian cells based on CRISPR interference (CRISPRi) (Gilbert et al., 2014). In CRISPRi screens, sgRNAs target catalytically dead Cas9 (dCas9) fused to a KRAB transcriptional repression domain to transcription start sites in the genome, thereby inhibiting gene transcription. CRISPRn and CRISPRi screening platforms each have their advantages for specific applications (Kampmann, 2018; Rosenbluh et al., 2017), but generally yield similar results (Horlbeck et al., 2016). Most previous CRISPR-based screens were implemented in cancer cell lines or stem cells rather than healthy differentiated human cells, thereby limiting potential insights into cell type-specific roles of human genes.

Here, we present a CRISPRi-based platform for genetic screens in human induced pluripotent stem cell (iPSC)-derived neurons. To our knowledge, it is the first description of a large-scale CRISPR-based screening platform in any differentiated, human iPSC-derived cell type. We focused on neurons as our first application, since functional genomic screens in human neurons have the potential to reveal mechanisms of selective vulnerability in neurodegenerative diseases (Kampmann, 2017) and convergent mechanisms of neuropsychiatric disorders (Willsey et al., 2018), thus addressing urgent public health issues. iPSC technology is particularly relevant to the study of human neurons, since primary neurons are difficult to obtain from human donors, and non-expandable due to their post-mitotic nature.

We integrated CRISPRi technology with our previously described i^{3}Neuron platform (Fernandopulle et al., 2018; Wang et al., 2017), which yields large quantities of highly homogeneous neurons, a prerequisite for robust population-based screens. We decided to use CRISPRi rather than CRISPRn, since CRISPRn-associated DNA damage is highly toxic to iPSCs and untransformed cells (Haapaniemi et al., 2018; Ihry et al., 2018; Schiroli et al., 2019). Furthermore, CRISPRi perturbs gene function by partial knockdown, rather than knockout, thereby enabling the investigation of the biology of essential genes. While large-scale genetic screens in mouse primary neurons have previously been implemented using RNA interference (RNAi) technology (Nieland et al., 2014; Sharma et al., 2013), CRISPRi represents an important advance over RNAi, since it lacks the pervasive off-target effects (Gilbert et al., 2014) inherent to

RNAi-based screening approaches (Adamson et al., 2012; Jackson et al., 2003; Kaelin, 2012).

We demonstrate the versatility of our approach in three complementary genetic screens, based on neuronal survival, single-cell RNA sequencing (scRNA-Seq), and neuronal morphology. These screens revealed striking examples of cell-type specific gene functions and identified new genetic modifiers of neuronal biology. Our results provide a strategy for systematic dissection of normal and disease states of neurons, and highlight the potential of interrogating human cell biology and gene function in iPSC-derived differentiated cell types.

RESULTS

Robust CRISPR interference in human iPSC-derived neurons

As a first step towards a high-throughput screening platform in neurons, we developed a scalable CRISPRi-based strategy for robust knockdown of endogenous genes in homogeneous populations of human iPSC-derived neurons. We built on our previously described i3Neuron (i3N) platform, which enables large-scale production of iPSC-derived glutamatergic neurons. Central to this platform is an iPSC line with an inducible Neurogenin 2 (*Ngn2*) expression cassette (Zhang et al., 2013) in the AAVS1 safe-harbor locus (Fernandopulle et al., 2018; Wang et al., 2017). To enable stable CRISPRi in iPSC-derived neurons, we generated a plasmid (pC13N-dCas9-BFP-KRAB) to insert an expression cassette for CAG promoter-driven dCas9-BFP-KRAB into the CLYBL safe harbor locus, which enables robust transgene expression throughout neuronal differentiation at higher levels than the AAVS1 locus (Cerbini et al., 2015) (Fig. 2.1A). We then integrated this cassette into our i^{3}N iPSC line, and called the resulting monoclonal line CRISPRi-i^{3}N iPSCs. A normal karyotype was confirmed for CRISPRi-i^{3}N iPSCs (Fig. 2.2A).

To validate CRISPRi activity, we transduced these iPSCs with a lentiviral construct expressing an sgRNA targeting the transferrin receptor gene (TFRC). Knockdown of *TFRC* mRNA was robust in iPSCs and in i3Neurons for several weeks after differentiation (Fig. 2.1B,C). We also validated knockdown of three additional genes, *UBQLN2* (Fig. 2.1D,E), *GRN* (Fig. 2.1F,G) and *CDH2* (Fig. 2.2B) by qRT-PCR,

Western blot, and/or immunofluorescence. Our platform thus enables potent CRISPRi knockdown of endogenous genes in iPSC-derived neurons.

Since CRISPRn-associated DNA damage has been found to be highly toxic to iPSCs (Ihry et al., 2018), we evaluated whether the CRISPRi machinery caused DNA damage in iPSCs or otherwise interfered with neuronal differentiation or activity. We found that expression of CRISPRi machinery and/or sgRNAs did not cause detectable DNA damage (Fig. 2.2C,D), as expected based on the abrogation of nuclease activity in dCas9, and did not affect neuronal differentiation (Fig. 2.2E) or activity as evaluated by calcium imaging (Fig. 2.2F).

We established the CRISPRi-i3N system used throughout this study in the background of the well-characterized WTC11 iPSC line (Miyaoka et al., 2014). In addition, we also generated an equivalent line in the NCRM5 iPSC line (Luo et al., 2014) and validated its CRISPRi activity (Fig. 2.2G).

A pooled CRISPRi screen reveals neuron-essential genes

We then used this platform to identify cell type-specific genetic modifiers of survival in pooled genetic screens in iPSCs and iPSC-derived neurons (Fig. 2.3A). We first transduced CRISPRi-i^{3}N iPSCs with our lentiviral sgRNA library H1 (Horlbeck et al., 2016). The H1 library targets 2,325 genes encoding kinases and other proteins representing the “druggable genome” with at least five independent sgRNAs per gene, plus 500 non-targeting control sgRNAs, for a total of 13,025 sgRNAs. Transduced iPSCs were either passaged for 10 days, or differentiated into neurons by

doxycycline-induced Ngn2 expression. Neurons were collected 14, 21 and 28 days post-induction. Frequencies of cells expressing each sgRNA at each time point were determined by next-generation sequencing of the sgRNA-encoding locus. We observed highly correlated sgRNA frequencies between independently cultured experimental replicates (Fig. 2.4A), supporting the robustness of these measurements.

To analyze the screen results, we developed a new bioinformatics pipeline, MAGeCK-iNC (MAGeCK including Negative Controls, available at kampmannlab.ucsf.edu/mageck-inc). This pipeline integrates a published method, MAGeCK (Li et al., 2014) with aspects of our previous bioinformatics pipeline (Kampmann et al., 2013, 2014) to take full advantage of the non-targeting control sgRNAs in our library when computing P values (see Methods for details). Based on the depletion or enrichment of sgRNAs targeting specific genes at different time points compared to day 0, we identified hit genes for which knockdown was toxic or beneficial to either iPSCs or neurons at different time points (Fig. 2.3B, Fig. 2.4B). We then calculated a knockdown phenotype score and significance P value for each gene (Table S1). The large number of non-targeting sgRNAs in our library enabled us to generate "quasi-genes" from random groupings of non-targeting sgRNAs to empirically estimate a false-discovery rate (FDR) for a given cutoff of hit strength (defined as the product of phenotype score and $-\log_{10}$(P value)), see Methods for details. We defined genes passing an FDR < 0.05 as hit genes. For the majority of hit genes, two or three sgRNAs in the library resulted in strong phenotypes (Fig. 2.4C,D), justifying the use of five sgRNAs/gene in the primary screen library.

Knockdown phenotypes of hit genes were strongly correlated between neurons at different time points, but distinctly less correlated between neurons and iPSCs (Fig. 2.3C). Next, we compared genes that were essential in iPSCs and/or neurons in our screens with “gold-standard” essential genes that were previously identified through genetic screens in cancer cell lines (Hart et al., 2017). This analysis revealed a shared core set of essential genes, as expected, and additional iPSC-specific and neuron-specific essential genes (Fig. 2.3D).

Using Gene Set Enrichment Analysis (GSEA) (Mootha et al., 2003; Subramanian et al., 2005), we found enrichment of distinct groups of survival-related genes in neurons compared to iPSCs, such as genes associated with sterol metabolism (Fig. 2.5A). We validated the strong neuronal dependence on the cholesterol biogenesis pathway pharmacologically using the HMG-CoA reductase inhibitor mevastatin (Fig. 2.3E) and found that CRISPRi knockdown of HMG-CoA reductase (HMGCR) can be partially rescued by supplementing its product mevalonate (Fig. 2.3F).

We determined expression levels of genes at different time points during neuronal differentiation by Quant-Seq (Data deposited in GEO, GSE124703; the results can be visualized at kampmannlab.ucsf.edu/ineuron-rna-seq). As a group, neuron-essential genes were expressed at significantly higher levels than non-essential genes in iPSC-derived neurons (one-sided Mann-Whitney U test, Fig. 2.5B). The vast majority of neuron-essential genes were detectable at the transcript level, further supporting the specificity of our screen results.

Intriguingly, we identified several genes that specifically enhanced neuronal survival when knocked down, including *MAP3K12* (encoding dual leucine zipper kinase DLK), *MAPK8* (encoding Jun kinase JNK1), *CDKN1C* (encoding the cyclin-dependent kinase inhibitor p57) and *EIF2AK3* (encoding the eIF2alpha kinase PERK) (Table S1). A pathway involving DLK, JNK and PERK has previously been implicated in neuronal death (Ghosh et al., 2011; Huntwork-Rodriguez et al., 2013; Larhammar et al., 2017; Miller et al., 2009; Pozniak et al., 2013; Watkins et al., 2013; Welsbie et al., 2013), validating our approach.

In summary, our large-scale CRISPRi screen in human iPSC-derived neurons uncovered genes that control the survival of neurons, but not cancer cells or iPSCs, demonstrating the potential of our platform to characterize the biology of differentiated cell types.

Pooled validation of hit genes

To validate and further characterize hit genes from the primary large-scale screen, we performed a series of secondary screens. For this purpose, we generated a new lentiviral sgRNA plasmid (pMK1334) that enables screens with single-cell RNA-Seq (scRNA-Seq) readouts (based on the CROP-Seq format (Datlinger et al., 2017)), and high-content imaging readouts (expressing a bright, nuclear-targeted BFP) (Fig. 2.6A). We individually cloned 192 sgRNAs into this plasmid (184 sgRNAs targeting 92 different hit genes with two sgRNAs per gene and eight non-targeting control sgRNAs). Then, to confirm essential genes identified in our primary screen, we pooled these plasmids and

conducted a survival-based validation screen (Fig. 2.6A). Because the library size was small compared to the primary screen, we obtained a high representation of each sgRNA in the validation screen. As in the primary screen, CRISPRi-i^{3}N iPSCs transduced with the plasmid pool were either passaged as iPSCs or differentiated into glutamatergic neurons, and then harvested at different time points for next-generation sequencing and calculation of survival phenotypes for each sgRNA (Table S2). We observed a high correlation of raw sgRNA counts between two independently differentiated biological replicates ($R2 > 0.9$, Fig. 2.6B), supporting the robustness of phenotypes measured in the pooled validation screen. We then compared the results from the validation screen with those from the primary screen. In both iPSCs and neurons, all positive hits and most of the negative hits from the primary screen were confirmed in the validation screen (Fig. 2.6C). These findings indicate that hits identified in the primary screen are highly reproducible.

In the brain, many neuronal functions are supported by glial cells, particularly astrocytes. To rule out the possibility that hits from the primary screen were artifacts of an astrocyte-free culture environment, we included an additional condition in the validation screen, in which neurons were co-cultured with primary mouse astrocytes. Neuronal phenotypes in the presence or absence of astrocytes were highly correlated (Fig. 2.6D,E and Fig. 2.8A), indicating that the vast majority of the neuron-essential genes we identified are required even in the presence of astrocytes. However, we identified a small number of genes, including *PPCDC*, *UROD* and *MAT2A*, for which knockdown was less toxic in the presence of astrocytes (Fig. 2.6F). This suggests that

astrocytes may compensate for the loss of function for these genes in neurons. We also identified a small number of other genes, including *MMAB*, *UBA1* and *PPP2R2A*, for which knockdown was more toxic in the presence of astrocytes (Fig. 2.6F). These genes may function in pathways affected by crosstalk between neurons and astrocytes.

Inducible CRISPRi distinguishes neuronal differentiation and survival phenotypes

A caveat of our primary screen is that we introduced the sgRNA library into cells constitutively expressing CRISPRi machinery at the iPSC stage. Therefore, some hit genes detected in the primary screen may play a role in neuronal differentiation rather than neuronal survival. To explore this possibility, we developed a system to allow independent control of neuronal differentiation and CRISPRi activity. We generated inducible CRISPRi constructs by tagging the CRISPRi machinery (dCas9-BFP-KRAB) with dihydrofolate reductase (DHFR) degrons. In the absence of the small molecule trimethoprim (TMP), these DHFR degrons cause proteasomal degradation of fused proteins. Addition of TMP counteracts degradation (Iwamoto et al., 2010). Our initial construct contained a single N-terminal DHFR degron (Fig. 2.8B), which was insufficient to fully suppress CRISPRi activity in the absence of TMP (Fig. 2.8C). Therefore, we generated another plasmid (pRT029) with DHFR degrons on both the N- and C-termini of dCas9-BFP-KRAB (Fig. 2.8G). This dual-degron CRISPRi construct was then integrated into the CLYBL locus of i3N-iPSCs. In the absence of TMP, the double-degron construct had no CRISPRi activity in iPSCs or neurons (Fig. 2.8D). TMP addition starting at the iPSC stage resulted in robust CRISPRi activity in iPSCs and

neurons (Fig. 2.8D), and TMP addition starting at the neuronal stage resulted in moderate CRISPRi activity (Fig. 2.8E). While future optimization of the inducible CRISPRi construct will be necessary, these results indicate that temporal regulation of CRISPRi activity can be achieved in iPSCs and differentiated neurons.

We used the inducible CRISPRi platform to determine if hit genes from our primary screen were related to neuronal survival or differentiation. iPSCs expressing the dual-degron construct were transduced with the pooled validation sgRNA library. Cells were then cultured under three different conditions, including no TMP, TMP added starting at the iPSC stage, and TMP added at the neuronal stage (Fig. 2.6H). In the population cultured without TMP, none of the sgRNAs showed strong phenotypes compared to cells to which TMP was added at the iPSC stage (Fig. 2.6I), confirming the tight control of the inducible system. To determine if any of the neuron-essential genes identified in our primary screen were in actuality required for differentiation, we compared neurons in which knockdown was induced either at the iPSC stage or later at the neuronal stage of the protocol. Phenotypes observed in these two conditions were highly correlated ($r = 0.98$, Fig. 2.6J), indicating that the vast majority of hits identified from the original screen are indeed essential for neuronal survival, rather than differentiation (Fig. 2.6H).

Interestingly, there was one exception: sgRNAs targeting *PPP1R12C* were strongly enriched when TMP was added at the iPSC stage, but this phenotype was substantially weaker when TMP was added at the neuron stage. Based on this finding, we hypothesized that these sgRNAs may interfere with neuronal differentiation. Indeed,

we observed that two independent sgRNAs targeting *PPP1R12C* each caused continued proliferation instead of neuronal differentiation in a subset of iPSCs (Fig. 2.8F,G), providing an explanation for the enrichment of cells expressing *PPP1R12*C-targeted sgRNAs in the primary screen. Thus, our inducible CRISPRi approach successfully uncovered a false-positive hit from the primary screen, which affected differentiation as opposed to neuronal survival. Interestingly, the AAVS1 locus, into which the inducible Ngn2 transgene was integrated, resides within the *PPP1R12C* gene. An open question remains as to whether *PPP1R12C* plays a role in neuronal differentiation, or whether sgRNAs directed against *PPP1R12C* interfered with doxycycline-mediated induction of Ngn2.

Taken together, these pooled validation screens confirmed that hits from the primary screen were highly reproducible and that we were able to identify genes specifically essential for neuronal survival.

CROP-Seq generates mechanistic hypotheses for genes controlling neuronal survival

Recently developed strategies to couple CRISPR screening to scRNA-Seq readouts yield rich, high-dimensional phenotypes from pooled screens (Adamson et al., 2016; Datlinger et al., 2017; Dixit et al., 2016). As a first step towards understanding the mechanisms by which hit genes affect the survival of iPSCs and neurons, we investigated how gene knockdown altered transcriptomes of single cells (Fig. 2.7A). We selected 27 genes that exemplified different categories of hits based on their pattern of

survival phenotypes in iPSCs and neurons (Fig. 2.6E). A pool of 58 sgRNAs (two sgRNAs targeting each selected gene and four non-targeting control sgRNAs) in the secondary screening plasmid pMK1334 (Fig. 2.6A) was transduced into CRISPRi-i3N iPSCs. We used the 10x Genomics platform to perform scRNA-Seq of ~ 20,000 iPSCs and 20,000 Day 7 neurons. We chose to monitor transcriptomic effects of hit gene knockdown at the early Day 7 time point to capture earlier, gene-specific effects of knockdown, as opposed to later nonspecific effects reflecting toxicity. Transcripts containing sgRNA sequences were further amplified to facilitate sgRNA identity assignment, adapting a previously published strategy (Hill et al., 2018). Following sequencing, transcriptomes and sgRNA identities were mapped to individual cells (Data deposited in GEO, GSE124703). High data quality was evident from the mean reads per cell (~84,000 for iPSCs, ~91,000 for neurons), the median number of genes detected per cell (~5,000 for iPSCs, ~4,600 for neurons) and the number of cells to which a unique sgRNA could be assigned after quality control (~15,000 iPSCs, ~8,400 neurons). Based on the expression of canonical marker genes, we excluded the possibility that gene knockdown interfered with differentiation to glutamatergic neurons (Fig. 2.9A).

Next, we examined the transcriptomes of groups of cells expressing a given sgRNA (which we refer to as “sgRNA groups”). In both iPSCs and neurons, the two sgRNA groups expressing sgRNAs targeting the same gene tended to form clusters in t-Distributed stochastic neighbor embedding (tSNE) plots (Fig. 2.9B), confirming that independent sgRNAs targeting the same gene had highly similar phenotypic

consequences. The extent of gene knockdown varied across cells within an sgRNA group and between the two sgRNAs targeting the gene. Given that many genes selected for the CROP-Seq screen are essential, it is likely that cells with lower levels of knockdown had a survival advantage and are enriched in the sequenced population. To characterize phenotypes in cells with the most stringent gene knockdown, we took advantage of the single-cell resolution of the CROP-Seq data to select the top 50% of cells with the best on-target knockdown for each gene for further analysis. We refer to this group of cells as the "gene knockdown group". Compared to cells with non-targeting sgRNAs, the expression levels of the targeted genes in a gene knockdown group were greatly repressed (Fig. 2.7B). For most genes (24/27 in iPSCs, 18/27 in neurons) knockdown levels of greater than 80% were achieved. Together, these findings further support the robustness of CRISPRi knockdown and of the transcriptomic phenotypes determined by our modified CROP-Seq platform.

To characterize how gene knockdown altered transcriptomes of iPSCs and neurons, we performed differential expression analysis between gene knockdown groups and the negative control group (Table S3). While knockdown of some genes induced the expression of cell-death related genes (including *PDCD2*, *AEN*, *GADD45A* and *ATF3*), no generic signature of dying cells dominated the differentially expressed genes. Rather, knockdown of different genes resulted in gene-specific transcriptomic signatures (Fig. 2.7C). By clustering gene knockdown groups based on the signature of differential gene expression, we found transcriptomic signatures associated with knockdown of functionally related genes (Fig. 2.7C). For some genes, knockdown

resulted in upregulation of functionally related genes. For example, knockdown of genes involved in cholesterol and fatty acid biosynthesis, including *HMGCS1, HMGCR, PMVK, MVK, MMAB,* and *HACD2,* caused induction of other genes in the same pathway (Fig. 2.7C, Table S3). Thus, pooled CROP-Seq screens can identify and group functionally related genes in human neurons.

The CROP-Seq screen also generated mechanistic hypotheses. For example, knockdown of MAP3K12 specifically improved neuronal survival. Signaling by the *MAP3K12*-encoded kinase DLK was previously implicated in neuronal death and neurodegeneration (Ghosh et al., 2011; Huntwork-Rodriguez et al., 2013; Larhammar et al., 2017; Miller et al., 2009; Pozniak et al., 2013; Watkins et al., 2013; Welsbie et al., 2013). In our screen, knockdown of *MAP3K12* resulted in coherent changes in neuronal gene expression (Fig. 2.10A and Table S3). Ribosomal genes and the anti-apoptotic transcription factor Brn3a (encoded by *POU4F1*) were upregulated.

Conversely, we observed downregulation of the pro-apoptotic BCL-2 protein Harakiri/DP5 (encoded by *HRK*), the neurodegeneration-associated amyloid precursor protein (*APP*), and the pro-apoptotic transcription factor JUN, which is also a downstream signaling target of DLK (Welsbie et al., 2013). Furthermore, *MAP3K12* knockdown caused downregulation of a vast array of proteins involved in cytoskeletal organization, and upregulation of specific synaptotagmins, which act as calcium sensors in synaptic vesicles. These changes in gene expression may relate to the function of DLK in synaptic terminals and its reported role as a neuronal sensor of cytoskeletal damage (Valakh et al., 2015). Lastly, *MAP3K12* knockdown induced expression of

neuritin (NRN1), a neurotrophic factor associated with synaptic plasticity and neuritogenesis (Cantallops et al., 2000; Javaherian and Cline, 2005; Naeve et al., 1997; Yao et al., 2016). Intriguingly, neuritin levels are decreased in Alzheimer's Disease patient brains, and overexpression of neuritin was found to be protective in a mouse model of Alzheimer's Disease (Choi et al., 2014). Thus, CROP-Seq provides a wealth of testable hypotheses for neuroprotective mechanisms and specific effectors downstream of DLK/MAP3K12 inhibition.

CROP-Seq reveals neuron-specific transcriptomic consequences of gene knockdown

The results from our parallel CROP-Seq screens in iPSCs and neurons enabled us to compare transcriptomic consequences of gene knockdown across both cell types (Fig. 2.9C). Interestingly, only a few genes, including *SQLE, MMAB, MVK, UQCRQ,* and *ATP5B*, showed high similarity (similarity score > 0.15) in the transcriptomic changes they induced in iPSCs versus neurons. Knockdown of most genes induced distinct transcriptomic responses in the two cell types. This suggests that either gene knockdown caused different stress states in the two cell types or that gene regulatory networks are wired differently in iPSCs and iPSC-derived neurons.

To further dissect these cell type-specific phenotypes, we ranked genes by the similarity of their knockdown phenotypes in iPSCs and neurons with respect to survival and transcriptomic response (Fig. 2.9D). For some genes, both survival and transcriptomic phenotypes were similar in iPSCs and neurons. An example for this

category of genes is *UQCRQ*, which encodes a component of the mitochondrial complex III in the electron transport chain. *UQCRQ* is essential in both cell types (Fig. 2.10B), and knockdown of *UQCRQ* had similar transcriptomic consequences in both iPSCs and neurons – upregulation of mitochondrially encoded electron transport chain components and of ribosomal proteins (Fig. 2.10C, Table S3). Similarly, knockdown of cholesterol and fatty acid biosynthesis genes induced expression of other cholesterol and fatty acid biosynthesis genes in both iPSCs and neurons (Fig. 2.7C, Table S3).

Interestingly, we also found examples of genes that were essential in both neurons and iPSCs, yet caused substantially different transcriptomic phenotypes when knocked down (Fig. 2.9D). For example, knockdown of the essential E1 ubiquitin activating enzyme, *UBA1* (Fig. 2.10B) caused neuron-specific induction of a large number of genes (Fig. 2.10D, Table S3), including those encoding heat shock proteins (cytosolic chaperones HSPA8 and HSPB1 and endoplasmic reticulum chaperones HSPA5 and HSP90B1). This suggests that compromised UBA1 function triggered a broad proteotoxic stress response in neurons, but not iPSCs, consistent with the role of UBA1 in several neurodegenerative diseases (Groen and Gillingwater, 2015). Thus, even ubiquitously expressed housekeeping genes can play distinct roles in different cell types.

Lastly, we discovered that some genes differed with respect to both survival and transcriptomic phenotypes in neurons and iPSCs (Fig. 2.9D). This was expected for genes predominantly expressed in neurons, such as *MAP3K12* (Fig. 2.10A). However, we also found examples of genes in which knockdown had strikingly different

transcriptomic consequences in neurons and iPSCs despite high expression in both cell types. Such a gene is *MAT2A*, encoding methionine adenosyl transferase 2a, which catalyzes the production of the methyl donor S-adenosylmethionine (SAM) from methionine and ATP (Fig. 2.11A). *MAT2A* is essential in neurons, but not iPSCs (Fig. 2.11B). Knockdown of *MAT2A* in iPSCs did not substantially affect the expression of any gene other than *MAT2A* itself (Fig. 2.11C). In neurons, however, knockdown of *MAT2A* caused differential expression of thousands of genes (Fig. 2.11D, Table S3). Genes downregulated in neurons in response to *MAT2A* knockdown were enriched for neuron-specific functions (Fig. 2.11E), providing a possible explanation for the neuron-selective toxicity of *MAT2A* knockdown.

In summary, results from CROP-Seq screens in iPSCs and iPSC-derived neurons further highlight differences in gene function across the two cell types, provide rich insights into consequences of gene knockdown, and generate mechanistic hypotheses. They further support the idea that it is critically important to study gene function in relevant cell types, even for widely expressed genes.

An arrayed CRISPRi platform for rich phenotyping by longitudinal imaging

While pooled genetic screens are extremely powerful due to their scalability, many cellular phenotypes cannot be evaluated using a pooled approach. Such phenotypes include morphology, temporal dynamics, electrophysiological properties, and non-cell-autonomous phenotypes. To expand the utility of our screening platform, we therefore optimized an arrayed CRISPRi platform for iPSC-derived neurons.

As a proof-of-concept arrayed screen, we established a longitudinal imaging platform to track the effect of knocking down selected hit genes from our primary screen on neuronal survival and morphology over time. First, we stably expressed cytosolic mScarlet (for neurite tracing) and nuclear-localized mNeon-Green (for survival analysis) in CRISPRi-i3N iPSCs. Then, we infected these iPSCs in multi-well plates with lentiviral preparations encoding 48 individual sgRNAs (23 genes selected from the gene set from the CROP-Seq screen targeted by two sgRNAs each, and two non-targeting sgRNAs), followed by puromycin selection and longitudinal imaging of iPSCs, or neuronal differentiation. After three days, we re-plated pre-differentiated neurons on 96-well plates alongside similarly prepared cells that did not express sgRNAs or the cytosolic mScarlet marker at a 1:20 ratio to allow more accurate tracing of mScarlet-expressing neurons. These plates were then longitudinally imaged every few days using an automated microscope with a large area of each well imaged at each time point, allowing us to re-image the same populations of neurons over time (Fig. 2.12A, Movies S3, S4).

We developed an automated image analysis pipeline to segment neuronal cell bodies and neurites (Fig. 2.12B). By tracking cell numbers over time, we could measure neuronal survival and iPSC proliferation (Fig. 2.12C,D). Quantification of survival based on longitudinal imaging was robust across independent experiments (Fig. 2.13A). Three individual sgRNAs were so toxic that they prevented longitudinal imaging, and were removed from further analysis. As anticipated, the vast majority of sgRNAs that altered survival in pooled screens also altered survival in our arrayed longitudinal survival

analysis (Fig. 2.12D). However, longitudinal imaging provided additional information on the timeline of toxicity caused by knockdown of different genes and revealed gene-specific temporal patterns (Fig. 2.12D,E).

We then analyzed the effect of gene knockdown on neurite morphology. Our neurite segmentation algorithm extracted multiple morphology metrics, including neurite length, number of neurite trunks and neurite branching (Fig. 2.12B,C). Our longitudinal imaging approach also enabled us to evaluate adverse effects of the expression of CRISPRi machinery and/or non-targeting sgRNA using highly sensitive readouts. We found that neither CRISPRi machinery nor non-targeting sgRNAs affected neuronal survival (Fig. 2.13B) or neurite growth (Fig. 2.13C).

Surprisingly, knockdown of genes that we selected based on their impact on neuronal survival also had distinct effects on neuronal morphology (Fig. 2.12C,F). Knockdown of the geranylgeranyltransferase *PGGT1B* promoted both neurite growth and branching, consistent with previous findings that protein prenylation inhibits axon growth (Li et al., 2016). Neurite length and the number of neurite trunks were under independent genetic control (Fig. 2.12G).

Taken together, the profile of features extracted from our imaging platform was so information-rich and gene-specific that hierarchical clustering of individual sgRNAs based on these features led to co-clustering of the two sgRNAs targeting a given gene for the majority of genes (Fig. 2.12E). Conceptually, knockdown phenotypes of specific genes occupy distinct regions in a high-dimensional neuronal morphology space (Fig. 2.12E,G).

In combination with survival-based and CROP-Seq screens, our arrayed high-content CRISPRi platform will enable the deep characterization of gene function in a plethora of human cell types.

DISCUSSION

Here, we describe a platform for large-scale, multimodal CRISPRi-based genetic screens in human iPSC-derived neurons. While CRISPR screens in cancer cells and stem cells have revealed numerous biological insights, we reasoned that screens in differentiated, non-cancerous cell types could elucidate novel, cell-type specific gene functions. Indeed, our survival screens uncovered genes that were essential for neurons, but not iPSCs or cancer cells. We also found that knockdown of some broadly-expressed housekeeping genes, such as UBA1, caused strikingly distinct transcriptomic phenotypes in neurons compared to iPSCs, consistent with the idea that gene functions can vary across distinct cell types. Lastly, our arrayed screening platform uncovered gene-specific effects on longitudinal survival and neuronal morphology. These proof-of-concept screens have generated a wealth of phenotypic data, which will provide a rich resource for further analysis and the generation of mechanistic hypotheses.

The combination of CRISPRi functional genomics and iPSC-derived neuron technology leverages the strengths of both approaches. Neurons are a highly specialized and disease-relevant cell type, and thus it is crucial to study certain human gene functions in these cells. However, primary human neurons cannot readily be obtained in the quantities and homogeneity needed for large-scale screens. By contrast, human iPSCs have several fundamental qualities ideally suited for screens. They can be made from readily available cells, such as skin fibroblasts or peripheral mononuclear

blood cells; they can be genetically engineered and subsequently expanded to generate large numbers of isogenic cells; and they can then be differentiated into a variety of cell types, including specific neuronal subtypes. Differentiation protocols based on induced expression of transcription factors are particularly useful for screens, as they are rapid and yield large numbers of homogeneous neurons. In addition to the Ngn2-driven generation of glutamatergic neurons (Fernandopulle et al., 2018; Wang et al., 2017; Zhang et al., 2013) used here, induced expression of different transcription factors yield other types of neurons, such as motor neurons (Hester et al., 2011; Shi et al., 2018) and inhibitory neurons (Yang et al., 2017). Systematic screens are beginning to uncover additional combinations of transcription factors driving specific neuronal fates (Liu et al., 2018; Tsunemoto et al., 2018). Thus, iPSC technology could be used to generate different neuron types from an isogenic parental cell line, which would facilitate parallel CRISPR screens to dissect neuronal subtype specific gene function. Such screens will address fundamental questions in neuroscience, such as why specific neuronal subtypes are selectively vulnerable in neurodegenerative diseases (Kampmann, 2017). Furthermore, genetic modifier screens in neurons derived from patient iPSCs and isogenic controls have the potential to uncover new disease mechanisms. These discoveries may, in turn, yield new therapeutic strategies to correct cellular defects linked to disease genes. Despite their usefulness, iPSC-derived neurons have limitations – in particular, they do not fully recapitulate all features of mature (or aging) neurons in the human brain. We anticipate that functional genomics approaches, such

as ours, may hold the key to improving protocols that lead to ever more faithful models of mature human neurons.

CRISPRi is particularly well suited as a method to study gene function in iPSC-derived neurons, for several reasons. First, it does not cause DNA damage (Fig. 2.2C,D), and thus lacks the non-specific p53-mediated toxicity observed with CRISPRn approaches in iPSCs and untransformed cells (Haapaniemi et al., 2018; Ihry et al., 2018). Second, it is inducible and reversible (Gilbert et al., 2014), enabling the time-resolved dissection of human gene function. Third, it perturbs gene function via partial knockdown, as opposed to knockout, thereby enabling functional characterization of essential genes, as demonstrated in this study.

There are several areas for further development of our platform. Further optimization of inducible CRISPRi will result in more potent gene repression in mature neurons, leading to increased sensitivity. The standard use of inducible CRISPRi would be preferable in order to initiate gene perturbation in the differentiated cell state, thereby avoiding false-positive phenotypes due to interference with the differentiation process. Also, establishment of our CRISPR activation (CRISPRa) approach in iPSC-derived neurons will enable gain-of-function genetic screens, which yield complementary insights to CRISPRi loss-of-function screens (Gilbert et al., 2014). Finally, using synthetic sgRNAs instead of lentivirus in arrayed CRISPRi screens would substantially increase scalability.

We anticipate that the technology described here can be broadly applied to include additional neuron-relevant readouts, such as multi-electrode arrays (to measure

electrophysiological properties) and brain organoids (to assay interactions of neurons with other cell types). However, our technology is not limited to neurons, and should provide a paradigm for investigating the specific biology of numerous other types of differentiated cells. Parallel genetic screens across the full gamut of human cell types cells may systematically uncover context-specific roles of human genes, leading to a deeper mechanistic understanding of how they control human biology and disease.

FIGURES

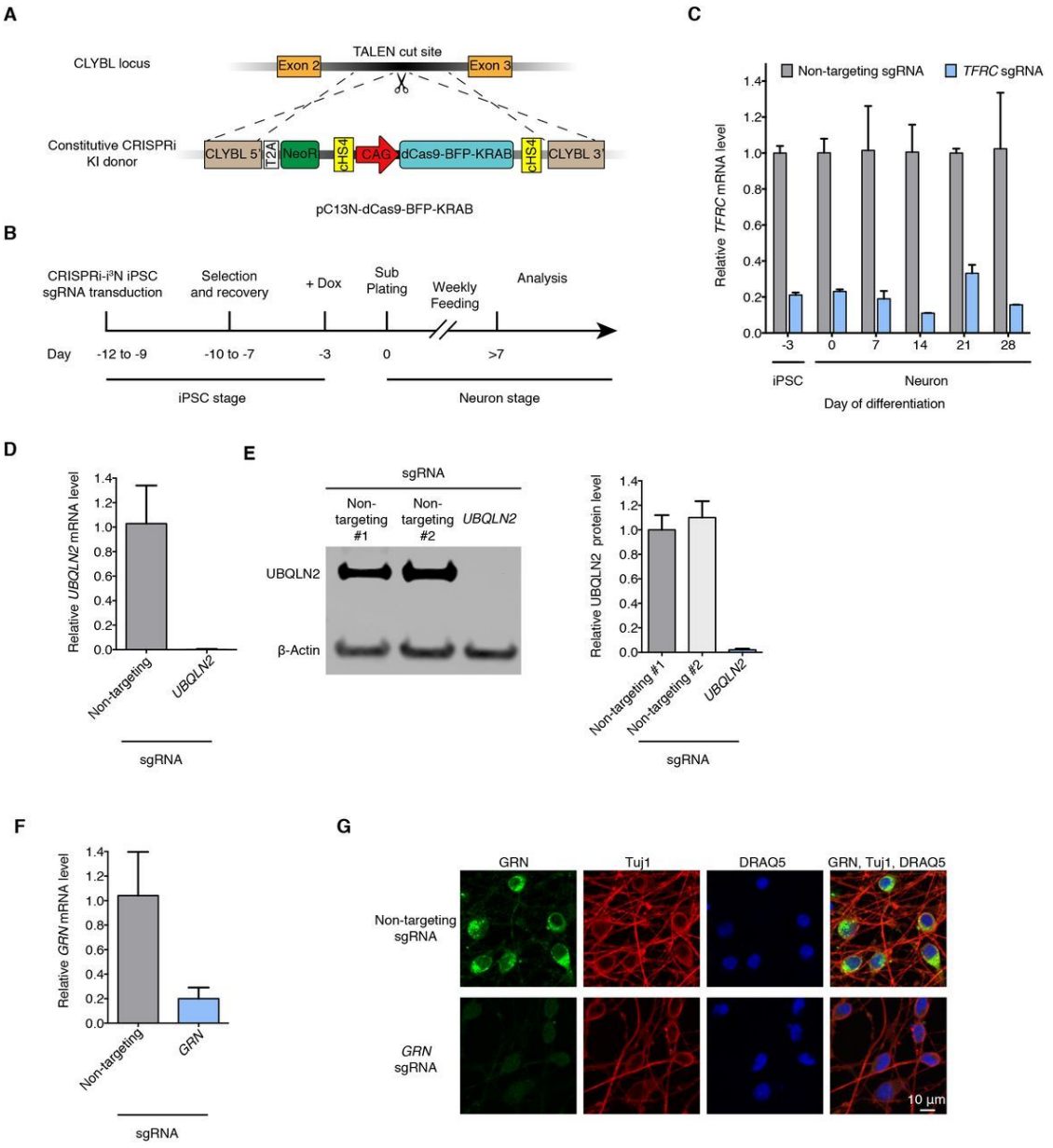

Fig. 2.1. Durable gene knockdown by CRISPR interference in human iPSC-derived neurons

(A) Construct pC13N-dCas9-BFP-KRAB for the expression of CRISPRi machinery from the CLYBL safe-harbor locus: catalytically dead Cas9 (dCas9) fused to blue fluorescent protein (BFP) and the KRAB domain, under the control of the constitutive CAG promoter.

(B) Timeline for sgRNA transduction, selection and recovery, doxycycline-induced neuronal differentiation and functional analysis of CRISPRi-i3N iPSCs.

(C) Knockdown of the transferrin receptor (TFRC) in CRISPRi-i3N iPSCs and neurons. CRISPRi-i3N iPSCs were lentivirally infected with an sgRNA targeting TFRC or a non-targeting negative control sgRNA. Neuronal differentiation was induced by addition of doxycycline on Day −3 of the differentiation protocol and plating cells in neuronal medium on Day 0. Cells were harvested at different days for qPCR. After normalizing by GAPDH mRNA levels, ratios of TFRC mRNA were calculated for cells expressing the TFRC-targeting sgRNA versus the non-targeting sgRNA; mean ± SD (two biological replicates).

(D, E) Knockdown of ubiquilin 2 (UBQLN2) in CRISPRi-i3N neurons. CRISPRi-i3N neurons infected with UBQLN2 sgRNA or non-targeting control sgRNA were harvested on Day 11 for qPCR (D) or Western blot (E) to quantify UBQLN2 knockdown at the mRNA level or protein level, respectively. (D) Relative UBQLN2 mRNA level was determined by normalizing UBQLN2 mRNA level by GAPDH. Relative UBQLN2 mRNA was calculated for cells expressing the UBQLN2-targeting sgRNA versus the non-targeting sgRNA; mean ± SD (three biological replicates). (E) Left, representative Western blot (Loading control β-Actin). Right, quantification of UBQLN2 protein levels normalized by β-Actin for cells with non-targeting sgRNAs or UBQLN2 sgRNA; mean ± SD (two independent Western blots).

(F,G) Knockdown of progranulin (GRN) in CRISPRi-i3N neurons. CRISPRi-i3N neurons infected with GRN sgRNA or non-targeting control sgRNA were harvested on Day 11 for qPCR (F) or monitored by immunofluorescence (IF) microscopy on Day 5. (G) Relative GRN mRNA level normalized by GAPDH mRNA. Ratio of relative GRN mRNA for cells expressing the GRN-targeting sgRNA versus the non-targeting sgRNA; mean ± SD (three biological replicates). (G) Top row, non-targeting negative control sgRNA. Bottom row, sgRNA targeting progranulin. Progranulin signal (IF, green), neuronal marker Tuj1 (IF, red) and nuclear counterstain DRAQ5 (blue) are shown.

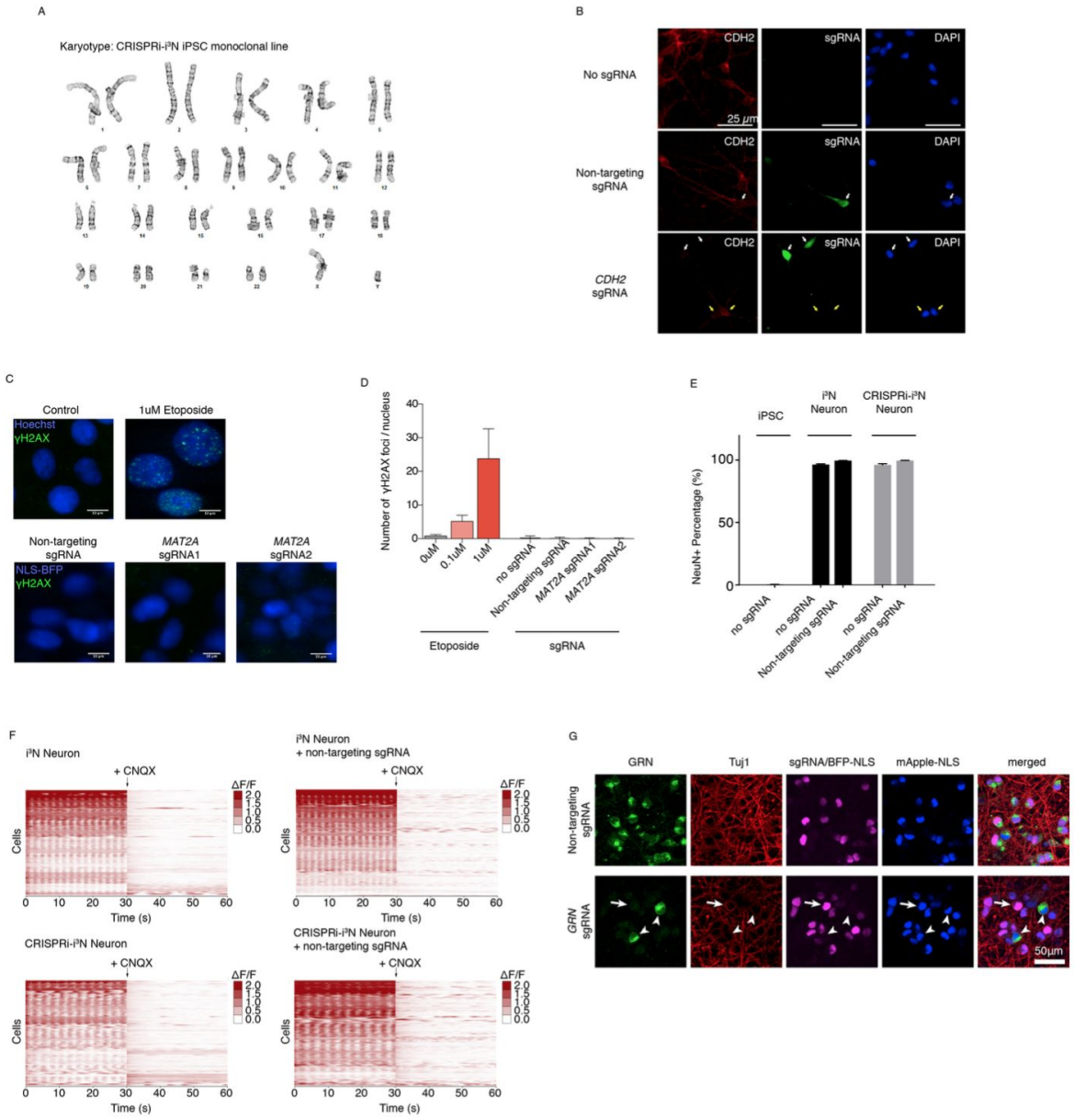

Figure 2.2. Normal karyotype, neuronal differentiation and activity and CRISPRi activity of the CRISPRi- i3N iPSC monoclonal line
(A) Karyotyping of the monoclonal CRISPRi- i3N iPSC line confirmed a normal male karyotype.

(B) Knockdown of N-cadherin (CDH2) in iPSC-derived neurons on Day 18 monitored on the protein level by immunofluorescence (IF) microscopy. White arrows mark cells infected with a lentiviral plasmid expressing an sgRNA and GFP (green). Top row, uninfected cells. Middle

row, non-targeting negative control sgRNA. N-cadherin signal (IF, red) is similar in infected and uninfected cells. Bottom row, sgRNA targeting N-cadherin (CDH2). For the infected cells (white arrows), N-cadherin signal (IF, red) is substantially reduced compared with neighboring uninfected cells (yellow arrows). Nuclear counterstain DAPI is shown in blue.

(C,D) DNAdamagedetectedbyγH2AXstaining.CRISPRi-i3NiPSCstreatedwithvehicleor 1μM etoposide for 6 hours or infected with non-targeting sgRNA or two different MAT2A sgRNAs for 48 hours were fixed and immunostained using an γH2AX antibody. (C) Representative images of γH2AX staining (Green). γH2AX foci can be observed in cells treated with etoposide, but not in cells with no treatment or with sgRNAs. Nuclei are visualized by Hoechst stain (top row, control and etoposide treatment) or NLS-BFP (bottom row, sgRNAs). (D) Quantification of the number of γH2AX foci per nucleus using CellProfiler. Mean and standard deviations for 6 replicates wells are shown.

(E) Quantification of the percentage of NeuN positive cells in i3N iPSCs, i3N neurons and CRISPRi-i3N neurons with or without transduction of a non-targeting sgRNA. Mean and standard deviations for replicates are shown.

(F) Heatmaps showing neuronal activity by GCaMP6m calcium imaging in i3N neurons and CRISPRi-i3N neurons with or without a non-targeting sgRNA.

(G) Knockdown of progranulin (GRN) in CRISPRi-NCRM5 neurons on Day 5 detected at the protein level by immunostanining. Top row, non-targeting control sgRNA. Bottom row, sgRNA targeting progranulin. For cells infected with progranulin-targeting sgRNA (indicated by arrow), progranulin signal (IF, green) is substantially reduced compared with cells infected with non-targeting sgRNA or cells not infected with sgRNA (indicated by arrowheads). The neuronal marker Tuj1 (IF, red), an sgRNA marker (BFP-NLS, purple) and a nuclear marker (mApple- NLS, blue) are shown.

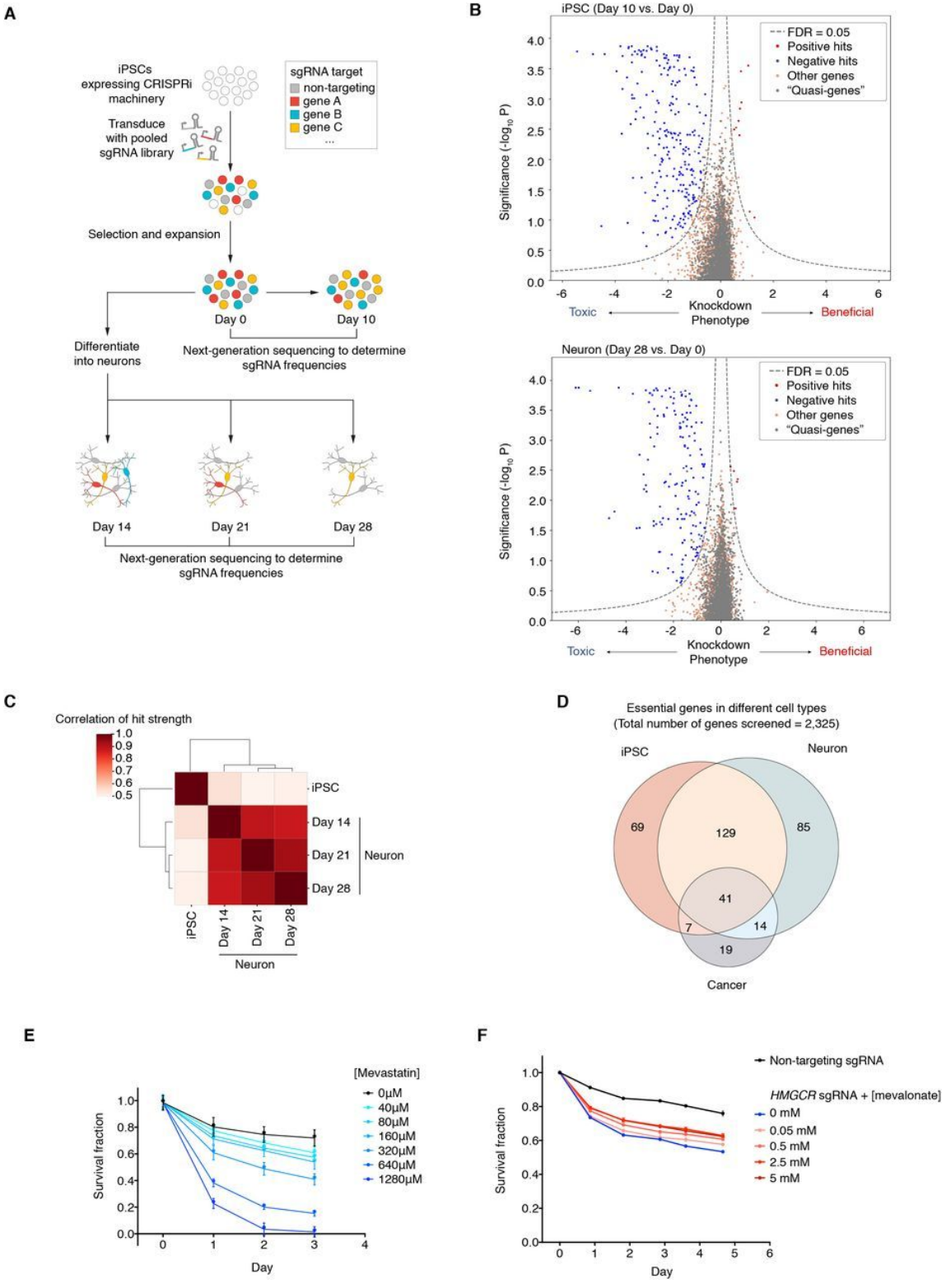
A
iPSCs expressing CRISPRi machinery
Transduce with pooled sgRNA library
sgRNA target
non-targeting
gene A
gene B
gene C
...
Selection and expansion
Day 0
Day 10
Next-generation sequencing to determine sgRNA frequencies
Differentiate into neurons
Day 14
Day 21
Day 28
Next-generation sequencing to determine sgRNA frequencies
B
iPSC (Day 10 vs. Day 0)
FDR = 0.05
Positive hits
Negative hits
Other genes
"Quasi-genes"
Significance (-log10 P)
Toxic
Knockdown Phenotype
Beneficial
Neuron (Day 28 vs. Day 0)
C
Correlation of hit strength
iPSC
Day 14
Day 21
Day 28
Neuron
D
Essential genes in different cell types
(Total number of genes screened = 2,325)
iPSC
Neuron
Cancer
69
129
85
41
7
14
19
E
[Mevastatin]
0μM
40μM
80μM
160μM
320μM
640μM
1280μM
Survival fraction
Day
F
Non-targeting sgRNA
HMGCR sgRNA + [mevalonate]
0 mM
0.05 mM
0.5 mM
2.5 mM
5 mM
Survival fraction
Day

Fig. 2.3. Massively parallel screen for essential genes in iPSCs and iPSC-derived neurons

(A) Strategy: CRISPRi-i3N iPSCs were transduced with a lentiviral sgRNA library targeting 2,325 genes (kinase and the druggable genome) and passaged as iPSCs or differentiated into glutamatergic neurons. Samples of cell populations were taken at different time points, and frequencies of cells expressing a given sgRNA were determined by next-generation sequencing.

(B) Volcano plots summarizing knockdown phenotypes and statistical significance (Mann-Whitney U test) for genes targeted in the pooled screen. Top, proliferation/survival of iPSCs between Day 0 and Day 10. Bottom, survival of iPSC-derived neurons between Day 0 and Day 28. Dashed lines: cutoff for hit genes (FDR = 0.05, see Methods).

(C) Correlation of hit gene strength (the product of phenotype and $-\log_{10}$(P value)) obtained for Day 10 iPSCs, and neurons harvested on Day 14, 21, or 28 post-induction.

(D) Overlap between essential genes we identified here in iPSCs and neurons, and gold-standard essential genes in cancer cell lines (Hart et al., 2017).

(E) Survival of neurons without treatment (black) or with various concentrations of Mevastatin (blue) quantified by microscopy; mean ± SD (six replicates).

(F) Survival of neurons infected with non-targeting sgRNA (black) or HMGCR sgRNA (blue) or HMGCR sgRNA with various concentrations of mevalonate (pink to red) quantified by microscopy; mean ± SD (six replicates).

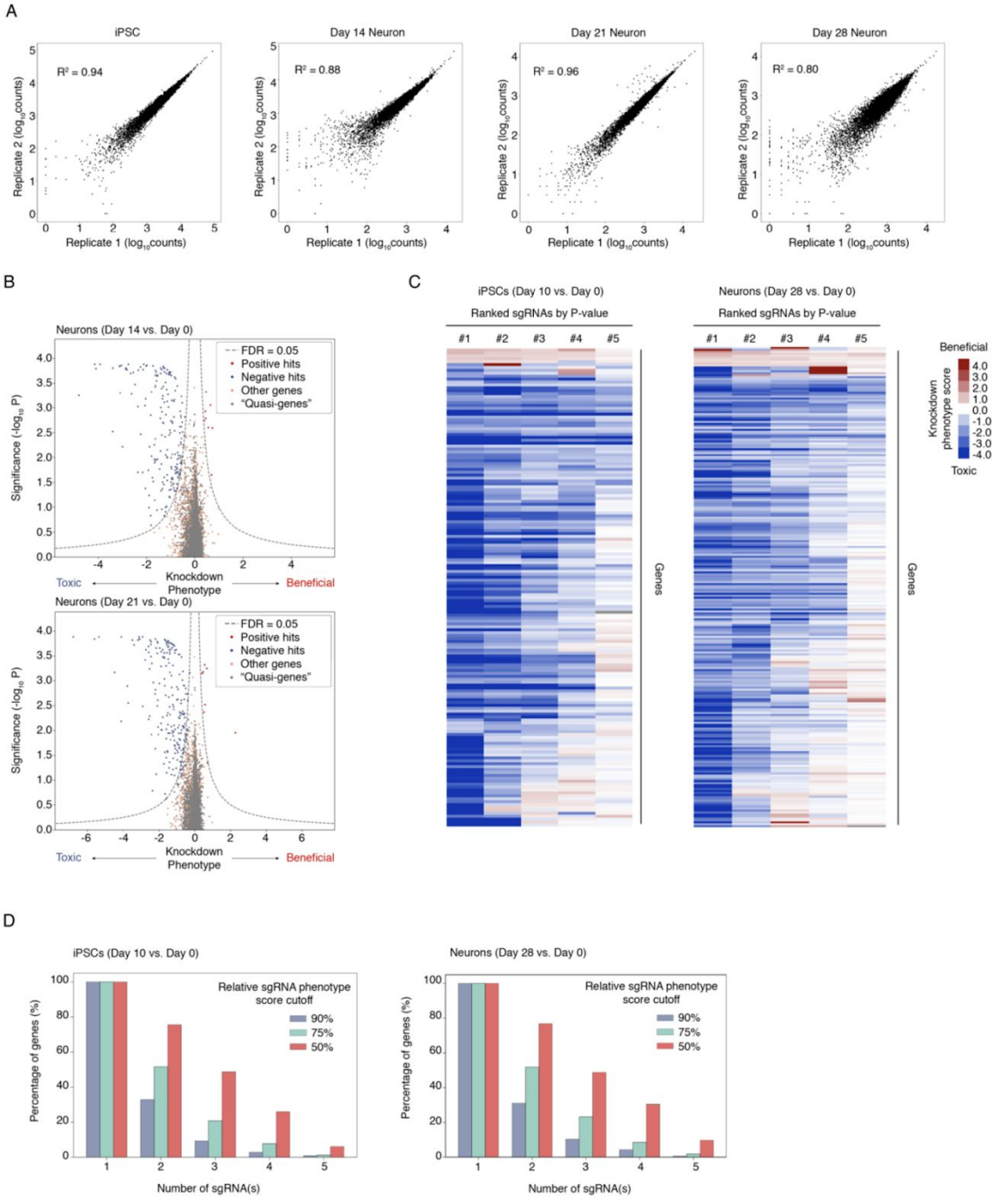

Fig.2.4. Characterization of results from massively parallel screens for essential genes in iPSCs and neurons

(A) Correlation of read counts from next-generation sequencing for individual sgRNAs between experimental replicates.

(B) Volcano plots summarizing knockdown phenotypes and statistical significance (Mann- Whitney U test) for genes targeted in the pooled screen in iPSC-derived neurons. Top, phenotypes for survival between Day 0 and Day 14. Bottom, phenotypes for survival between Day 0 and Day 21. Dashed lines represent the cutoff for hit genes, which was defined based on the product of phenotype and $-\log_{10}$(P value) at an empirically determined false discovery rate of 0.05 (see Methods).

(C) Heatmaps showing knockdown phenotype scores of all 5 sgRNAs (x-axis) for every hit gene (y-axis) in iPSCs (left) and iPSC-derived neurons (right). The five sgRNAs for a given gene are ranked by their p-values and are shown from left to right.

(D) Bar graphs summarizing the percentage of hit genes that have a certain number of sgRNAs (x-axis) showing a knockdown phenotype score above a given activity cutoff in iPSCs (left) and iPSC-drived neurons (right). For each sgRNA targeting a given gene, a relative sgRNA phenotype score was calculated by dividing its knockdown phenotype score by that of the most significant sgRNA targeting the same gene. Cutoffs are set based on the relative sgRNA phenotype scores.

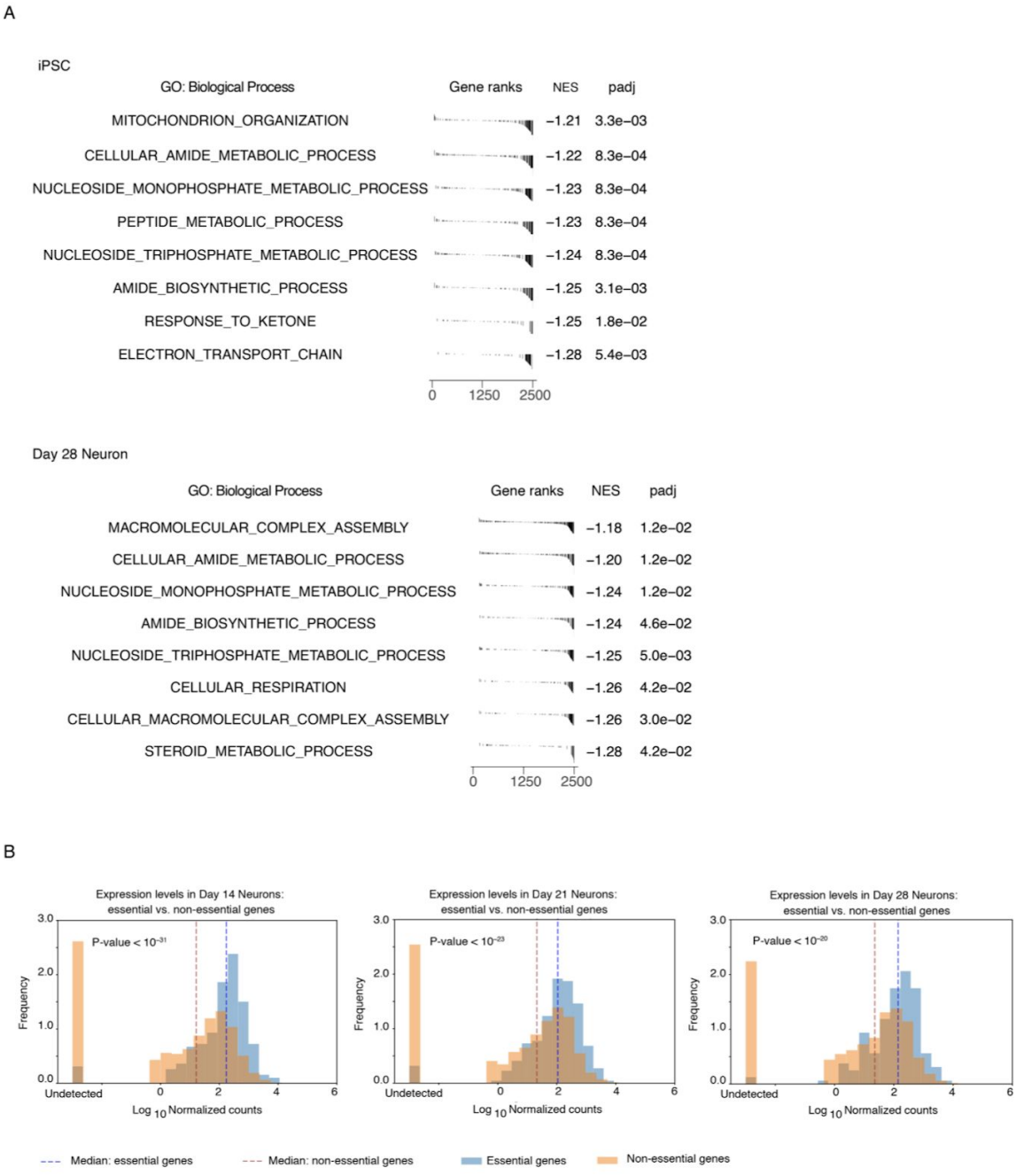

Fig.2.5. Functional analysis of hit genes from primary survival screens in iPSCs and iPSC-derived neurons

(A) Gene set enrichment analysis (GSEA) for hit genes from the screens. Significantly enriched GO terms for biological processes (BH-adjusted P value<0.05: 100,000 permutations) are shown for essential genes in iPSCs (Day 0 vs. Day 10) and neurons (Day 0 vs. Day 28). NES, normalized enrichment score.

(B) Expression levels of essential and non-essential genes in neurons at Day 14, 21, and 28 of differentiation were plotted as the distributions of $\log_{10}$ normalized counts from Quant- Seq. Median levels of expression were indicated. P values were calculated using one-sided Mann-Whitney U test.

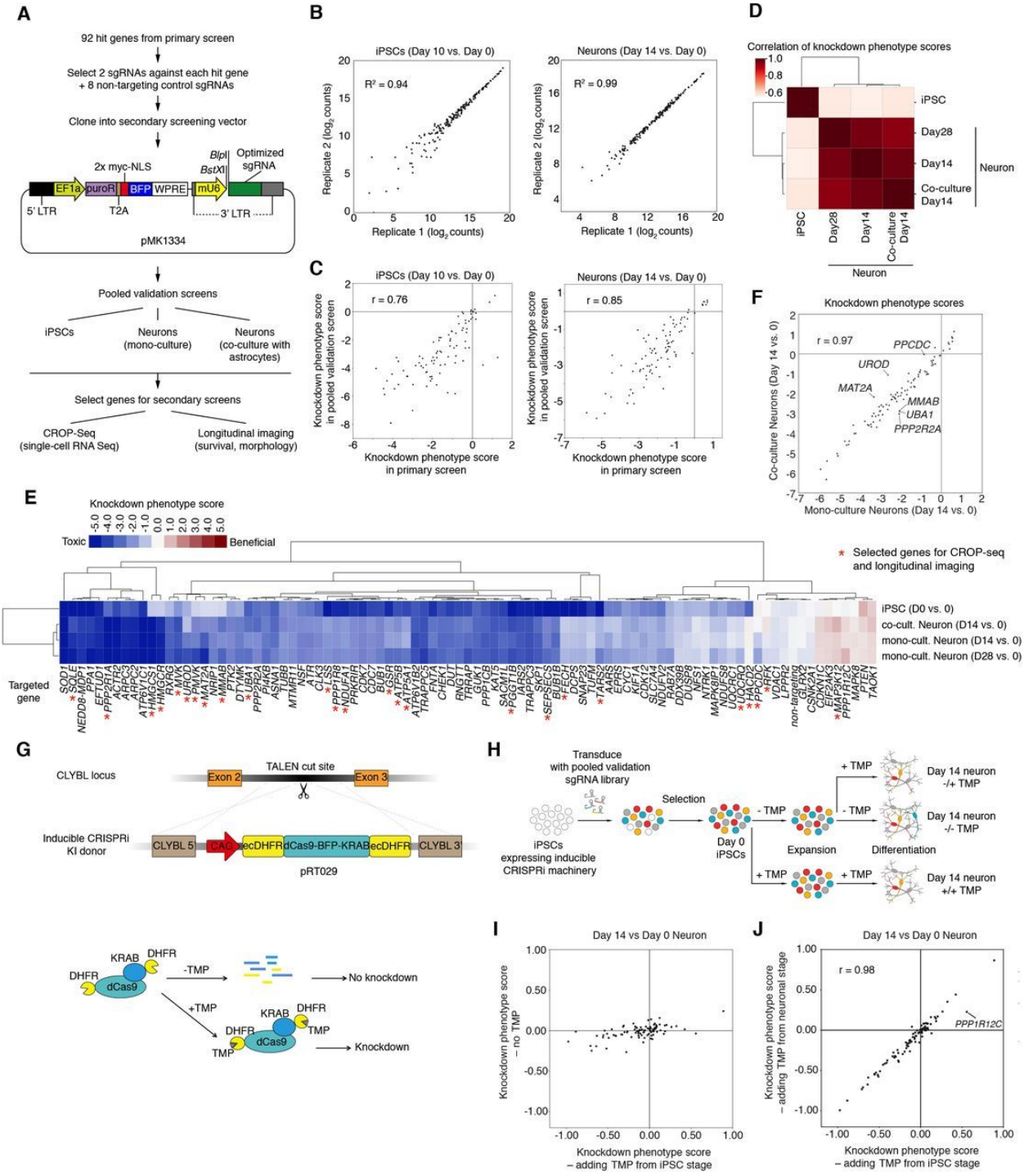

Fig.2.6. Pooled validation of hit genes from the primary screen
(A) Strategy for validation of hit genes.

(B) Raw counts of sgRNAs from next-generation sequencing for biological replicates of Day 10 iPSCs (left) and Day 14 neurons (right) and coefficients of determination (R2), Each dot represents one sgRNA.

(C) Knockdown phenotype scores from primary screens and validation screens for Day 10 iPSCs (left) and Day 14 neurons (right) and Pearson correlation coefficients (r). Each dot represents one gene.

(D) Hierarchical clustering of different cell populations from the pooled validation screens based on the pairwise correlations of the knockdown phenotype scores of all genes.

(E) Heatmap showing knockdown phenotype scores of the genes targeted in the validation screen (columns) in different cell populations (rows). Both genes and cell populations were hierarchically clustered based on Pearson correlation. Red asterisks mark genes selected for secondary screens (CROP-Seq and longitudinal imaging).

(F) Gene knockdown phenotype scores of Day 14 neurons in monoculture (x-axis) and co-culture with primary mouse astrocytes (y-axis) and Pearson correlation coefficient (r). Each dot represents one gene. Outlier genes, (differences > ± 2 SD from the mean differences) are labeled.

(G) Strategy for degron-based inducible CRISPRi. Addition of trimethoprim (TMP) stabilizes the DHFR degron-tagged CRISPRi machinery.

(H) Strategy to test whether hit genes control neuronal survival or earlier processes.

(I) Knockdown phenotype scores for Day 14 neurons from screens in the inducible CRISPRi iPSCs, comparing populations with TMP added from the iPSC stage (x-axis) to populations without TMP added (y-axis). Each dot represents one gene.

(J) Knockdown phenotype scores for Day 14 neurons from screens in the inducible CRISPRi iPSCs, comparing populations with TMP added from the iPSC stage (x-axis) to populations with TMP added from the neuronal stage (y-axis) and Pearson correlation coefficient (r). Each dot represents one gene. The outlier gene, PPP1R12C, is labeled.

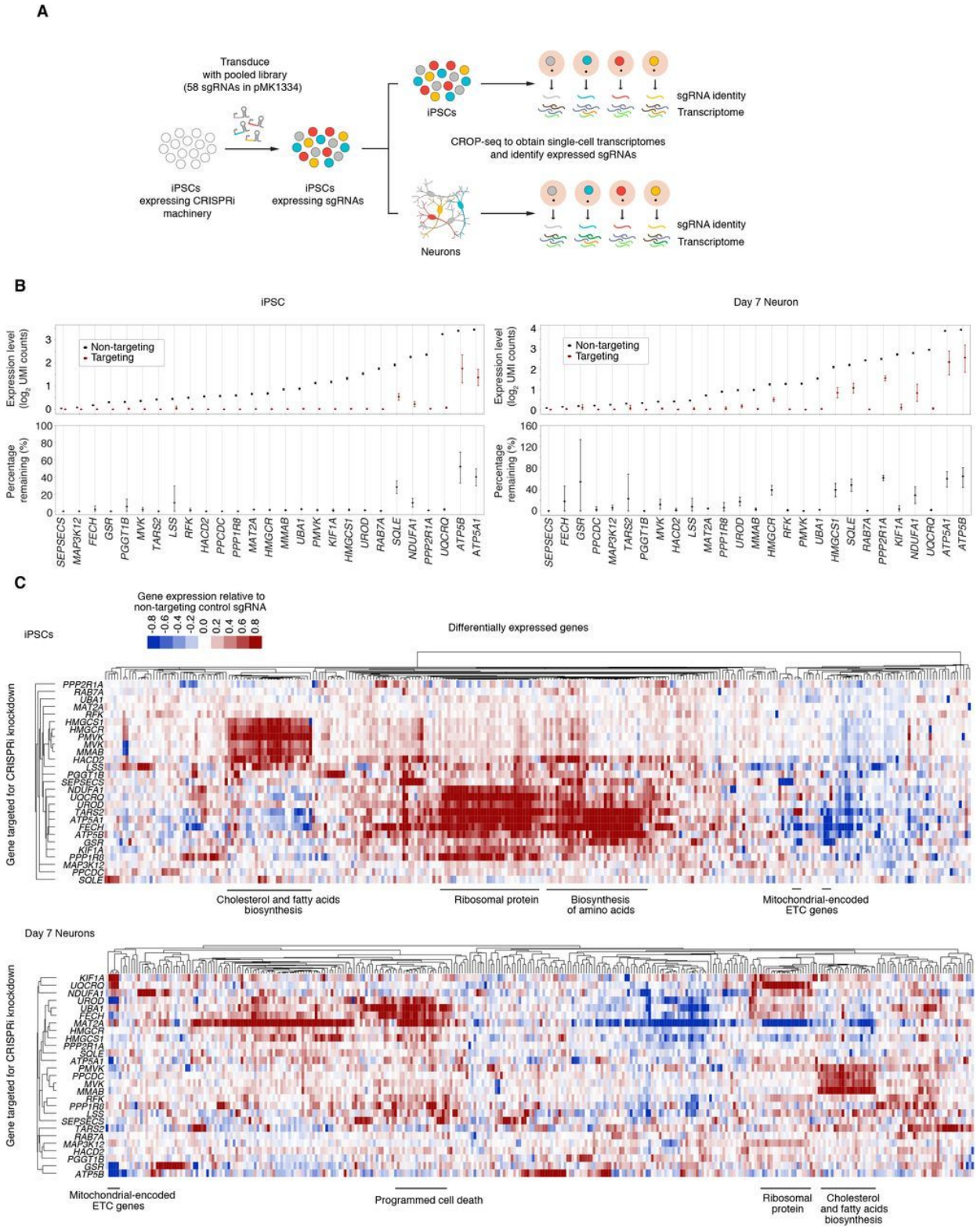

Fig.2.7. CROP-Seq reveals transcriptome changes in iPSCs and iPSC-derived neurons induced by knockdown of survival-relevant genes
(A) Strategy for CROP-Seq experiments.

(B) On-target knockdown efficiencies in the CROP-Seq screen were quantified for iPSCs (left) and Day 7 neurons (right). For each target gene, the 50% of cells with the strongest on-target knockdown were selected from all cells expressing sgRNAs targeting the gene; average expression of each target gene within these cells is compared to cells with non-targeting control sgRNAs. Error bars: 95% confidence intervals estimated by bootstrapping.

(C) Changes in gene expression in response to CRISPRi knockdown of genes of interest in iPSCs (top) and Day 7 neurons (bottom). Each row represents one targeted gene; for each targeted gene, the top 20 genes with the most significantly altered expression were selected, and the merged set of these genes is represented by the columns. Rows and columns were clustered hierarchically based on Pearson correlation. Functionally related groups of differentially expressed genes are labeled.

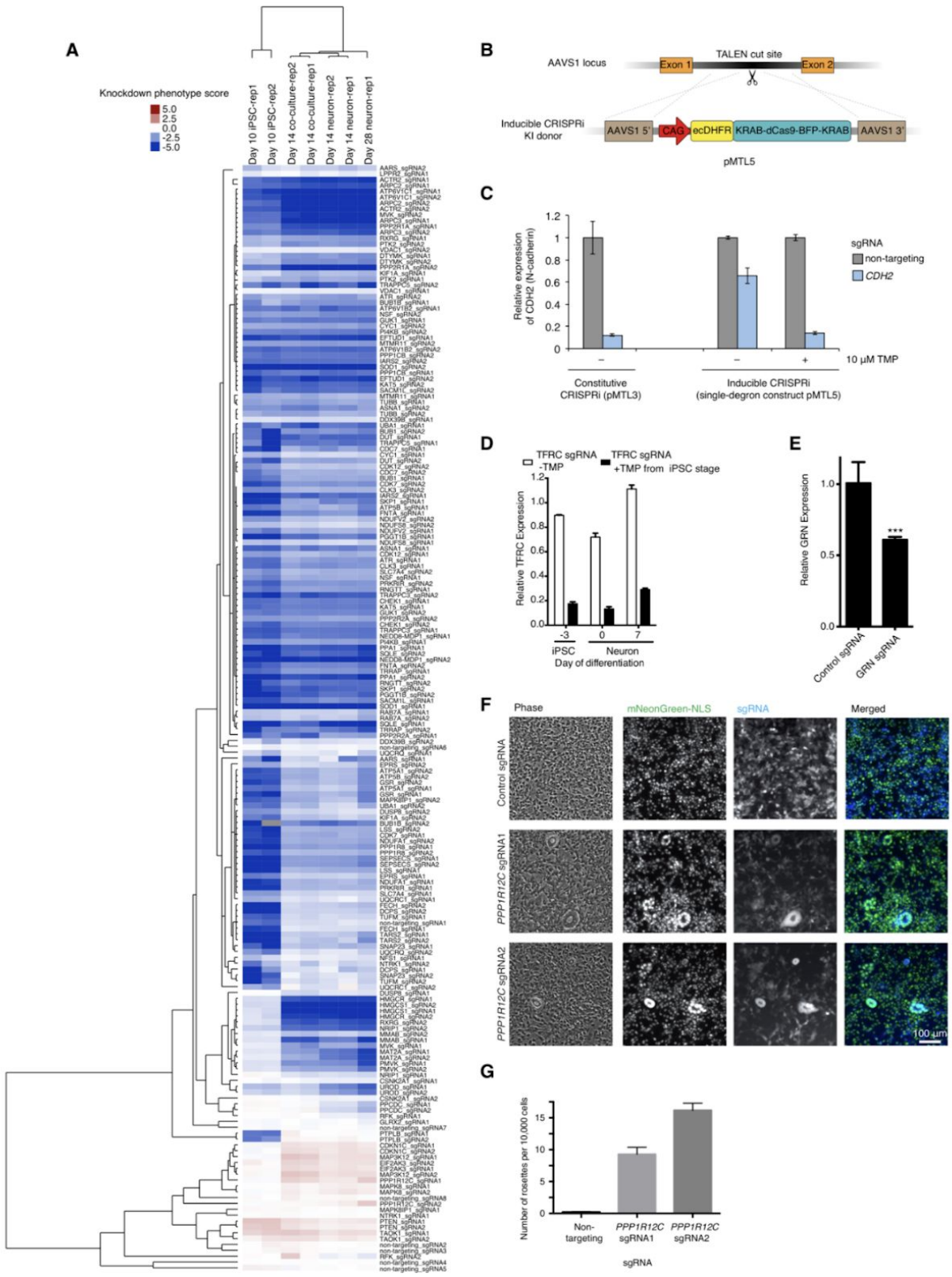
A
Knockdown phenotype score
5.0
2.5
0.0
-2.5
-5.0
Day 10 iPSC-rep1
Day 10 iPSC-rep2
Day 14 co-culture-rep2
Day 14 co-culture-rep1
Day 14 neuron-rep2
Day 14 neuron-rep1
Day 28 neuron-rep1
B
AAVS1 locus
Exon 1
TALEN cut site
Exon 2
Inducible CRISPRi KI donor
AAVS1 5'
CAG
ecDHFR
KRAB-dCas9-BFP-KRAB
AAVS1 3'
pMTL5
C
Relative expression of CDH2 (N-cadherin)
sgRNA
non-targeting
CDH2
10 μM TMP
Constitutive CRISPRi (pMTL3)
Inducible CRISPRi (single-degron construct pMTL5)
D
TFRC sgRNA -TMP
TFRC sgRNA +TMP from iPSC stage
Relative TFRC Expression
iPSC
Neuron
Day of differentiation
E
Relative GRN Expression
Control sgRNA
GRN sgRNA
F
Phase
mNeonGreen-NLS
sgRNA
Merged
Control sgRNA
PPP1R12C sgRNA1
PPP1R12C sgRNA2
100 μm
G
Number of rosettes per 10,000 cells
Non-targeting
PPP1R12C sgRNA1
PPP1R12C sgRNA2
sgRNA

Fig.2.8. Pooled validation of hit genes from the primary screen
(A) Heatmap showing relative knockdown phenotype scores of sgRNAs (rows) from the validation screens (columns, both experimental replicates, expect for Day 28 neurons, for which the second replicate sample was accidentally lost during sample preparation). Both sgRNAs and screens were hierarchically clustered based on Pearson correlation.

(B) Construct pMTL5 for the expression of CRISPRi machinery (dCas9-BFP-KRAB) fused to an N-terminal DHFR degron from the AAVS1 safe-harbor locus.

(C) Characterization of inducible CRISPRi activity in iPSCs with integrated single-degron CRISPRi machinery (construct pMTL5), compared to an equivalent constitutive construct lacking the degron (pMTL3). iPSCs were transduced with a lentiviral sgRNA expression construct containing a non-targeting sgRNA (grey bars) or an sgRNA targeting CDH2 (encoding N-cadherin, blue bars). Cells were cultured in the presence or absence of 10 μM trimethoprim (TMP), and cell-surface levels of N-cadherin were quantified by immunofluorescence flow cytometry 48 hours after transduction. Expression levels relative to non-targeting sgRNA are shown. Mean of two experimental replicates, error bars indicate standard deviation.

(D,E) Characterization of inducible CRISPRi activity in iPSCs and neurons with integrated double-degron CRISPRi machinery (construct pRT029). (D) Knockdown of the transferrin receptor (TFRC) in iPSCs and iPSC-derived neurons in the presence or absence of trimethoprim (TMP). iPSCs expressing the inducible CRISPRi machinery were lentivirally infected with an sgRNA targeting TFRC or a non-targeting negative control sgRNA. Infected iPSCs were cultured and differentiated into neurons in the presence of 20 μM TMP from iPSC stage or in the absence of TMP. Cells from both conditions were harvested at different days and levels of TFRC as well as ACTB mRNAs were quantified by qPCR. After normalizing each sample by ACTB mRNA levels, ratios of TFRC mRNA were calculated for cells expressing the TFRC-targeting sgRNA versus cells with the non-targeting sgRNA cultured in the same condition. Mean and standard deviations for replicates are shown. (E) qPCR result showing the conditional knockdown of GRN in iPSC-derived neurons. iPSCs expressing the dual-degron inducible CRISPRi machinery were lentivirally infected with an sgRNA targeting GRN or a non-targeting negative control sgRNA. Infected iPSCs were differentiated into neurons. The neurons were cultured in neuronal medium with the presence or absence of 20 μM TMP. Day 7 neurons from both conditions were harvested and levels of GRN as well as ACTB mRNAs were quantified by qPCR. After normalizing each sample by ACTB mRNA levels, ratios of GRN mRNA were calculated for cells expressing the GRN-targeting sgRNA versus cells with the control sgRNA cultured in the same condition. Mean and standard deviations for replicates are shown. One-tailed t-test was applied (*** $P<0.001$).

(F,G) Inhibition of the neuronal differentiation of CRISPRi-i3N iPSCs by sgRNAs targeting PPP1R12C. (F) Phase contrast (first column) and fluorescence (second and third column) micrographs of partially differentiated neuron populations infected with an

expression construct for sgRNAs (non-targeting control sgRNA, top row, or two different sgRNAs targeting PPP1R12C, middle and bottom row) and a BFP marker. Nuclei are visualized by expression of mNeonGreen-NLS (second column, green in merged images). Cells expressing sgRNAs are marked by cytosolic BFP (third column, blue in merged images). Images were acquired following six days of iPSC proliferation post-infection and three days of doxycycline-induced differentiation. (G) Quantification of undifferentiated colonies in a repeat experiment. Rosettes were counted manually by an individual blinded to the experimental conditions. The total number of cells was counted by Nikon Elements software bright spot detection module for green nuclei. Mean and SEM for replicate wells are shown (n = 6). One-way ANOVA and multiple comparisons were applied (****P<0.0001).

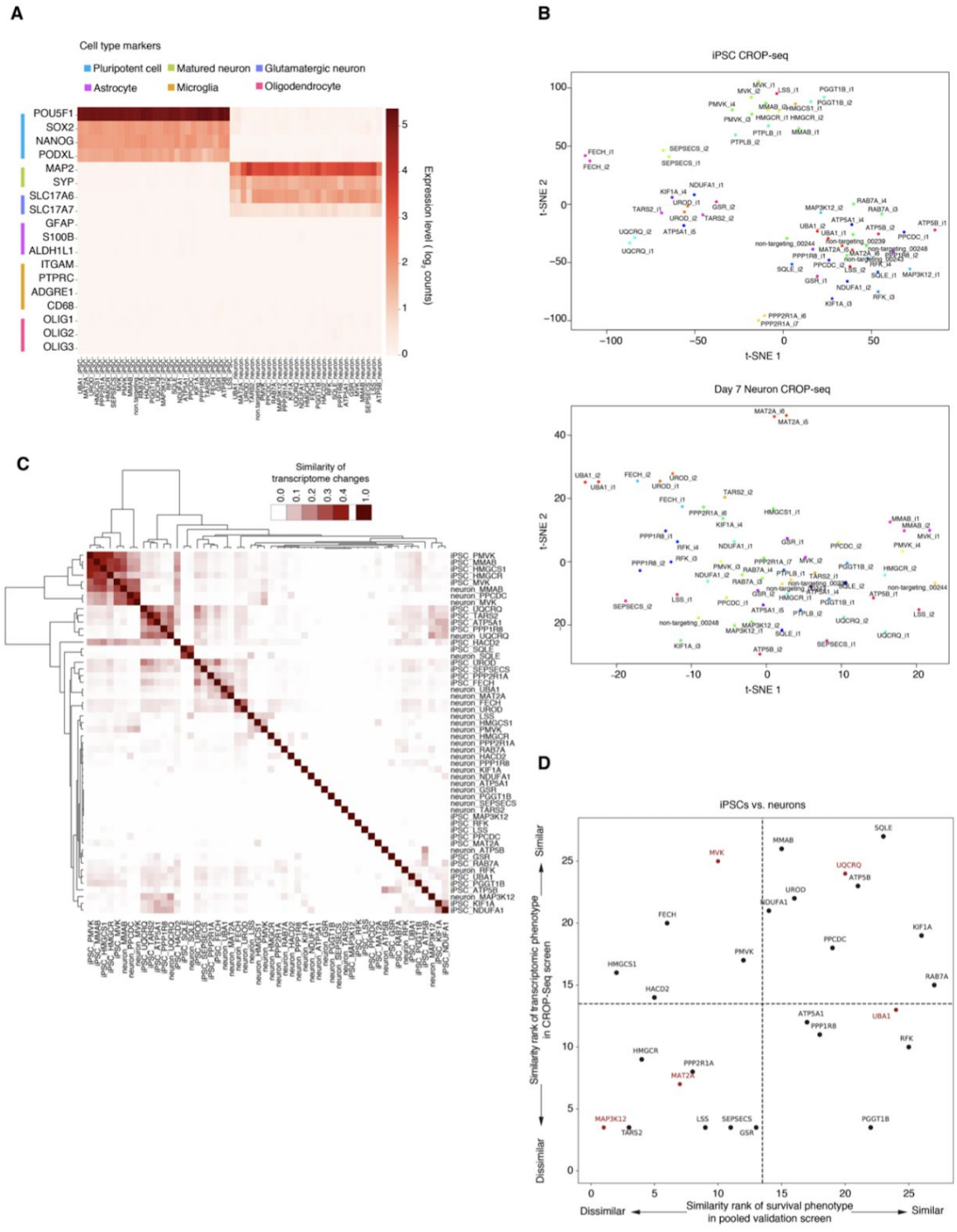

Fig.2.9. Characterization of CROP-Seq screen results
(A) Heatmap showing the expression levels of marker genes for different cell types in different gene knockdown groups in iPSCs and Day 7 neurons obtained from the

CROP-seq screen. The shade of red indicates the mean expression level of a given gene for all cells in that gene knockdown group.

(B) Transcriptomes of different sgRNA groups in iPSCs (left) and neurons (right) were visualized with t-Distributed stochastic neighbor embedding (t-SNE), colored by target genes.

(C) Pairwise similarities of transcriptome changes of different gene knockdown groups across iPSCs and neurons were determined based on the numbers of overlapping and total transcripts that were significantly altered in two groups (see Methods for details). Gene knockdown groups were hierarchically clustered based on Pearson correlation. The shade of red indicates the similarity.

(D) Comparison of differences between iPSCs and neurons in knockdown phenotypes for survival and transcriptomic responses. Genes were ranked by similarities between iPSCs and neurons in their knockdown phenotypes in terms of survival (x-axis) or transcriptomic response (y-axis). Dashed lines indicate the middle rank positions. Genes selected for further discussion are labeled in red.

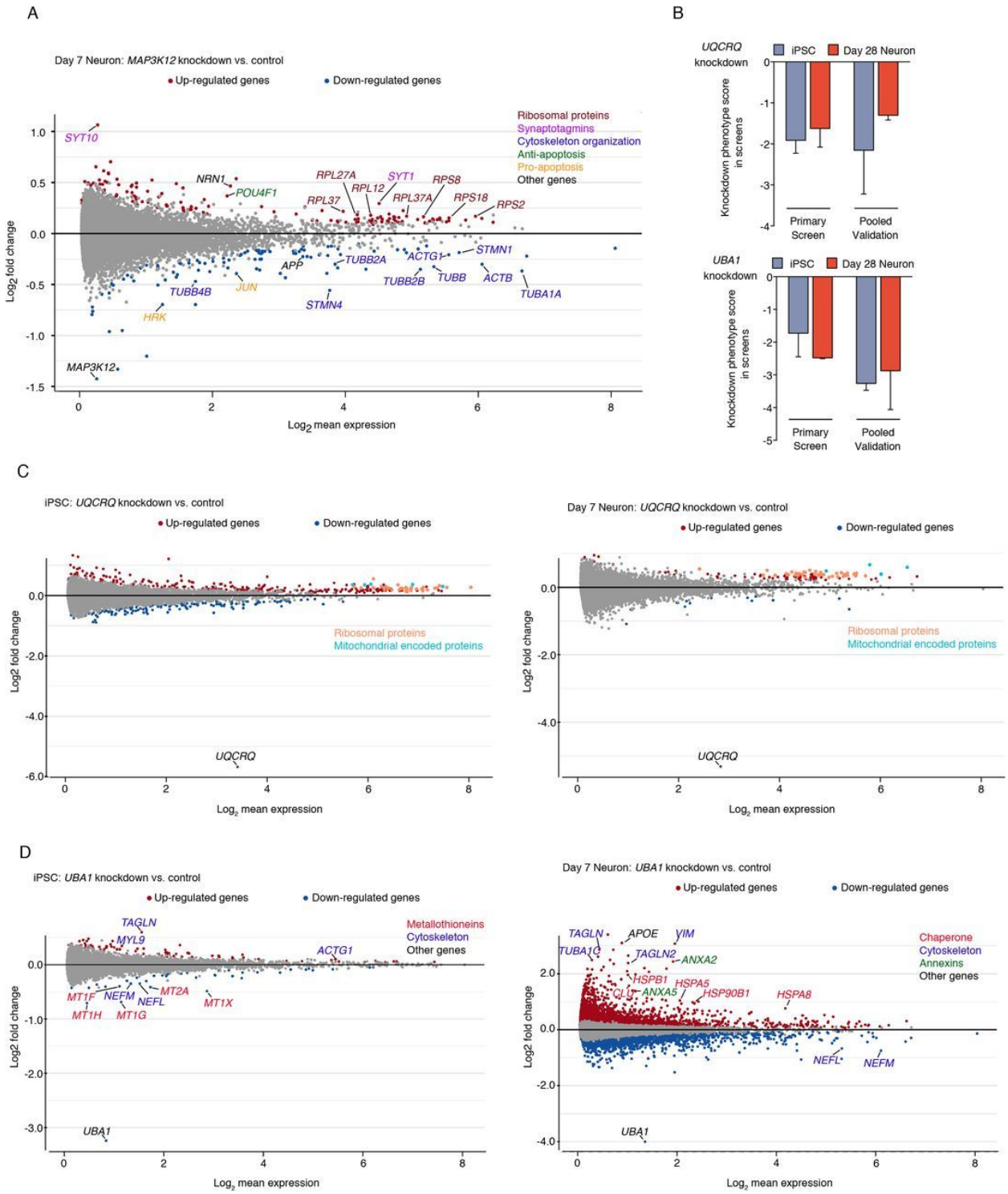

Fig.2.10. Cell-type specific responses to gene knockdown on the transcriptomic level

(A) Changes in transcript levels caused by MAP3K12 knockdown in neurons from the CROP-Seq screen. Differentially expressed genes (padj < 0.05) in red (upregulation) or blue (downregulation), or other colors for genes discussed in the main text.

(B) Knockdown phenotypes of UQCRQ (top) and UBA1 (bottom) in iPSCs and iPSC-derived neurons from the primary and validation screens. Survival phenotypes of 2 sgRNAs targeting the same gene, mean ± SD.

(C,D) Transcriptomic changes caused by knockdown of UQCRQ (C) or UBA1 (D) in iPSCs and neurons. Differentially expressed genes (padj < 0.05) in red (upregulation) or blue (downregulation), or other colors for genes discussed in the main text.

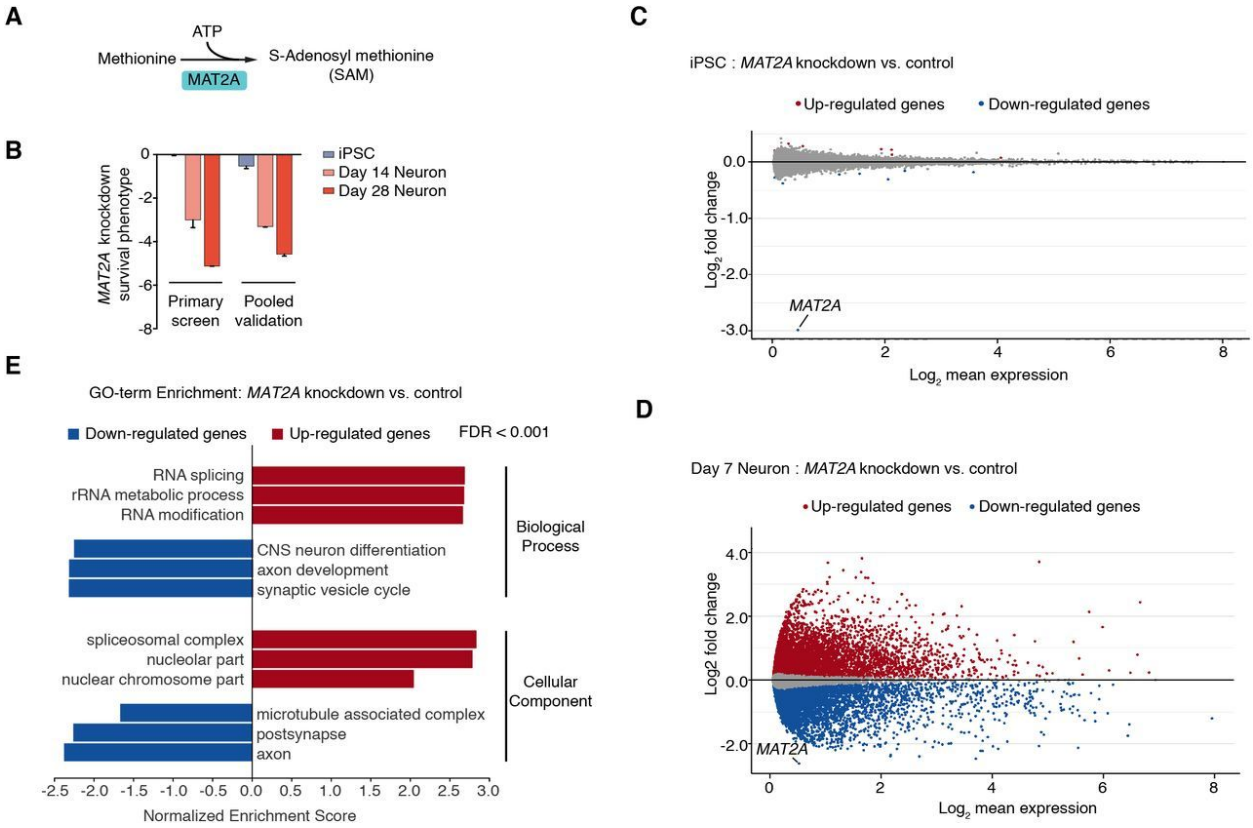

Fig.2.11. CROP-Seq reveals neuron-specific transcriptomic consequences of MAT2A knockdown

(A) Methionine adenosyl transferase 2a (MAT2A) catalyzes the production of the methyl donor S-adenosylmethionine (SAM) from methionine and ATP.

(B) MAT2A is essential in neurons but not iPSCs. Knockdown phenotypes of MAT2A in iPSCs and neurons from the primary and validation screens. Survival phenotypes of 2 sgRNAs targeting MAT2A, mean ± SD.

(C,D) Changes in transcript levels caused by MAT2A knockdown in iPSCs (C) and neurons (D) from the CROP-Seq screen. Differentially expressed genes (padj < 0.05) in red (upregulation) or blue (downregulation).

(E) Gene Set Enrichment Analysis (GSEA) results for differentially expressed genes in iPSC-derived neurons with MAT2A knockdown compared to negative control sgRNAs. Significantly enriched GO terms for Biological Process and Cellular Component are shown.

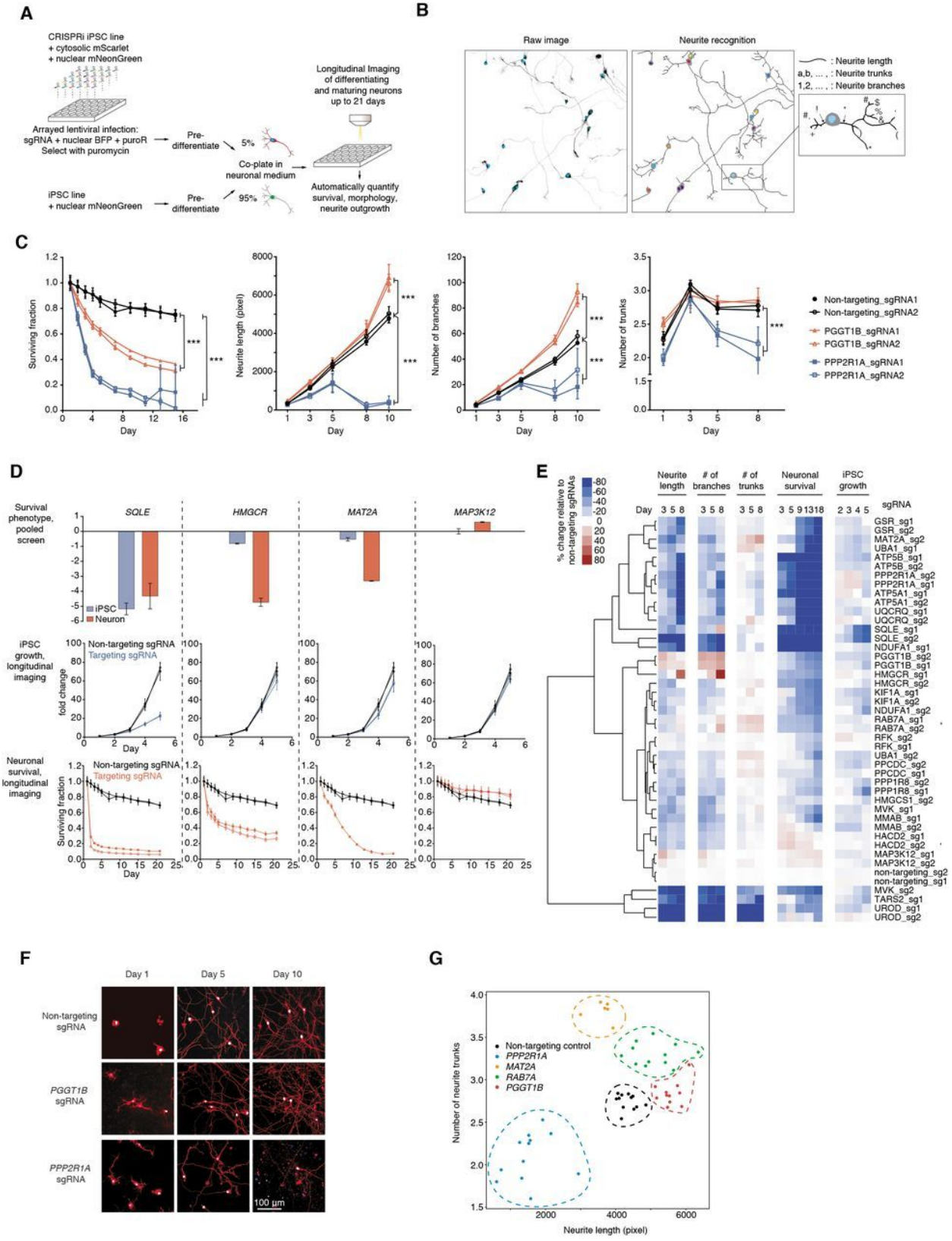
A
CRISPRi iPSC line
+ cytosolic mScarlet
+ nuclear mNeonGreen
Arrayed lentiviral infection:
sgRNA + nuclear BFP + puroR
Select with puromycin
Pre-differentiate
5%
95%
Co-plate in neuronal medium
Longitudinal Imaging of differentiating and maturing neurons up to 21 days
Automatically quantify survival, morphology, neurite outgrowth
iPSC line
+ nuclear mNeonGreen
B
Raw image
Neurite recognition
: Neurite length
a,b, ... , : Neurite trunks
1,2, ... , : Neurite branches
C
Surviving fraction
Neurite length (pixel)
Number of branches
Number of trunks
Day
Non-targeting_sgRNA1
Non-targeting_sgRNA2
PGGT1B_sgRNA1
PGGT1B_sgRNA2
PPP2R1A_sgRNA1
PPP2R1A_sgRNA2
D
Survival phenotype, pooled screen
SQLE
HMGCR
MAT2A
MAP3K12
iPSC
Neuron
iPSC growth, longitudinal imaging
Non-targeting sgRNA
Targeting sgRNA
fold change
Neuronal survival, longitudinal imaging
Surviving fraction
Day
E
% change relative to non-targeting sgRNAs
Neurite length
# of branches
# of trunks
Neuronal survival
iPSC growth
Day
sgRNA
GSR_sg1
GSR_sg2
MAT2A_sg2
UBA1_sg1
ATP5B_sg1
ATP5B_sg2
PPP2R1A_sg2
PPP2R1A_sg1
ATP5A1_sg1
ATP5A1_sg2
UQCRQ_sg1
UQCRQ_sg2
SQLE_sg1
SQLE_sg2
NDUFA1_sg1
PGGT1B_sg2
PGGT1B_sg1
HMGCR_sg1
HMGCR_sg2
KIF1A_sg1
KIF1A_sg2
NDUFA1_sg2
RAB7A_sg1
RAB7A_sg2
RFK_sg2
RFK_sg1
UBA1_sg2
PPCDC_sg2
PPCDC_sg1
PPP1R8_sg2
PPP1R8_sg1
HMGCS1_sg2
MVK_sg1
MMAB_sg1
MMAB_sg2
HACD2_sg1
HACD2_sg2
MAP3K12_sg1
MAP3K12_sg2
non-targeting_sg2
non-targeting_sg1
MVK_sg2
TARS2_sg1
UROD_sg1
UROD_sg2
F
Day 1
Day 5
Day 10
Non-targeting sgRNA
PGGT1B sgRNA
PPP2R1A sgRNA
100 µm
G
Number of neurite trunks
Neurite length (pixel)
Non-targeting control
PPP2R1A
MAT2A
RAB7A
PGGT1B

Fig.2.12 .Longitudinal imaging to track the effect of selected hit gene knockdown on iPSC growth, neuronal survival and neurite morphology
(A) Strategy for longitudinal imaging for neuronal survival and neurite morphology.

(B) An example illustrating the image analysis pipeline. A raw image (left) containing sgRNA positive neurons expressing nuclear BFP (cyan) and cytosolic mScarlet (greyscale) were segmented and neurites were recognized (right). Different parameters, including neurite length, number of neurite trunks and number of neurite branches were quantified for individual neurons. Total number of sgRNA positive neurons was quantified for each image to monitor neuronal survival.

(C) Quantification of knockdown effects of PGGT1B and PPP2R1A on neuronal survival, neurite length, number of branches and number of trunks. For each sgRNA, mean ± SD of replicate images is shown for each time point. *** significant differences compared to non-targeting sgRNA ($P < 0.001$, Student's t-test).

(D) Examples of hit genes whose survival phenotypes in the pooled screens were validated by longitudinal imaging. Top, knockdown phenotypes of SQLE, HMGCR, MAT2A and MAP3K12 in iPSCs and neurons from the validation screens. Average phenotypes of two sgRNAs targeting each gene; error bars represent SD. Growth curves of iPSCs (middle) and survival curves of neurons (bottom) with non-targeting sgRNAs and sgRNAs targeting SQLE, HMGCR, MAT2A or MAP3K12. Fold change (for iPSCs, middle) or surviving fraction (for neurons, bottom) of number of sgRNA-positive cells relative to Day 1 was calculated for each imaging well, mean ± SD for all replicate wells for one sgRNA are shown.

(E) Changes of iPSC proliferation, neuronal survival and neurite morphology features relative to non-targeting sgRNAs at different time points (columns) induced by knockdown of different genes (rows). Rows were hierarchically clustered based on Pearson correlation.

(F) Representative images of neurons with PGGT1B and PPP2R1A knockdown on Days 1, 5 and 10. Nuclear BFP is shown in blue, cytosolic mScarlet is shown in red. Scale bar, 100 μm.

(G) Effect of gene knockdown on neurite length (x-axis) and number of neurite trunks (y-axis). Each dot indicates the mean measurements of all neurons in one image. Different target genes are shown in different colors, and replicate images for one target gene are grouped by dashed lines in the same colors.

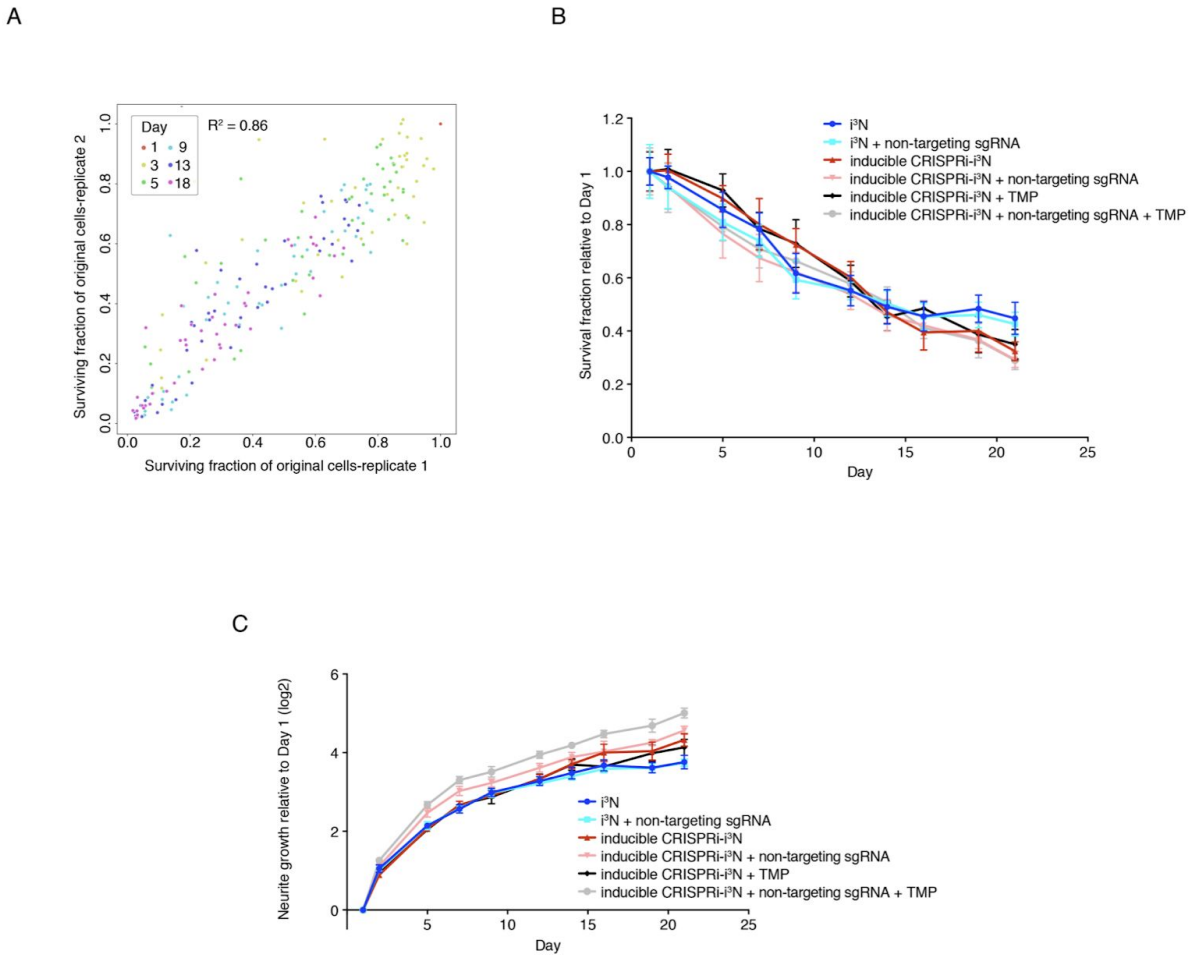

Fig.2.13. Reproducibility of longitudinal imaging results

(A) Scatter plot showing surviving fractions of neurons with different sgRNAs at different days of differentiation (shown in different colors) relative to Day 1 in two independent sets of imaging experiments. Each dot represents one sgRNA in a certain time point. Coefficient of determination (R2) is indicated.

(B,C) Survival (B) and neurite growth (C) of i3N neurons and inducible CRISPRi i3N neurons with or without non-targeting sgRNA in the absence or presence of TMP, quantified from longitudinal imaging data. Mean and standard deviations for 6 replicate wells are shown.

TABLES

Table 2.1 Key resources

REAGENT or RESOURCE	SOURCE	IDENTIFIER
Antibodies		
Goat polyclonal anti-human progranulin	R&D Systems	Cat#AF2420; RRID:AB_2114489
Mouse monoclonal anti-TUJ1	BioLegend	Cat#801201; RRID:AB_2313773
Donkey polyclonal anti-goat AF-488	Jackson ImmunoResearch	Cat#705-545-147; RRID:AB_2336933
Donkey polyclonal anti-mouse RRX	Jackson ImmunoResearch	Cat#715-295-151; RRID:AB_2340832
Donkey polyclonal anti-goat AF-647	Jackson ImmunoResearch	Cat#705-605-147; RRID:AB_2340437
Donkey polyclonal anti-mouse AF-488	Jackson ImmunoResearch	Cat#715-545-151; RRID:AB_2341099
Guinea pig polyclonal anti-NeuN	MilliporeSigma	Cat#ABN90; RRID:AB_11205592
Chicken polyclonal anti-MAP2	Abcam	Cat#ab5392; RRID:AB_2138153

REAGENT or RESOURCE	SOURCE	IDENTIFIER
Mouse monoclonal anti-human tau	Thermo	Cat#MN1000; RRID:AB_2314654
Goat polyclonal anti-guinea pig AF-647	ThermoFisher Scientific	Cat#A-21450; RRID:AB_2735091
Donkey polyclonal anti-chicken AF-647	Jackson ImmunoResearch	Cat#703-605-155; RRID:AB_2340379
Mouse monoclonal anti- β-Actin (8H10D10)	Cell Signaling Technology	Cat# 3700, RRID:AB_2242334
Mouse monoclonal anti-phospho-Histone H2A.X (Ser139)	Millipore	Cat# 05-636, RRID:AB_309864
Rabbit monoclonal anti-UBQLN2 (D7R2Z)	Cell Signaling Technology	Cat# 85509, RRID:AB_2800056
IRDye 680RD Goat anti-Mouse IgG	LI-COR Biosciences	Cat# 926-68070, RRID:AB_10956588
IRDye 800CW Goat anti-Rabbit IgG	LI-COR Biosciences	Cat# 926-32211, RRID:AB_621843

Chemicals, Peptides, and Recombinant Proteins		
REAGENT or RESOURCE	SOURCE	IDENTIFIER
Trimethoprim	Sigma	Cat#92131-5G
CNQX disodium salt	Tocris	Cat#1045
Puromycin dihydrochloride	Sigma	Cat#P9620-10ML
Blastidicin S HCl	Gemini Bio-Products	Cat#400-165P
Hoechst 33342	Thermo	Cat#62249
Lipofectamine Stem	ThermoFisher	Cat#STEM00003
Alt-R S.p. HiFi Cas9 Nuclease V3	IDT	Cat#1081060
Lipofectamine 3000 Transfection Reagent	ThermoFisher Scientific	Cat# L3000015
ViralBoost	Alstem	Cat#VB100
BrainPhys Neuronal Medium	STEMCELL Technologies	Cat#05790
BrainPhys without Phenol Red	STEMCELL Technologies	Cat#05791
Cultrex 3D Culture Matrix Laminin I	R&D Systems	Cat#3446-005-01

REAGENT or RESOURCE	SOURCE	IDENTIFIER
Doxycycline hyclate	Sigma	Cat#D9891
Poly-L-ornithine hydrobromide	Sigma-Aldrich	Cat#P3655-50MG
Etoposide	Abcam	Cat#ab120227
Essential 8 Medium	Thermo Fisher Scientific	Cat#A1517001
Matrigel Basement Membrane Matrix	Corning	Cat#356231
Y-27632 dihydrochloride ROCK inhibitor	Tocris	Cat#125410
N2 Supplement	Thermo Fisher Scientific	Cat#17502-048
B27 Supplement	Thermo Fisher Scientific	Cat#17504-044
NT-3	PeproTech	Cat#450-03
BDNF	PeproTech	Cat#450-02
Mevastatin	Sigma-Aldrich	Cat#M2537
Mevalonate	Sigma-Aldrich	Cat#M4667
Critical Commercial Assays		
Direct-zol 96 RNA Kit	Zymo	Cat#R2055

REAGENT or RESOURCE	SOURCE	IDENTIFIER
iTaq Universal Probes One-Step Kit	Bio-Rad	Cat#172-5141
Chromium Single Cell 3’ Library & Gel Bead Kit v2	10x Genomics	Cat# 120267
Chromium i7 Multiplex Kit Kit	10x Genomics	Cat#120262
Chromium Single Cell A Chip	10x Genomics	Cat#1000009
Chromium Controller & Accessory Kit	10x Genomics	Cat#120223
Quick-RNA Miniprep Kit	Zymo	Cat#R1054
Qubit RNA HS Assay Kit	Invitrogen	Cat#Q32855
QuantSeq 3’ mRNA-Seq Library Prep Kit FWD	Lexogen	Cat#015
Qubit dsDNA HS Assay Kit	Invitrogen	Cat#Q32851
High Sensitivity DNA Kit	Agilent	Cat#5067-4626

REAGENT or RESOURCE	SOURCE	IDENTIFIER
SensiFAST SYBR Lo-ROX 2X master mix	Bioline	Cat#BIO-94005
GAPDH PrimePCR Primers	Bio-Rad	Unique Assay ID: qHsaCEP0041396
GRN PrimePCR Primers	Bio-Rad	Unique Assay ID: qHsaCEP0057821
UBQLN2 PrimePCR Primers	Bio-Rad	Unique Assay ID: qHsaCEP0055207
Deposited Data		
iNeuron-RNA-Seq	This paper	https://kampmannlab.ucsf.edu/ineuron-rna-seq ; GEO: GSE124703
iPSC and Day 7 Neuron CROP-seq Data	This paper	GEO: GSE124703

Experimental Models: Cell Lines		
REAGENT or RESOURCE	SOURCE	IDENTIFIER
Human: NCRM5 iPSC line	Luo et al., 2014	N/A
Human: i3N iPSC line	Wang et al., 2017	N/A
Recombinant DNA		
Plasmid: Ef1a-mNeon-Green-NLS (H53)	This paper	N/A
Plasmid: Ef1a-mScarlet (I2)	This paper	N/A
Plasmid: Ef1a-GCaMP6m (I1)	This paper	N/A
Plasmid: CLYBL-TO-hNGN2-BSD-mApple	Addgene	Addgene Plasmid#124229; RRID:Addgene_124229
Plasmid: pCE-mp53DD	Okita et al., 2013	Addgene Plasmid#41856; RRID:Addgene_41856
Plasmid: pC13N-CLYBL-CAG-dCas9-BFP-KRAB	This paper	N/A
Plasmid: pRT029	This paper	N/A
Plasmid:pMTL3	This paper	N/A
Plasmid:pMTL5	This paper	N/A
Plasmid:pMK1334	This paper	N/A

Software and Algorithms		
REAGENT or RESOURCE	SOURCE	IDENTIFIER
NIS Elements AR 5.02.01 64-bit	Nikon Instruments Inc.	https://www.microscope.healthcare.nikon.com/products/software/nis-elements
Fiji - 2.0.0-rc-69/1.52n	Schindelin et al., 2012	https://imagej.net/Fiji
CellProfiler- 3.1.5	Carpenter et al., 2006	https://cellprofiler.org/
BlueBee Genomics Platform	BlueBee	https://www. bluebee.com/quantseq
Bowtie- 1.2.1.1	Langmead et al., 2009	http://bowtie-bio.sourceforge.net/index.shtml
MAGeCK- 0.5.7	Lie et al., 2014	https://sourceforge.net/p/mageck/wiki/Home/
MAGeCK-iNC	This paper	kampmannlab.ucsf.edu/mageck-inc

REAGENT or RESOURCE	SOURCE	IDENTIFIER
Cell Ranger- 2.2.0	10X Genomics	https://support.10xgenomics.com/single-cell-gene-expression/software/pipelines/latest/what-is-cell-ranger
R- 3.5.1	The R project	https://www.r-project.org/
scater- 1.8.4	McCarthy et al., 2017	https://bioconductor.org/packages/release/bioc/html/scater.html
fgsea – 1.7.1	Sergushichev, 2016	https://bioconductor.org/packages/release/bioc/html/fgsea.html
WebGestalt	Zhang et al., 2005	http://www.webgestalt.org/#
Cluster- 3.0	Eisen et al., 1998	http://bonsai.hgc.jp/~mdehoon/software/cluster/software.htm#ctv
Java TreeView- 1.1.6r4	Saldanha, 2004	http://jtreeview.sourceforge.net/

MATERIALS AND METHODS

Human iPSCs

Human iPSCs (male WTC11 background (Miyaoka et al., 2014) unless otherwise noted; male NCRM5 (Luo et al., 2014) background in Fig. 2.2G) were cultured in Essential 8 Medium (Gibco/Thermo Fisher Scientific; Cat. No. A1517001) on BioLite Cell Culture Treated Dishes (Thermo Fisher Scientific; assorted Cat. No.) coated with Growth Factor Reduced, Phenol Red-Free, LDEV-Free Matrigel Basement Membrane Matrix (Corning; Cat. No. 356231) diluted 1:100 in Knockout DMEM (Gibco/Thermo Fisher Scientific; Cat. No. 10829-018). Briefly, Essential 8 Medium was replaced every other day or every day once 50% confluent. When 80-90% confluent, cells were passaged, which entailed the following: aspirating media, washing with DPBS, incubating with StemPro Accutase Cell Dissociation Reagent (Gibco/Thermo Fisher Scientific; Cat. No. A11105-01) at 37°C for 7 minutes, diluting Accutase 1:5 in DPBS, collecting in conicals, centrifuging at 200g for 5 minutes, aspirating supernatant, resuspending in Essential 8 Medium supplemented with 10nM Y-27632 dihydrochloride ROCK inhibitor (Tocris; Cat. No. 125410), counting, and plating onto Matrigel-coated plates at desired number.

Human iPSC-derived neurons

Human iPSCs engineered to express mNGN2 under a doxycycline-inducible system in the AAVS1 safe harbor locus were used for the differentiation protocol below.

iPSCs were released and centrifuged as above, and pelleted cells were resuspended in N2 Pre-Differentiation Medium containing the following: Knockout DMEM/F12 (Gibco/Thermo Fisher Scientific; Cat. No. 12660-012) as the base, 1X MEM Non-Essential Amino Acids (Gibco/Thermo Fisher Scientific; Cat. No. 11140-050), 1X N2 Supplement (Gibco/Thermo Fisher Scientific; Cat. No. 17502-048), 10ng/mL NT-3 (PeproTech; Cat. No. 450-03), 10ng/mL BDNF (PeproTech; Cat. No. 450-02), 1µg/mL Mouse Laminin (Thermo Fisher Scientific; Cat. No. 23017-015), 10nM ROCK inhibitor, and 2µg/mL doxycycline hydrochloride (Sigma-Aldrich; Cat. No. D3447-500MG) to induce expression of mNGN2. iPSCs were counted and plated at 7 x 105 cells per Matrigel-coated well of a 6-well plate in 2mL of N2 Pre-Differentiation Medium, or at 4 x 106 cells per Matrigel-coated 10-cm dish in 12mL of medium, for three days. After three days, hereafter Day 0, pre-differentiated cells were released and centrifuged as above, and pelleted cells were resuspended in Classic Neuronal Medium containing the following: half DMEM/F12 (Gibco/Thermo Fisher Scientific; Cat. No. 11320-033) and half Neurobasal-A (Gibco/Thermo Fisher Scientific; Cat. No. 10888-022) as the base, 1X MEM Non-Essential Amino Acids, 0.5X GlutaMAX Supplement (Gibco/Thermo Fisher Scientific; Cat. No. 35050-061), 0.5X N2 Supplment, 0.5X B27 Supplement (Gibco/Thermo Fisher Scientific; Cat. No. 17504-044), 10ng/mL NT-3, 10ng/mL BDNF, 1µg/mL Mouse Laminin, and 2µg/mL doxycycline hydrochloride. Pre-differentiated cells were subsequently counted and plated plated at 2 x 105 cells per well of a BioCoat Poly-D-Lysine 12-well plate (Corning; Cat. No. 356470) in 1mL of Classic Neuronal Medium, or at 7.5 x 106 cells per BioCoat Poly-D-Lysine 10-cm dish (Corning; Cat. No.

356469) in 10mL medium. On Day 7, half of the medium was removed and an equal volume of fresh Classic Neuronal Medium without doxycycline was added. On Day 14, half of the medium was removed and twice that volume of fresh medium without doxycycline was added. On Day 21, one-third of the medium was removed and twice that volume of fresh medium without doxycycline was added. On Day 28 and each week after, one-third of the medium was removed and an equal volume of fresh medium without doxycycline was added.

For the longitudinal imaging screens, updated media formulations were used for neuronal differentiation and culture. During the three days of pre-differentiation, we used Induction Medium containing the following: Knockout DMEM/F12 (Gibco/Thermo Fisher Scientific; Cat. No. 12660-012) as the base, 1X GlutaMAX Supplement (Gibco/Thermo Fisher Scientific; Cat. No. 35050-061), 1X MEM Non-Essential Amino Acids (Gibco/Thermo Fisher Scientific; Cat. No. 11140-050), 1X N2 Supplement (Gibco/Thermo Fisher Scientific; Cat. No. 17502-048), 10nM ROCK inhibitor, and 2ug/mL doxycycline (Sigma #D9891). Differentiated neurons were cultured in Cortical Neuron Culture Medium containing the following: BrainPhys Neuronal Medium (STEMCELL Technologies #05790) or BrainPhys without Phenol Red (STEMCELL Technologies #05791) as the base, 1X B27 Supplement (Gibco/Thermo Fisher Scientific; Cat. No. 17504-044), 10ng/mL NT-3 (PeproTech; Cat. No. 450-03), 10ng/mL BDNF (PeproTech; Cat. No. 450-02), 1ug/mL Mouse Laminin (R&D Systems #3446-005-01), and optionally 2µg/mL doxycycline.

Primary mouse astrocytes

Primary mouse astrocytes were isolated from two P1 mouse pups and cultured in T75 in DMEM + 10% FBS. One day after plating neurons, astrocytes were dissociated by trypsin, washed by PBS to remove any remaining FBS and centrifuged at 200g for 5 minutes. The pelleted astrocytes were resuspended in the Classic Neuronal Medium and plated onto the neuronal culture at a 1:5 astrocytes to neurons ratio. Media changes were performed as indicated above for neuronal culture. Once astrocytes were confluent, 2 μM final concentration of AraC was added to the culture.

Molecular Cloning

The CLYBL-targeting constitutive CRISPRi vector pC13N-dCas9-BFP-KRAB was obtained by sub-cloning dCas9-BFP-KRAB from plasmid pHR-SFFV-dCas9-BFP-KRAB downstream of a CAG promoter in the CLYBL-targeting pC13N-iCAG.copGFP vector via BsrGI and AgeI digestion, thus replacing copGFP and generating the plasmid. pHR-SFFV-dCas9-BFP-KRAB was a gift from Stanley Qi & Jonathan Weissman, Addgene plasmid # 46911; http://n2t.net/addgene:46911; RRID:Addgene_46911 (Gilbert et al., 2013) and pC13N-iCAG.copGFP was a gift from Jizhong Zou (Addgene plasmid # 66578; http://n2t.net/addgene:66578; RRID:Addgene_66578 (Cerbini et al., 2015)).

The AAVS1-targeting constitutive CRISPRi vector pMTL3 was obtained by inserting a gene block (gBlock, IDT Technologies) encoding BFP-KRAB into pAAVS1-NC-CRISPRi to create a C-terminal fusion with dCas9, and replacing the

neomycin resistance marker with a puromycin resistance marker. pAAVS1-NC-CRISPRi (Gen3) was a gift from Bruce Conklin (Addgene plasmid # 73499; http://n2t.net/addgene:73499; RRID:Addgene_73499 (Mandegar et al., 2016)). The degron controlled version was generated by inserting a gene-block encoding E. coli dihydrofolate reductase (ecDHFR)–derived degrons with the R12Y, G67S, and Y100I mutations (Iwamoto et al., 2010) to generate an N-terminal fusion with the CRISPRi machinery.

The CLYBL-targeted inducible CRISPRi construct pRT029 was generated by sub-cloning gene blocks encoding E. coli dihydrofolate reductase (ecDHFR)–derived degrons with the R12Y, G67S, and Y100I mutations in the first degron and R12H, N18T and A19V in the second degron (Iwamoto et al., 2010) to generate both an N-terminal and a C-terminal in-frame fusion with dCas9-BFP-KRAB in pC13N-dCas9-BFP-KRAB.

The secondary screening vector pMK1334 was generated as follows: The PpuMI – SnaBI fragment of CROPseq-Guide-Puro was replaced with a gene block encoding the mU6-BstXI-BlpI-optimized sgRNA backbone fragment from our sgRNA vector pCRISPRia-v2 (Addgene plasmid # 84832; http://n2t.net/addgene:84832; RRID:Addgene_84832 (Horlbeck et al., 2016)) to obtain pMK1332. CROPseq-Guide-Puro was a gift from Christoph Bock (Addgene plasmid # 86708; http://n2t.net/addgene:86708; RRID:Addgene_86708 (Datlinger et al., 2017)). Next, the RsrII + PflMI fragment from pMK1332 was replaced by the RsrII + PflMI fragment from pCRISPRia-v2 to introduce tagBFP, creating pMK1333. Last, tagBFP was replaced by a gene block encoding 2xmycNLS-tagBFP2 to obtain pMK1334.

The mNeon-Green-NLS vector (H53) was generated by sub-cloning an EF1α promoter and mNeon-Green with two SV40-NLS into the pMK1333 vector via XhoI and EcoRI digestion, thus replacing the mU6 promoter, the original EF1α promoter, and the original fluorophore. The mScarlet vector (I2) was generated by sub-cloning mScarlet downstream of an EF1α promoter in the H53 vector via BmtI and EcoRI digestion, thus replacing mNeon-Green-NLS.

The GCaMP6m vector (I1) was generated by sub-cloning GCaMP6m downstream of an EF1α promoter in the H53 vector via BmtI and EcoRI digestion, thus replacing mNeon-Green-NLS.

Vector maps are available at kampmannlab.ucsf.edu/resources, and plasmids will be shared on Addgene.

CRISPRi iPS cell line generation

WTC11 iPSCs harboring a single-copy of doxycycline-inducible mouse NGN2 at the AAVS1 locus (Wang et al., 2017, Fernandopulle et al., 2018) were used as the parental iPSC line for further genetic engineering. iPSCs were transfected with pC13N-dCas9-BFP-KRAB and TALENS targeting the human CLYBL intragenic safe harbor locus (between exons 2 and 3) (pZT-C13-R1 and pZT-C13-L1, Addgene #62196, #62197) using DNA In-Stem (VitaScientific). After 14 days, BFP-positive iPSCs were isolated via FACS sorting, and individualized cells were plated in a serial dilution series to enable isolation of individual clones under direct visualization with an inverted microscope (EtaLuma LS 620) in a tissue culture hood via manual scraping. Clones with

heterozygous integration of dCas9-BFP-KRAB (determined using PCR genotyping) were used for further testing. Karyotype testing (Cell Line Genetics) was normal for the clonal line used for further experiments in this study, which we termed CRISPRi-i3N iPSCs. Similarly, we generated the inducible CRISPRi iPSC line by using pRT029 as a donor plasmid, instead of pC13N-dCas9-BFP-KRAB.

NCRM5 iPSCs (Luo et al., 2014) were used as a second parental iPSC line for genetic engineering. iPSCs were transfected using Lipofectamine Stem (ThermoFisher #STEM00003) with Alt-R S.p. HiFi Cas9 Nuclease V3 (Integrated DNA Technologies #1081060), a custom sgRNA targeting the human CLYBL intragenic safe harbor locus (between exons 2 and 3) from Synthego (sequence ATGTTGGAAGGATGAGGAAA), and the following plasmids: pC13N-dCas9-BFP-KRAB, CLYBL-TO-hNGN2-BSD-mApple (Addgene #124229) and pCE-mp53DD (Okita et al., 2013, Addgene #41856). The following day, iPSCs were individualized and plated in a serial dilution series to enable isolation of individual clones under direct visualization with an inverted microscope (EtaLuma LS 620) in a tissue culture hood via manual scraping. While iPSCs were plated in the serial dilution series, 20 μM blasticidin (Gemini Bio-Products #400-165P) was added to the culture medium for 1-4 days to select for clones with successful integration of TO-hNGN2-BSD-mApple. Clones with heterozygous integration of dCas9-BFP-KRAB and TO-hNGN2-BSD-mApple (determined using PCR genotyping) were used for further testing, including functional CRISPRi activity (verified by GRN immunocytochemistry) and neuronal differentiation (verified visually and with TUJ1 immunocytochemistry).

Dissociation of neurons

Papain (Worthington; Code: PAP2; Cat. No.LK003178) was resuspended in 1X Hanks' Balanced Salt Solution (Corning; Cat. No. 21-022-CV) to 20U/mL and warmed at 37°C for 10 minutes. Magnesium chloride was added at 5mM and DNase (Worthington; Code: DPRF; Cat. No. LS006333) was added at 5ug/mL immediately before use. Culture medium was aspirated and human iPSC-derived neurons were washed with DPBS. The papain, magnesium chloride, and DNase solution was added at 250µL per well of a 12-well plate or at 2mL per 10-cm dish and incubated at 37°C for 10 minutes. This dissociation solution was quenched in 5 volumes of DMEM (Gibco/Thermo Fisher Scientific; Cat. No. 10313-039) supplemented with 10% fetal bovine serum for each volume of dissociation solution, and the resulting solution was used to detach and transfer the sheet of cells to the appropriate collection tube format. For DNA, RNA, or protein extraction, the neuron sheet was centrifuged at 200g for 3 minutes, the supernatant was carefully removed with a P1000 pipette, and the pellet was snap frozen in liquid nitrogen. For flow cytometry analysis, the neuron sheet was triturated 10-15 times and centrifuged at 200g for 10 minutes, the supernatant was carefully removed with a P1000 pipette, and the pellet was resuspended in staining solution.

Quantification of knockdown by qPCR

To quantify TFRC or CDH2 knockdown, human iPSCs or neuron cell pellets were thawed on ice, and total RNA was extracted using the Quick-RNA Miniprep Kit (Zymo;

Cat. No. R1054). An input of 100ng RNA was used to synthesize cDNA with the SuperScript III First-Strand Synthesis System (Invitrogen; Cat. No. 18080-051). Samples were prepared for qPCR in technical duplicates in 15µL reaction volumes using SensiFAST SYBR Lo-ROX 2X master mix (Bioline; Cat. No. BIO-94005), custom qPCR primers from Integrated DNA Technologies used at a final concentration of 0.4uM, and cDNA (prepared above) diluted at 1:2 or 1:100 for the target or housekeeping gene, respectively. Quantitative real-time PCR was performed on an Agilent Mx3005P QPCR System with the following Fast 2-Step protocol: 1) 95°C for 2 minutes; 2) 95°C for 5 seconds (denaturation); 3) 60°C for 15 seconds (annealing/extension); 4) repeat steps 2 and 3 for a total of 40 cycles; 5) ramp from 55°C to 95°C to establish melting curve. Expression fold changes were calculated using the ΔΔCt method.

To quantify UBQLN2 or GRN knockdown, total RNA was extracted from Day 11 CRISPRi-i3N neurons on 12-well plates using the Direct-zol 96 RNA Kit (Zymo #R2055). Samples were prepared for RT-qPCR in technical and biological triplicates in 10 µL reaction volumes using the iTaq Universal Probes One-Step Kit (Bio-Rad #172-5141). The following PrimePCR Probe Assays from Bio-Rad were diluted 1:20: GAPDH (Unique Assay ID qHsaCEP0041396), UBQLN2 (qHsaCEP0055207), and GRN (qHsaCEP0057821). Quantitative real-time PCR was performed on a QuantStudio 6 Flex Real-time PCR System (ThermoFisher #4485691). Expression fold changes were calculated using the ΔΔCt method.

Quantification of knockdown by Western Blot

To quantify protein level knockdown of UBQLN2 by UBQLN2 sgRNA in CRISPRi-i3N neurons, neurons with 2 different non-targeting sgRNAs or UBQLN2 sgRNA were lysed and 20ug of total protein from each lysate was loaded into a NuPAGE 4-12% Bis-Tris Gel (Invitrogen, Cat# NP0336BOX). Subsequently, the gel was transferred onto a nitrocellulose membrane, which was then blocked by Odyssey® Blocking Buffer (PBS) (LI-COR, Cat#927-50000), followed by overnight incubation with primary antibodies at 4 degree. The primary antibodies used were Mouse monoclonal anti-β-Actin (8H10D10) (Cell Signaling Technology, Cat#3700) and Rabbit monoclonal anti-UBQLN2 (D7R2Z) (Cell Signaling Technology, Cat#85509). After incubation, the membrane was washed three times with TBST and then incubated with secondary antibodies (LI-COR Cat# 926-32211 and 926-68070) at room temperature for 1hr. The membrane was then washed 3 times with TBST and once with TBS and imaged on the Odyssey Fc Imaging system (LI-COR Cat# 2800). Digital images were processed and analyzed using ImageJ.

Immunocytochemistry

To evaluate N-cadherin (CDH2) knockdown, pre-differentiated neurons were plated in Classic Neuronal Medium with doxycycline on day 0 at 4 x 104 cells per well on sterilized, Matrigel-coated 12mm diameter round glass coverslips (Ted Pella Inc; Cat. No. 26023) placed in 24-well plates. One day later, primary rat cortical astrocytes (gift from Li Gan) were plated in Classic Neuronal Medium with doxycycline on the same

coverslips (co-culture) at 8 x 103 cells per well. On days 7 and 14, half of the medium was removed and an equal volume of fresh Classic Neuronal Medium without doxycycline was added. On day 18, culture medium was aspirated from each well and cells were subsequently washed with DPBS. Cells were then fixed with 4% paraformaldehyde, which was prepared by diluting 16% paraformaldehyde (Electron Microscopy Sciences; Cat. No. 15710) 1:4 in DPBS, at room temperature for 15 minutes. Paraformaldehyde was removed with a P1000 pipette and collected for proper disposal, and coverslips were washed three times with DPBS for 5 minutes each. Cells were blocked with 2.5ug/mL Mouse BD Fc Block (BD Biosciences; Cat. No. 553141) at room temperature for 15 minutes and subsequently incubated with 1uL mouse IgG1k anti-human CD325 antibody conjugated to APC (BioLegend; Cat. No. 350808) in 50uL of Fc Block at room temperature for 45 minutes. Coverslips were then washed once with DPBS for 5 minutes, incubated with 1ug/mL Hoechst 33342 (Thermo Fisher Scientific; Cat. No. H3570) diluted in DPBS at room temperature for 10 minutes, and then washed twice more with DPBS for 5 minutes each. One drop of Aqua Poly Mount (Polysciences; Cat. No. 18606)

To evaluate progranulin (GRN) knockdown, pre-differentiated neurons were plated in Cortical Neuron Culture Medium with doxycycline on Day 0 at 3.0 x 105 cells per well on poly-L-ornithine-coated 8-well glass-bottom slides (Ibidi #80827). On day 5, culture medium was aspirated from each well and cells were subsequently washed with PBS. Cells were fixed with 4% paraformaldehyde, which was prepared by diluting 16% paraformaldehyde (Electron Microscopy Sciences; Cat. No. 15710) 1:4 in PBS, at room

temperature for 30 minutes. Paraformaldehyde was removed with a P1000 pipette and collected for proper disposal, and slides were washed three times with PBS. Cells were blocked with 3% donkey serum with 0.1% saponin in PBS at room temperature for one hour and subsequently incubated with goat anti-human progranulin antibody diluted 1:3000 (R&D Systems #AF2420) and mouse anti-human TUJ1 antibody (BioLegend #801201) diluted 1:1000 in blocking buffer at 4°C overnight. Slides were then washed three times with PBS and incubated with donkey anti-goat IgG conjugated to AF-488 or AF-647 (Jackson ImmunoResearch #705-545-147 or #705-605-147) and donkey anti-mouse IgG conjugated to RRX or AF-488 (Jackson ImmunoResearch #715-295-151 or #715-545-151) diluted 1:2000 in blocking buffer at room temperature for one hour. Slides were again washed three times with PBS, and incubated with 5 uM DRAQ5 (Thermo Fisher Scientific #62251) in blocking buffer at room temperature for 30 minutes.

To evaluate neuronal differentiation, pre-differentiated neurons were resuspended in Cortical Neuron Culture Medium with doxycycline (2 ug/uL), then plated on poly-L-ornithine-coated 96-well culture dishes (Perkin Elmer #6055308) at a density of 7.5×104 cells/well (n=6 wells per sgRNA). On day 14, culture medium was aspirated from each well on one set of plates and cells were subsequently washed with PBS. Cells were fixed with 4% paraformaldehyde, which was prepared by diluting 16% paraformaldehyde (Electron Microscopy Sciences; Cat. No. 15710) 1:4 in PBS, at room temperature for 15 minutes. Paraformaldehyde was removed and collected for proper disposal, and the plate was washed three times with PBS. Cells were blocked with 5%

donkey serum and 0.1% Triton X-100 in PBS at room temperature for 2.5 hours and subsequently incubated with guinea pig anti-NeuN antibody (MilliporeSigma #ABN90) diluted 1:1000 in blocking buffer at 4°C overnight. The plate was then washed three times with PBS and incubated with goat anti-guinea pig IgG conjugated to AF-647 (ThermoFisher Scientific #A-21450) diluted 1:1000 in blocking buffer at room temperature for 2.5 hours. Plates were again washed three times with PBS. Cells without sgRNA were then incubated with 4 uM Hoechst 33342 (Thermo #62249) for 30 minutes at room temperature, and subsequently washed three times with PBS. i3N iPSCs plated on Ibidi slides were stained alongside the neurons for comparison. For NeuN quantification, stained neurons were imaged with a spinning disk confocal microscope with a motorized stage (Nikon Eclipse Ti), controlled using Nikon Elements software. A 20X objective was used to acquire a series of 36 slightly overlapping images within each well followed by image stitching.

DNA damage assay

CRISPRi-i3N iPSCs were infected by non-targeting sgRNA or 2 different MAT2A sgRNAs for 48hrs on Matrigel-coated 96-well plates. Cells with no treatment and with 1uM Etoposide treatment for 6hrs were used as negative and positive controls, respectively. These cells were fixed by 4% paraformaldehyde for 15 mins followed by permeabilization by 0.1% Triton for 10 mins. After that, the cells were blocked with 5% goat serum and 0.1% Triton X-100 in PBS at room temperature for 1 hour and subsequently incubated with mouse anti-H2AX pS139 antibody (Millipore #05-636)

diluted in blocking buffer at a final concentration of 2 µg/ml overnight at 4 degree. Following incubation, the cells were washed three times with PBS and incubated with goat anti-mouse IgG conjugated to Alexa Fluor 488 (Abcam, Cat#ab150113) at room temperature for 1hr. Cells were then washed three times with PBS. Untreated cells and Etoposide treated cells were incubated with 1uM Hoechst 33342 (Thermo #62249) for 30 minutes at room temperature. For quantification, stained iPSCs were imaged using an InCell 6000 (GE Cat# 28-9938-51) at 60X and H2AX foci were quantified using CellProfiler (Carpenter et al., 2006).

Calcium Imaging

i3N iPSCs and CRISPRi-i3N iPSCs were lentivirally transduced with the GCaMP6m vector (I1). These polyclonal iPSCs were passaged and plated at a density of 5.0×104 cells/well in Matrigel-coated 6-well culture plates. Shortly afterwards, half of the wells with iPSCs were transduced with lentivirus containing non-targeting sgRNA. The following day, media was changed to E8 + RI. Two days after infection, the media was changed to E8 + 12 ug/mL puromycin (Sigma #P9620-10ML) to select for transduced cells.

Following selection for 3-4 additional days, the iPSCs were passaged into fresh Matrigel-coated 6-well culture plates at a high density and allowed to differentiate in Induction Medium with doxycycline (2 ug/mL) for 3 days, with daily media changes.

Following the 3 days of differentiation, these partially-differentiated neurons were passaged and resuspended in Cortical Neuron Culture Medium with doxycycline (2 ug/uL), then plated on poly-L-ornithine-coated 96-well culture dishes (Perkin Elmer #6055308) at a density of 7.5×104 cells/well (n=6 wells per sgRNA). For the remainder of the experiment before imaging, half of the culture medium was removed and an equal volume of fresh medium was added three times per week. On day 28, half of the culture medium was aspirated from each well. Neurons were imaged with a spinning disk confocal microscope with a 37 °C heated chamber and a motorized stage (Nikon Eclipse Ti), controlled using Nikon Elements software. A 20X objective was used to acquire 30-second movies of one field per well (n = 4-6 wells) at approximately 5 frames/second. Following the initial acquisition, culture medium containing CNQX (Tocris #1045) at a final concentration of 50 uM was added to each well. Beginning one minute after CNQX addition, the same fields were imaged as previously.

Primary CRISPRi screen

The CRISPRi v2 H1 library with top 5 sgRNAs per gene (Horlbeck et al., 2016) was packaged into lentivirus for transduction of iPSCs as follows. Two 15-cm dishes were each seeded with 8 x 106 HEK293T cells in 20 mL DMEM complete (basal medium supplemented with 10% FBS and 1% penicillin/streptomycin). The next day, H1 library transfection mix was prepared in the following manner: 10ug H1 library plasmid and 10ug third generation packaging mix (1:1:1 mix of the three plasmids) were diluted into 2mL Opti-MEM I Reduced Serum Medium (Gibco; Cat. No. 31985070); 250uL

Lipofectamine 2000 Transfection Reagent (Invitrogen; Cat. No. 11668027) was diluted into 2mL Opti-MEM and incubated at room temperature for 5 minutes; the diluted DNA solution was added to the diluted Lipofectamine solution, inverted several times to mix, and incubated at room temperature for 15 minutes. Following incubation, half of the transfection solution was gently added dropwise to each 15-cm dish with HEK293T cells, and the plates were briefly and gently moved in a figure-eight pattern to mix. Eight hours later, the Lipofectamine-containing media on each dish was carefully aspirated and replaced with 20mL DMEM complete supplemented with 40uL ViralBoost (Alstem; Cat. No. VB100; diluted 1:500 in media). Two days later, HEK293T media (approximately 40mL) was transferred to a 50mL conical and centrifuged at room temperature for 10 minutes at 300g to pellet cell debris. The supernatant was carefully transferred to a syringe fitted with a 0.45um filter in order to filter the virus-containing solution into a new 50mL conical. Approximately 10mL of cold Lentivirus Precipitation Solution (Alstem; Cat. No. VC100) was added to this filtered solution, which was then mixed well and stored at 4°C for 48 hours. Following incubation, the solution was centrifuged at 4°C for 30 minutes at 1,500g, and the supernatant was decanted. A second centrifugation at 4°C for 5 minutes at 1,500g was performed, and the remaining supernatant was removed with a P1000 pipette. The virus-containing pellet was resuspended in 20mL Essential 8 iPSC medium with ROCK inhibitor.

For infection with the H1 library, two T175 Matrigel-coated flasks were each seeded with 2 x 107 CRISPRi-i3 N iPSCs in 10mL of the virus-containing medium and left in the tissue culture hood for 15 minutes to allow even distribution and attachment

before moving to the incubator. Six hours later, an additional 15mL of Essential 8 medium with ROCK inhibitor was added to each flask without removing the virus-containing medium. The next day, we performed a complete media change on all flasks, adding 35mL Essential 8 medium with ROCK inhibitor to allow the cells to recover and proliferate. One day later, we released the cells and seeded four T175 Matrigel-coated flasks each with 1 x 107 cells in 20mL Essential 8 medium with ROCK inhibitor, which was the medium volume and formulation used for puromycin treatment to enrich sgRNA-expressing cells. The initial MOI, quantified as the fraction of BFP-positive cells by flow cytometry, was ~15%, corresponding to a library representation of ~450 cells per library element. Puromycin treatment proceeded in the following manner: two days with 0.8ug/mL puromycin, followed by two days with 1ug/mL puromycin. At the end of treatment, cells were assessed by flow cytometry (83% expressed high levels of BFP) and seeded for the iPSC and neuronal survival screens, which are described below.

For the iPSC growth-based screen, two T175 Matrigel-coated flasks were each seeded with 1 x 107 cells in 20mL Essential 8 medium with ROCK inhibitor (timepoint t0), corresponding to a library representation of ~1,200 cells per library element. Approximately 2 x 107 t0 cells were also snap frozen in liquid nitrogen for downstream sample preparation to represent the Day 0 sample, corresponding to a library representation of ~1,200 cells per library element. Media was replaced on day two (t2), omitting ROCK inhibitor. Cells were released on day three (t3), and each replicate was seeded into two new T175 Matrigel-coated flasks with 1 x 107 cells each in 20mL

Essential 8 medium with ROCK inhibitor. Media was replaced on day five (t5), omitting ROCK inhibitor. Cells were released on day six (t6), cells within the same replicate were mixed across flasks, and each replicate was seeded into two new T175 Matrigel-coated flasks with 1 x 10 cells each in 20mL Essential 8 medium with ROCK inhibitor. Media was replaced on days eight (t8) and nine (t9), omitting ROCK inhibitor. Cells were released on day ten (t10), cells within the same replicate were mixed across flasks, and 4 x 107 cells from each replicate were snap frozen for downstream sample preparation, corresponding to a library representation of ~2,500 cells per library element

For the neuronal survival screen, twelve 10-cm Matrigel-coated dishes were each seeded with 4 x 106 iPSCs in N2 Pre-Differentiation Medium (day-3) and differentiated as previously described. However, an additional full media change (10mL) was performed on Day 4 to remove cellular debris that started to appear. On Days 14, 21, and 28, dead (floating cells) were removed and live (adherent) cells from two 10-cm dishes were harvested per replicate per timepoint. Since neuronal death occurred over time, the estimated library representation for these time points was ~410 cells/library element on Day 14, ~380 cells/library element on Day 21, and ~330 cells/library element on Day 28. Adherent cells were released by papain as previously described, and pelleted cells were snap frozen for downstream sample preparation. Genomic DNA was extracted with the NucleoSpin Blood L or XL kits (Macherey Nagel; Cat. No. 740954.20 or 740950.10, respectively) and samples were prepared for sequencing on an Illumina HiSeq-4000 based on previously described protocols (Gilbert et al., 2014; Kampmann et al., 2014).

Pooled validation screen

192 sgRNAs, including 184 sgRNAs targeting 92 selected hit genes from the primary screen (two sgRNAs per gene) and 8 non-targeting control sgRNAs, were individually cloned into the secondary screening vector pMK1334 and verified by Sanger sequencing. The plasmid was pooled and lentivirus was produced as for the Primary Screen. CRISPRi-i3N iPSCs were transduced with the pool at 70% MOI (quantified as fraction of BFP-positive cells by flow cytometry) and were transduced cells selected by 1 ug/ml of puromycin to obtain a population of cells that was ~85% BFP-positive. Following 3 days of expansion, approximately 2 million of these cells were harvested as Day 0 sample (corresponding to a library representation of ~9,000 cells/library element) and the rest of cells were cultured as iPSCs (as described in 'Human iPS cell culture') or differentiated into glutamatergic neurons (as described in 'Human neuronal culture'). For the iPSC growth screen, iPSCs were cultured in E8 medium with daily medium change in two T25 flasks as duplicates and were passaged every 2-3 days till Day 10. Approximately 2 million of Day 10 iPSCs from each replicate were harvested, corresponding to a library representation of ~9,000 cells/library element. For the mono-culture neuronal screen, 10 million of pre-differentiated neurons were plated in one Poly-D-Lysine coated 15-cm dish (Corning; Cat. No. 354550). Two replicate dishes of neurons were cultured in Classic Neuronal Medium as described in 'Human neuronal culture'. Live neurons were harvested on Day 14 and Day 28 neurons as described for the primary screens; the library representation was ~35,000 cells /

library element on Day 14 and ~28,000 cells / library element on Day 28. For the co-culture neuronal screen, 1.5 million of primary mouse astrocytes were added into one Poly-D-Lysine coated 15-cm dish containing 7.5 million neurons. Two replicate dishes of neurons in co-culture were cultured as described in 'Astrocyte co-culture'. Day 14 neurons from each replicate of co-culture experiment were harvested, the library representation was ~50,000 neurons/library element. Genomic DNA was isolated from all harvested samples using a commercial kit (Macherey Nagel; NucleoSpin® Blood). The sgRNA-encoding region were then amplified and sequenced as in the Primary Screen.

CROP-Seq

CRISPRi-i3N iPSCs were infected with a pool of selected sgRNAs in the CROP-Seq vector pMK1334 at a low multiplicity of infection to minimize double infection. After puromycin selection and expansion, cells were either passaged as iPSCs or differentiated into neurons. Approximately 20,000 iPSCs and 20,000 day 7 i3Neurons were captured by the 10X Chromium Controller using Chromium Single Cell 3' Library & Gel Bead Kit v2 (10X Genomics; Cat. No. 120267) with 10,000 input cells per lane. Sample prep was performed according to protocol, holding 10-30 ng full-length cDNA for sgRNA-enrichment PCR.

To facilitate sgRNA assignment, sgRNA-containing transcripts were additionally amplified by hemi-nested PCR reactions by adapting a previously published approach (Hill et al., 2018). Briefly, in the first PCR reaction, 15ng of full-length cDNA was used as

template and Enrichemnt_PCR_1_For and Enrichemnt_PCR_1_Rev were used as primers. PCR product was cleaned up by 1.0x SPRI beads (SPRIselect; BECKMAN COULTER; Cat. No. B23317) and 1ng cleaned product was input into the second PCR reaction using Enrichemnt_PCR_2_For and Enrichemnt_PCR_2_Rev as primers. Following 1.0x SPRI beads clean up, 1 ng of the PCR product from the second PCR reaction was used as template in the final PCR, in which reverse primer Enrichemnt_PCR_2_Rev and a forward primer, Enrichemnt_PCR_3_For, containing an i7 index, were used as primers. All PCR reactions were carried out for 18 cycles using KAPA HiFi polymerase (KAPA HiFi HotStart ReadyMix (2X); Cat. No. KK2602) with annealing temperature at 62 degree and 15 seconds extension per cycle. The sgRNA-enrichment libraries were separately indexed and sequenced as spike-ins alongside the whole-transcriptome scRNA-Seq libraries using a NovaSeq 6000 using the following configuration: Read 1: 26, i7 index: 8, i5 index: 0, Read 2: 98.

Quant-Seq

Neurons cultured in 12-well plates were released with papain, pelleted, and snap frozen on days 0, 14, 21, 28, and 35 in technical duplicates (approximately 2 x 105 cells each) per timepoint. RNA was extracted using the Quick-RNA Miniprep Kit (Zymo; Cat. No. R1054), and RNA concentrations were determined with the Qubit RNA HS Assay Kit (Invitrogen; Cat. No. Q32855) on a Qubit 2.0 Fluorometer (Invitrogen; Cat. No. Q32866). mRNA-Seq libraries were prepared from an input of 184ng total RNA in 5uL using the QuantSeq 3’ mRNA-Seq Library Prep Kit FWD for Illumina (Lexogen; Cat. No. 015). Briefly, oligodT hybridization enabled mRNA-selective reverse transcription. The

original RNA template was then degraded, and second strand cDNA synthesis was achieved by random priming and extension by DNA polymerase. Samples were subsequently subjected to magnetic bead-based purification, followed by library amplification with indexed flow-cell adapters (14 PCR cycles) and another round of magnetic bead-based purification. mRNA-Seq library concentrations (mean of 1.01 ± 0.275 ng/uL) were measured with the Qubit dsDNA HS Assay Kit (Invitrogen; Cat. No. Q32851) on a Qubit 2.0 Fluorometer. Library fragment-length distributions (mean of 371 ± 16.1 bp) were quantified with the High Sensitivity DNA Kit (Agilent; Cat. No. 5067-4626) on a 2100 Bioanalyzer Instrument (Agilent; Cat. No. G2939BA). All libraries were diluted to 2.72nM for equimolar representation in the final, pooled sample. Single-end sequencing was performed, generating reads toward the poly(A) tail.

Longitudinal CRISPRi-i3Neuron imaging screen

CRISPRi-i3N iPSCs were transduced with lentivirus expressing mNeonGreen-NLS and FACS-sorted for the brightest green population. These polyclonal cells will be referred to as nuclear-green CRISPRi-i3N iPSCs. Subsequently, a fraction of these iPSCs were transduced with lentivirus expressing cytosolic mScarlet and FACS sorted for the brightest red and green cells. These polyclonal iPSCs will be referred to as the nuclear-green/cytosolic red CRISPRi-i3N iPSCs.

The arrayed sgRNAs in the pMK1334 vector were packaged into lentivirus for transduction of iPSCs as follows: 6-well plates coated with poly-D-lysine were seeded with 2.5 x 106 HEK293T cells per well in 1.5 mL of DMEM complete (basal medium

supplemented with 10% FBS) each. The next day, the arrayed transfection mixes were prepared in the following manner: 1.2ug sgRNA plasmid and 1.2 ug packaging mix (0.8ug psPAX2, 0.3ug pMD2G, 0.1ug pAdVantage), along with 5 uL P3000 reagent (ThermoFisher Scientific # L3000015) were diluted into 150 uL Opti-MEM I Reduced Serum Medium (Gibco; Cat. No. 31985070); 3.75 uL Lipofectamine 3000 Transfection Reagent (ThermoFisher Scientific # L3000015) was diluted into 150 uL Opti-MEM and incubated at room temperature for 5 minutes; the diluted Lipofectamine solution was added to the diluted DNA solution, flicked to mix, and incubated at room temperature for 20 minutes. Following incubation, the transfection solutions were gently added dropwise to each well with HEK293T cells, and the plates were briefly and gently moved in a figure-eight pattern to mix. The following day, the Lipofectamine-containing media on each well was carefully aspirated and replaced with 3mL DMEM complete supplemented with 6uL ViralBoost (Alstem; Cat. No. VB100; diluted 1:500 in media). Three days later, HEK293T media from each well was transferred to one well each of two 2mL deep 96-well dishes (USA Scientific #1896-2800) and centrifuged at 4°C for 30 minutes at 3428g to pellet cell debris. Viral supernatant was stored at 4°C.

For functional titering of the lentivirus, nuclear-green+ CRISPRi-i3N iPSCs were passaged and plated at a density of 1.0 x 104 cells/well in Matrigel-coated 96-well culture dishes. Following adherence of iPSCs, 75 uL of each viral supernatant was added to one well, and a series of half-volume dilutions was performed for a total of four dilutions. The following day, the culture medium containing the lentivirus was carefully aspirated and replaced with fresh medium. Three days after infection, iPSCs were

imaged with a spinning disk confocal microscope with a motorized stage (Nikon Eclipse Ti), controlled using Nikon Elements software. A 20X objective was used to acquire a series of 36 slightly overlapping images within each well followed by image stitching. The ratio of cells infected with lentivirus was quantified via Nikon Elements software as the number of green nuclei with blue signal above an intensity threshold divided by the total number of green nuclei. The volumes of viral supernatant used in all subsequent infections were adjusted based on the differences between infection ratios.

Nuclear-green+ cytosolic red+ CRISPRi-i3N iPSCs were passaged and plated at a density of 2.5×104 cells/well in Matrigel-coated 12-well culture plates. Shortly afterwards, the iPSCs were transduced with lentivirus containing individual sgRNAs. The following day, media was changed to E8 + RI. Two days after infection, the media was changed to E8 + puromycin (12 ug/mL) to select for transduced cells.

Following selection for 3-4 additional days, the iPSCs were passaged into fresh Matrigel-coated 12-well culture plates at a high density and allowed to differentiate in Induction Medium with doxycycline (2 ug/mL) for 3 days, with daily media changes. Concurrently, the uninfected nuclear-green CRISPRi-i3N iPSCs were differentiated alongside the infected nuclear-green+blue/cytosolic red CRISPRi-i3N iPSCs.

Following the 3 days of differentiation, these partially-differentiated neurons were passaged and resuspended in Cortical Neuron Culture Medium with doxycycline (2 ug/uL), then plated on poly-L-ornithine-coated 96-well culture dishes (Perkin Elmer #6055308) at a density of 5.0×104 cells/well (n=6 wells per sgRNA for most, 3-5 for some). The nuclear-green+blue/cytosolic red CRISPRi-i3Neurons were spiked in at a

density of 1:20 with the nuclear-green CRISPRi-i3Neurons to facilitate tracing of neurites while maintaining trophic support of higher-density neuron cultures. Following plating, we waited for adherence of neurons before imaging for the first time. For the remainder of each longitudinal imaging experiment, half of the culture medium was removed and an equal volume of fresh medium was added three times per week.

For each timepoint, CRISPRi-i3Neurons were imaged with a spinning disk confocal microscope with a motorized stage (Nikon Eclipse Ti), controlled using Nikon Elements software. A 20X objective was used to acquire a series of 25 slightly overlapping images within each well followed by image stitching. Between imaging sessions, plates were incubated in a traditional water-jacketed 5% CO2 incubator at 37°C.

Longitudinal iPSC imaging screen

Nuclear-green CRISPRi-i3N iPSCs were passaged and plated in Matrigel-coated 96-well culture dishes at a density of 1,000 cells/well. Following adherence, iPSCs were transduced with lentivirus (same preparation as for the longitudinal neuronal imaging) containing individual sgRNAs (n=3 wells per sgRNA). The following day, media was changed to E8 + ROCK inhibitor. Starting two days after infection, iPSCs were imaged with a spinning disk confocal microscope with a motorized stage (Nikon Eclipse Ti), controlled using Nikon Elements software. A 20X objective was used to acquire a series of 36 slightly overlapping images within each well followed by image stitching. Between

imaging sessions, plates were incubated in a traditional water-jacketed 5% CO2 incubator at 37 °C.

Longitudinal imaging for CRISPRi toxicity

i3N iPSCs and inducible CRISPRi-i3N iPSCs were transduced with lentivirus expressing only mNeonGreen-NLS, and/or with lentivirus expressing cytosolic mScarlet. These polyclonal iPSC groups will be referred to as the nuclear-green iPSCs and nuclear-green/cytosolic red iPSCs, respectively. Nuclear-green/cytosolic red iPSCs were passaged and plated at a density of 5.0×104 cells/well in Matrigel-coated 6-well culture plates. Shortly afterwards, half of the wells with iPSCs were transduced with lentivirus containing non-targeting sgRNA. The following day, media was changed to E8 + RI. Two days after infection, the media was changed to E8 + puromycin (12 ug/mL) to select for transduced cells. Following selection for 3-4 additional days, the iPSCs were passaged into fresh Matrigel-coated 12-well culture plates at a high density and allowed to differentiate in Induction Medium with doxycycline (2 ug/mL) for 3 days, with daily media changes. Concurrently, the uninfected nuclear-green iPSCs were differentiated alongside the nuclear-green/cytosolic red iPSCs. Following the 3 days of differentiation, these partially-differentiated neurons were passaged and resuspended in Cortical Neuron Culture Medium with doxycycline (2 ug/uL), then plated on poly-L-ornithine-coated 96-well culture dishes (Perkin Elmer #6055308) at a density of 5.0×104 cells/well (n=6 wells per sgRNA). The inducible CRISPRi-i3N neurons were plated in two groups, with or without 20 uM TMP (Sigma #92131-5G) in the culture

medium. The nuclear-green/cytosolic red neurons were spiked in at a density of 1:20 with the nuclear-green neurons to facilitate tracing of neurites while maintaining trophic support of higher-density neuron cultures. Following plating, we waited for adherence of neurons before imaging for the first time. For the remainder of each longitudinal imaging experiment, half of the culture medium was removed and an equal volume of fresh medium was added three times per week. For each timepoint, neurons were imaged with a spinning disk confocal microscope with a motorized stage (Nikon Eclipse Ti), controlled using Nikon Elements software. A 20X objective was used to acquire a series of 25 slightly overlapping images within each well followed by image stitching. Between imaging sessions, plates were incubated in a traditional water-jacketed 5% CO2 incubator at 37 °C.

Pharmacological validation of HMGCR phenotype

CRISPRi-i3N cells infected with non-targeting control sgRNA or HMGCR sgRNA were seeded into 96- or 384-well plates on Day 0 into Brainphys media containing mevastatin (compactin, Sigma #M2537) or mevalonate (Sigma #M4667) at the concentrations indicated in Fig. 2E,F. Images were taken daily and half-media changes performed every second day, with half-concentrations of the treatments used when refreshing media.

QUANTIFICATION AND STATISTICAL ANALYSIS

Quant-Seq analysis

Fastq files were uploaded to and processed through the cloud-based BlueBee Genomics Platform (https://www.bluebee.com/quantseq). Briefly, raw reads were trimmed with Bbduk, aligned with STAR Aligner, and counted with HTSeq-count to yield gene counts. Differential expression analyses were performed with the DESeq2 pipeline, which compared counts from each set of duplicates at different timepoints to counts from the day 0 timepoints. Additional, custom analysis pipelines were devised in R. We developed a simple web application with the Shiny R package that enables users to visualize normalized read counts and expression fold change (relative to day 0) throughout neuronal differentiation for a queried gene. The web application can be accessed via kampmannlab.ucsf.edu/ineuron-rna-seq.

Primary screen analysis

We developed a bioinformatics pipeline, MAGeCK-iNC (MAGeCK including Negative Controls) for large-scale functional genomics analysis, which we made publicly available (kampmannlab.ucsf.edu/mageck-inc). First, raw sequencing reads from next-generation sequencing were cropped and aligned to the reference using Bowtie (Langmead et al., 2009) to determine sgRNA counts in each sample. Next, counts files of two samples subject to comparison were input into MAGeCK and $\log_2$ fold changes (LFCs) and P values were calculated for each sgRNA using the 'mageck test –k' command. Following that, gene level knockdown phenotype scores were determined by

averaging LFCs of the top 3 sgRNAs targeting this gene with the most significant P values. The statistical significance for each gene was determined by comparing the set of P values for sgRNAs targeting it with the set of P values for non-targeting control sgRNAs using the Mann-Whitney U test, as described previously (Kampmann et al., 2013, 2014). To correct for multiple hypothesis testing, we first performed random sampling of 5 with replacement from non-targeting control sgRNAs to generate 'negative-control-quasi-genes' and calculated knockdown phenotype scores and P values for each of them. Then, we calculated the hit strength, defined as the product of knockdown phenotype score and –log (p value), for all genes in the library and for 'negative-control-quasi-genes' generated above. Based on the distribution of all the products, a cutoff value was chosen to make sure the false-discovery rate (FDR) is less than 0.05. To find enriched annotations within hit genes, Gene Set Enrichment Analysis (GSEA) was performed for Day 10 iPSCs and Day 28 neurons using the fgsea package in R (Sergushichev, 2016).

Pooled validation screen analysis

sgRNA counts for each sample were determined as in primary screen. Subsequently, knockdown phenotype scores for each sgRNA were calculated as LFCs of sgRNA counts between two samples and were normalized by subtracting the median of non-targeting control sgRNAs. LFCs were averaged for samples with replicates. Gene-level knockdown phenotype score was determined as the mean of knockdown phenotype scores of all sgRNAs targeting this gene.

CROP-Seq analysis

Cell Ranger (version 2.2.0, 10X Genomics) with default parameters was used to align reads and generate digital expression matrices from single-cell sequencing data. To map sgRNA transcripts together with other mRNA transcripts to individual cells, a custom reference was generated by extending the human genome assembly (Ensembl GRCh38 release) with 'quasi-genes' representing sgRNA-containing transcripts (one sgRNA sequence per quasi-gene with 250bp upstream and 230bp downstream sequences). Sequencing results of sgRNA-enrichment libraries were analyzed using methods previously described (Hill et al., 2018) to further facilitate sgRNA identity assignment.

For a given cell, sgRNA(s) whose UMI counts were greater than 4 standard deviations of the mean UMI counts of all sgRNAs were assigned to that cell as its identity. Cells with only one assigned sgRNA were retained for further analysis. The Scater package (McCarthy et al., 2017) implemented in R was used to analyze the digital expression matrices including normalization, quality control and filtering.

The mean reads per cell was around 84,000 for iPSCs and 91,000 for neurons. Median number of genes detected per cell was around 5,000 for iPSCs and 4,600 for neurons. After quality control, a single sgRNA could be assigned to ~15,000 iPSCs and ~8,400 neurons

For each target gene, the top 50% cells with best on-target knockdown were retained. Differential gene expression analysis was performed between each gene

knockdown group (cells assigned by targeting sgRNAs of that gene) and control group (cells assigned by non-targeting control sgRNAs) using the R package edgeR (Robinson et al., 2010) treating each cell as one replicate.

For Fig. 2.7C, relative expression of each gene was calculated as z-normalized expression with respect to the mean and standard deviation of that gene in the control group:

$$x_{normalized} = \frac{x - \mu_{control}}{\sigma_{control}}$$

The top 20 most significantly altered genes were selected for each gene knockdown group and merged together to form the signature gene list. Gene knockdown groups were hierarchically clustered based on their relative expression of the signature genes, using Cluster 3.0 (Eisen et al., 1998) and visualized using Java TreeView (Saldanha, 2004).

For Fig. 2.11E, GSEA was performed using the web tool WebGestalt (Zhang et al., 2005). For Fig. 2.9C,D, the similarity score of transcriptome changes between two gene knockdown groups, A and B, was calculated as follows:

$$Similarity_{A,B} = \frac{|A_{up} \cap B_{up}| + |A_{down} \cap B_{down}|}{|A_{up} \cup B_{up}| + |A_{down} \cup B_{down}|}$$

Aup and Bup denote for the significantly upregulated genes (padj<0.01) in A and B, while Adown and Bdown denote for the significantly downregulated genes (padj<0.01) in A and B.

Longitudinal imaging data analysis

A CellProfiler (Carpenter et al., 2006) pipeline was developed to analyze longitudinal imaging data. For iPSC growth and i3Neuron survival experiments, sgRNA+ cells were recognized as nuclear-green+ blue+ objects and the total number of sgRNA+ cells was quantified for every image. iPSC growth and i3Neuron survival were calculated as the ratio of sgRNA+ cell number at different time points to that of day 1 of imaging. For neurite morphology analysis, neurites of sgRNA+ cells were first enhanced by the EnhanceOrSuppressFeatures and EnhanceEdges modules, and then skeletonized by the Morph module. Following that, MeasureObjectSkeleton module was implemented to measure neurite length, number of branches and number of trunks for individual neurons. The mean values of the above measurements of all sgRNA+ neurons were calculated for each image.

To integrate all image analysis data, we generated a panel of imaging phenotypes for a given sgRNA, including neurite length, number of neurite branches, number of neurite trunks, neuronal survival and iPSC growth at different time points. For Fig. 2.12E, the percentage changes of imaging phenotypes compared to the mean of non-targeting control sgRNAs were calculated for each sgRNA. Most of genes in the imaging experiment were targeted by two sgRNAs (some genes missed one sgRNA during experiment process), and a gene was discarded if it was targeted by two sgRNAs and the correlation of the two sgRNAs was less than 0.8. All remaining sgRNAs were hierarchically clustered based on the Pearson correlation of their

percentage changes of imaging phenotypes, using Cluster 3.0 (Eisen et al., 1998) and visualized using Java TreeView (Saldanha, 2004).

Calcium Imaging Analysis

Representative GCaMP6m movies for each cell group were chosen manually, after viewing all movies for each group. Representative movies before and after CNQX addition were merged sequentially and aligned using Nikon Elements software. For each merged and aligned movie, ROIs were drawn manually with Fiji (Schindelin et al., 2012) around every clearly visible cell body, and the mean gray value was measured for each ROI in each frame. For each ROI, ΔF/F was calculated using the average of the 5 frames with the lowest values as the baseline.

DATA AND SOFTWARE AVAILABILITY

RNA sequencing data sets generated in this study are available on NCBI GEO as dataset GSE124703 (https://www.ncbi.nlm.nih.gov/geo/query/acc.cgi?acc=GSE124703).

Expression levels of genes of interest at different time points during neuronal differentiation can be visualized interactively at kampmannlab.ucsf.edu/ineuron-rna-seq.

Longitudinal imaging data files will be made available on request to the lead author. The MAGeCK-iNC bioinformatics pipeline is available at kampmannlab.ucsf.edu/mageck-inc.

The CellProfiler pipeline for analysis of neuronal longitudinal imaging data will be made available on request to the lead author, and will also be submitted to the CellProfiler depository of published pipelines (https://cellprofiler.org/examples/published_pipelines.html) upon publication.

REFERENCES

Adamson, B., Norman, T.M., Jost, M., Cho, M.Y., Nunez, J.K., Chen, Y., Villalta, J.E., Gilbert, L.A., Horlbeck, M.A., Hein, M.Y., et al. (2016). A Multiplexed Single-Cell CRISPR Screening Platform Enables Systematic Dissection of the Unfolded Protein Response. Cell 167, 1867-1882 e1821.

Adamson, B., Smogorzewska, A., Sigoillot, F.D., King, R.W., and Elledge, S.J. (2012). A genome-wide homologous recombination screen identifies the RNA-binding protein RBMX as a component of the DNA-damage response. Nat Cell Biol 14, 318-328.

Cantallops, I., Haas, K., and Cline, H.T. (2000). Postsynaptic CPG15 promotes synaptic maturation and presynaptic axon arbor elaboration in vivo. Nature neuroscience 3, 1004-1011.

Carpenter, A.E., Jones, T.R., Lamprecht, M.R., Clarke, C., Kang, I.H., Friman, O., Guertin, D.A., Chang, J.H., Lindquist, R.A., Moffat, J., et al. (2006). CellProfiler: image analysis software for identifying and quantifying cell phenotypes. Genome biology 7, R100.

Cerbini, T., Funahashi, R., Luo, Y., Liu, C., Park, K., Rao, M., Malik, N., and Zou, J. (2015). Transcription activator-like effector nuclease (TALEN)-mediated CLYBL targeting enables enhanced transgene expression and one-step generation of dual reporter human induced pluripotent stem cell (iPSC) and neural stem cell (NSC) lines. PloS one 10, e0116032.

Choi, Y., Lee, K., Ryu, J., Kim, H.G., Jeong, A.Y., Woo, R.S., Lee, J.H., Hyun, J.W., Hahn, S., Kim, J.H., et al. (2014). Neuritin attenuates cognitive function impairments in tg2576 mouse model of Alzheimer's disease. PloS one 9, e104121.

Datlinger, P., Rendeiro, A.F., Schmidl, C., Krausgruber, T., Traxler, P., Klughammer, J., Schuster, L.C., Kuchler, A., Alpar, D., and Bock, C. (2017). Pooled CRISPR screening with single-cell transcriptome readout. Nat Methods 14, 297-301.

Dixit, A., Parnas, O., Li, B., Chen, J., Fulco, C.P., Jerby-Arnon, L., Marjanovic, N.D., Dionne, D., Burks, T., Raychowdhury, R., et al. (2016). Perturb-Seq: Dissecting Molecular Circuits with Scalable Single-Cell RNA Profiling of Pooled Genetic Screens. Cell 167, 1853-1866 e1817.

Eisen, M.B., Spellman, P.T., Brown, P.O., and Botstein, D. (1998). Cluster analysis and display of genome-wide expression patterns. Proceedings of the National Academy of Sciences of the United States of America 95, 14863-14868.

Fernandopulle, M.S., Prestil, R., Grunseich, C., Wang, C., Gan, L., and Ward, M.E. (2018). Transcription Factor-Mediated Differentiation of Human iPSCs into Neurons. Curr Protoc Cell Biol 79, e51.

Ghosh, A.S., Wang, B., Pozniak, C.D., Chen, M., Watts, R.J., and Lewcock, J.W. (2011). DLK induces developmental neuronal degeneration via selective regulation of proapoptotic JNK activity. J Cell Biol 194, 751-764.

Gilbert, L.A., Horlbeck, M.A., Adamson, B., Villalta, J.E., Chen, Y., Whitehead, E.H., Guimaraes, C., Panning, B., Ploegh, H.L., Bassik, M.C., et al. (2014).

Genome-Scale CRISPR-Mediated Control of Gene Repression and Activation. Cell 159, 647-661.

Gilbert, L.A., Larson, M.H., Morsut, L., Liu, Z., Brar, G.A., Torres, S.E., Stern-Ginossar, N., Brandman, O., Whitehead, E.H., Doudna, J.A., et al. (2013). CRISPR-mediated modular RNA-guided regulation of transcription in eukaryotes. Cell 154, 442-451.

Groen, E.J.N., and Gillingwater, T.H. (2015). UBA1: At the Crossroads of Ubiquitin Homeostasis and Neurodegeneration. Trends in molecular medicine 21, 622-632.

Haapaniemi, E., Botla, S., Persson, J., Schmierer, B., and Taipale, J. (2018). CRISPR–Cas9 genome editing induces a p53-mediated DNA damage response. Nature medicine 24, 927-930.

Hart, T., Tong, A.H.Y., Chan, K., Van Leeuwen, J., Seetharaman, A., Aregger, M., Chandrashekhar, M., Hustedt, N., Seth, S., Noonan, A., et al. (2017). Evaluation and Design of Genome-Wide CRISPR/SpCas9 Knockout Screens. G3 (Bethesda) 7, 2719-2727.

Hester, M.E., Murtha, M.J., Song, S., Rao, M., Miranda, C.J., Meyer, K., Tian, J., Boulting, G., Shaffer, D.V., Zhu, M.X., et al. (2011). Rapid and Efficient Generation of Functional Motor Neurons From Human Pluripotent Stem Cells Using Gene Delivered Transcription Factor Codes. Molecular Therapy 19, 1905-1912.

Hill, A.J., McFaline-Figueroa, J.L., Starita, L.M., Gasperini, M.J., Matreyek, K.A., Packer, J., Jackson, D., Shendure, J., and Trapnell, C. (2018). On the design of CRISPR-based single-cell molecular screens. Nat Methods 15, 271-274.

Horlbeck, M.A., Gilbert, L.A., Villalta, J.E., Adamson, B., Pak, R.A., Chen, Y., Fields, A.P., Park, C.Y., Corn, J.E., Kampmann, M., et al. (2016). Compact and highly active next-generation libraries for CRISPR-mediated gene repression and activation. eLife 5.

Huntwork-Rodriguez, S., Wang, B., Watkins, T., Ghosh, A.S., Pozniak, C.D., Bustos, D., Newton, K., Kirkpatrick, D.S., and Lewcock, J.W. (2013). JNK-mediated phosphorylation of DLK suppresses its ubiquitination to promote neuronal apoptosis. J Cell Biol 202, 747-763.

Ihry, R.J., Worringer, K.A., Salick, M.R., Frias, E., Ho, D., Theriault, K., Kommineni, S., Chen, J., Sondey, M., Ye, C., et al. (2018). p53 inhibits CRISPR-Cas9 engineering in human pluripotent stem cells. Nature medicine 24, 939-946.

Iwamoto, M., Bjorklund, T., Lundberg, C., Kirik, D., and Wandless, T.J. (2010). A general chemical method to regulate protein stability in the mammalian central nervous system. Chemistry & biology 17, 981-988.

Jackson, A.L., Bartz, S.R., Schelter, J., Kobayashi, S.V., Burchard, J., Mao, M., Li, B., Cavet, G., and Linsley, P.S. (2003). Expression profiling reveals off-target gene regulation by RNAi. Nat Biotechnol 21, 635-637.

Javaherian, A., and Cline, H.T. (2005). Coordinated motor neuron axon growth and neuromuscular synaptogenesis are promoted by CPG15 in vivo. Neuron 45, 505-512.

Kaelin, W.G., Jr. (2012). Molecular biology. Use and abuse of RNAi to study mammalian gene function. Science 337, 421-422.

Kampmann, M. (2017). A CRISPR Approach to Neurodegenerative Diseases. Trends in molecular medicine 23, 483-485.

Kampmann, M. (2018). CRISPRi and CRISPRa Screens in Mammalian Cells for Precision Biology and Medicine. ACS Chem Biol 13, 406-416.

Kampmann, M., Bassik, M.C., and Weissman, J.S. (2013). Integrated platform for genome-wide screening and construction of high-density genetic interaction maps in mammalian cells. Proceedings of the National Academy of Sciences of the United States of America 110, E2317-2326.

Kampmann, M., Bassik, M.C., and Weissman, J.S. (2014). Functional genomics platform for pooled screening and generation of mammalian genetic interaction maps. Nature protocols 9, 1825-1847.

Koike-Yusa, H., Li, Y., Tan, E.P., Velasco-Herrera Mdel, C., and Yusa, K. (2014). Genome-wide recessive genetic screening in mammalian cells with a lentiviral CRISPR-guide RNA library. Nat Biotechnol 32, 267-273.

Langmead, B., Trapnell, C., Pop, M., and Salzberg, S.L. (2009). Ultrafast and memory-efficient alignment of short DNA sequences to the human genome. Genome biology 10, R25.

Larhammar, M., Huntwork-Rodriguez, S., Jiang, Z., Solanoy, H., Sengupta Ghosh, A., Wang, B., Kaminker, J.S., Huang, K., Eastham-Anderson, J., Siu, M., et al. (2017). Dual leucine zipper kinase-dependent PERK activation contributes to neuronal degeneration following insult. eLife 6.

Li, H., Kuwajima, T., Oakley, D., Nikulina, E., Hou, J., Yang, W.S., Lowry, E.R., Lamas, N.J., Amoroso, M.W., Croft, G.F., et al. (2016). Protein Prenylation Constitutes an Endogenous Brake on Axonal Growth. Cell Rep 16, 545-558.

Li, W., Xu, H., Xiao, T., Cong, L., Love, M.I., Zhang, F., Irizarry, R.A., Liu, J.S., Brown, M., and Liu, X.S. (2014). MAGeCK enables robust identification of essential genes from genome-scale CRISPR/Cas9 knockout screens. Genome biology 15, 554.

Liu, Y., Yu, C., Daley, T.P., Wang, F., Cao, W.S., Bhate, S., Lin, X., Still, C., Liu, H., Zhao, D., et al. (2018). CRISPR Activation Screens Systematically Identify Factors that Drive Neuronal Fate and Reprogramming. Cell Stem Cell 23, 758-771.

Luo, Y., Liu, C., Cerbini, T., San, H., Lin, Y., Chen, G., Rao, M.S., and Zou, J. (2014). Stable enhanced green fluorescent protein expression after differentiation and transplantation of reporter human induced pluripotent stem cells generated by AAVS1 transcription activator-like effector nucleases. Stem Cells Transl Med 3, 821-835.

Mandegar, M.A., Huebsch, N., Frolov, E.B., Shin, E., Truong, A., Olvera, M.P., Chan, A.H., Miyaoka, Y., Holmes, K., Spencer, C.I., et al. (2016). CRISPR Interference

Efficiently Induces Specific and Reversible Gene Silencing in Human iPSCs. Cell Stem Cell 18, 541-553.

McCarthy, D.J., Campbell, K.R., Lun, A.T., and Wills, Q.F. (2017). Scater: pre-processing, quality control, normalization and visualization of single-cell RNA-seq data in R. Bioinformatics 33, 1179-1186.

Miller, B.R., Press, C., Daniels, R.W., Sasaki, Y., Milbrandt, J., and DiAntonio, A. (2009). A dual leucine kinase-dependent axon self-destruction program promotes Wallerian degeneration. Nature neuroscience 12, 387-389.

Miyaoka, Y., Chan, A.H., Judge, L.M., Yoo, J., Huang, M., Nguyen, T.D., Lizarraga, P.P., So, P.L., and Conklin, B.R. (2014). Isolation of single-base genome-edited human iPS cells without antibiotic selection. Nat Methods 11, 291-293.

Mootha, V.K., Lindgren, C.M., Eriksson, K.F., Subramanian, A., Sihag, S., Lehar, J., Puigserver, P., Carlsson, E., Ridderstrale, M., Laurila, E., et al. (2003). PGC-1alpha-responsive genes involved in oxidative phosphorylation are coordinately downregulated in human diabetes. Nature genetics 34, 267-273.

Naeve, G.S., Ramakrishnan, M., Kramer, R., Hevroni, D., Citri, Y., and Theill, L.E. (1997). Neuritin: a gene induced by neural activity and neurotrophins that promotes neuritogenesis. Proceedings of the National Academy of Sciences of the United States of America 94, 2648-2653.

Nieland, T.J., Logan, D.J., Saulnier, J., Lam, D., Johnson, C., Root, D.E., Carpenter, A.E., and Sabatini, B.L. (2014). High content image analysis identifies novel

regulators of synaptogenesis in a high-throughput RNAi screen of primary neurons. PloS one 9, e91744.

Okita, K., Yamakawa, T., Matsumura, Y., Sato, Y., Amano, N., Watanabe, A., Goshima, N., and Yamanaka, S. (2013). An efficient nonviral method to generate integration-free human-induced pluripotent stem cells from cord blood and peripheral blood cells. Stem cells 31, 458-466.

Pozniak, C.D., Sengupta Ghosh, A., Gogineni, A., Hanson, J.E., Lee, S.H., Larson, J.L., Solanoy, H., Bustos, D., Li, H., Ngu, H., et al. (2013). Dual leucine zipper kinase is required for excitotoxicity-induced neuronal degeneration. J Exp Med 210, 2553-2567.

Robinson, M.D., McCarthy, D.J., and Smyth, G.K. (2010). edgeR: a Bioconductor package for differential expression analysis of digital gene expression data. Bioinformatics 26, 139-140.

Rosenbluh, J., Xu, H., Harrington, W., Gill, S., Wang, X., Vazquez, F., Root, D.E., Tsherniak, A., and Hahn, W.C. (2017). Complementary information derived from CRISPR Cas9 mediated gene deletion and suppression. Nat Commun 8, 15403.

Saldanha, A.J. (2004). Java Treeview--extensible visualization of microarray data. Bioinformatics 20, 3246-3248.

Schindelin, J., Arganda-Carreras, I., Frise, E., Kaynig, V., Longair, M., Pietzsch, T., Preibisch, S., Rueden, C., Saalfeld, S., Schmid, B., et al. (2012). Fiji: an open-source platform for biological-image analysis. Nat Methods 9, 676-682.

Schiroli, G., Conti, A., Ferrari, S., Della Volpe, L., Jacob, A., Albano, L., Beretta, S., Calabria, A., Vavassori, V., Gasparini, P., et al. (2019). Precise Gene Editing Preserves Hematopoietic Stem Cell Function following Transient p53-Mediated DNA Damage Response. Cell Stem Cell 24, 551-565 e558.

Sergushichev, A. (2016). An algorithm for fast preranked gene set enrichment analysis using cumulative statistic calculation. bioRxiv doi: https://doi.org/10.1101/060012.

Shalem, O., Sanjana, N.E., Hartenian, E., Shi, X., Scott, D.A., Mikkelsen, T.S., Heckl, D., Ebert, B.L., Root, D.E., Doench, J.G., et al. (2014). Genome-scale CRISPR-Cas9 knockout screening in human cells. Science 343, 84-87.

Sharma, K., Choi, S.Y., Zhang, Y., Nieland, T.J., Long, S., Li, M., and Huganir, R.L. (2013). High-throughput genetic screen for synaptogenic factors: identification of LRP6 as critical for excitatory synapse development. Cell Rep 5, 1330-1341.

Shi, Y., Lin, S., Staats, K.A., Li, Y., Chang, W.-H., Hung, S.-T., Hendricks, E., Linares, G.R., Wang, Y., Son, E.Y., et al. (2018). Haploinsufficiency leads to neurodegeneration in C9ORF72 ALS/FTD human induced motor neurons. Nature medicine 24, 313-325.

Subramanian, A., Tamayo, P., Mootha, V.K., Mukherjee, S., Ebert, B.L., Gillette, M.A., Paulovich, A., Pomeroy, S.L., Golub, T.R., Lander, E.S., et al. (2005). Gene set enrichment analysis: a knowledge-based approach for interpreting genome-wide expression profiles. Proceedings of the National Academy of Sciences of the United States of America 102, 15545-15550.

Tsunemoto, R., Lee, S., Szücs, A., Chubukov, P., Sokolova, I., Blanchard, J.W., Eade, K.T., Bruggemann, J., Wu, C., Torkamani, A., et al. (2018). Diverse reprogramming codes for neuronal identity. Nature 557, 375-380.

Valakh, V., Frey, E., Babetto, E., Walker, L.J., and DiAntonio, A. (2015). Cytoskeletal disruption activates the DLK/JNK pathway, which promotes axonal regeneration and mimics a preconditioning injury. Neurobiol Dis 77, 13-25.

Wang, C., Ward, M.E., Chen, R., Liu, K., Tracy, T.E., Chen, X., Xie, M., Sohn, P.D., Ludwig, C., Meyer-Franke, A., et al. (2017). Scalable Production of iPSC-Derived Human Neurons to Identify Tau-Lowering Compounds by High-Content Screening. Stem cell reports 9, 1221-1233.

Wang, T., Wei, J.J., Sabatini, D.M., and Lander, E.S. (2014). Genetic screens in human cells using the CRISPR-Cas9 system. Science 343, 80-84.

Watkins, T.A., Wang, B., Huntwork-Rodriguez, S., Yang, J., Jiang, Z., Eastham-Anderson, J., Modrusan, Z., Kaminker, J.S., Tessier-Lavigne, M., and Lewcock, J.W. (2013). DLK initiates a transcriptional program that couples apoptotic and regenerative responses to axonal injury. Proceedings of the National Academy of Sciences of the United States of America 110, 4039-4044.

Welsbie, D.S., Yang, Z., Ge, Y., Mitchell, K.L., Zhou, X., Martin, S.E., Berlinicke, C.A., Hackler, L., Jr., Fuller, J., Fu, J., et al. (2013). Functional genomic screening identifies dual leucine zipper kinase as a key mediator of retinal ganglion cell death. Proceedings of the National Academy of Sciences of the United States of America 110, 4045-4050.

Willsey, A.J., Morris, M.T., Wang, S., Willsey, H.R., Sun, N., Teerikorpi, N., Baum, T.B., Cagney, G., Bender, K.J., Desai, T.A., et al. (2018). The Psychiatric Cell Map Initiative: A Convergent Systems Biological Approach to Illuminating Key Molecular Pathways in Neuropsychiatric Disorders. Cell 174, 505-520.

Yang, N., Chanda, S., Marro, S., Ng, Y., Janas, J.A., Haag, D., Ang, C.E., Tang, Y., Flores, Q., Mall, M., et al. (2017). Generation of pure GABAergic neurons by transcription factor programming. Nature Methods 14, 621-628.

Yao, J.J., Zhao, Q.R., Liu, D.D., Chow, C.W., and Mei, Y.A. (2016). Neuritin Up-regulates Kv4.2 alpha-Subunit of Potassium Channel Expression and Affects Neuronal Excitability by Regulating the Calcium-Calcineurin-NFATc4 Signaling Pathway. The Journal of biological chemistry 291, 17369-17381.

Zhang, B., Kirov, S., and Snoddy, J. (2005). WebGestalt: an integrated system for exploring gene sets in various biological contexts. Nucleic acids research 33.

Zhang, Y., Pak, C., Han, Y., Ahlenius, H., Zhang, Z., Chanda, S., Marro, S., Patzke, C., Acuna, C., Covy, J., et al. (2013). Rapid Single-Step Induction of Functional Neurons from Human Pluripotent Stem Cells. Neuron 78, 785-798.

Zhou, Y., Zhu, S., Cai, C., Yuan, P., Li, C., Huang, Y., and Wei, W. (2014). High-throughput screening of a CRISPR/Cas9 library for functional genomics in human cells. Nature 509, 487-491.

CHAPTER THREE

Genome-wide CRISPRi/a screens in human neurons

link lysosomal failure to ferroptosis

INTRODUCTION

The human body comprises hundreds of different cell types. Even though their genomes are nearly identical, cell types are characterized by vastly different cell biologies, enabling them to fulfill diverse physiological functions. Transcriptomic profiling, fueled by recent advances in single-cell- and single-nucleus-RNA sequencing technologies, has revealed cell-type specific gene expression signatures (Gao et al., 2018; Han et al., 2020b; Lake et al., 2018; Muraro et al., 2016). In addition to gene expression, gene function can also be cell type-specific, as evidenced by the fact that mutations in broadly expressed or housekeeping genes can lead to strongly cell-type specific defects and disease states. Striking examples are familial mutations causing neurodegenerative diseases, which are often characterized by the selective vulnerability of specific neuronal subtypes, even if the mutated gene is expressed throughout the brain or even throughout the body. Cell-type specific gene function is also supported by our recent finding that knockdown of certain genes can have remarkably different impacts on cell survival and gene expression in different isogenic human cell types, including stem cells and neurons (Tian et al., 2019).

Therefore, understanding the function of human genes in different cell types is the next step toward elucidating tissue-specific cell biology and uncovering disease mechanisms. To this end, we recently developed a functional genomics platform, leveraging the strengths of CRISPR interference (CRISPRi) and iPSC technology, that enables large-scale, multimodal loss-of-function genetic screens in differentiated human cell types, as demonstrated in neurons (Tian et al., 2019). Here, we present a

complementary gain-of-function screening platform in human iPSC-derived neurons based on CRISPR-activation (CRISPRa), which can give complementary biological insights to CRISPRi screens (Gilbert et al., 2014).

We conduct the first genome-wide CRISPRi and CRISPRa screens in human neurons using different readouts to identify genes controlling neuronal survival and redox homeostasis, and CROP-seq screens to uncover transcriptional fingerprints of genes associated with neurodegenerative diseases.

Neurons, as one of the longest-living cell types in the human body, are challenged by various stresses in aging and disease. Due to their post-mitotic nature, neurons do not have the ability to 'self-renew' by cell division. Therefore, robust stress response mechanisms are required for neurons to maintain long-term health. One of the predominant stresses in aging and neurodegenerative diseases is oxidative stress (Barnham et al., 2004; Finkel and Holbrook, 2000), which is induced by excessive accumulation of reactive oxygen species (ROS) in the cell. ROS are highly reactive oxygen-derived molecules that are generated as by-products of normal oxygen metabolism. At low levels, ROS have physiological functions in cellular signaling and activate pro-survival pathways such as MAPK pathways (Kim et al., 2015).
Various antioxidant systems have evolved to control ROS levels and maintain redox homeostasis, including non-enzymatic antioxidants such as vitamin E, vitamin C and glutathione, and enzymatic antioxidants such as superoxide dismutase (SOD), glutathione peroxidases (GPX), peroxiredoxins (PRX) and catalase (Kim et al., 2015). There are also dedicated cellular pathways that sense and respond to ROS levels such

as the Keap1-Nrf2 pathway (Sies et al., 2017). An imbalance of ROS production and antioxidant defenses leads to excessive accumulation of ROS, which can cause oxidative damage to proteins, lipids and DNA and ultimately lead to cell death (Kim et al., 2015; Sies et al., 2017). In particular, peroxidation of lipids containing polyunsaturated fatty acids (PUFAs) can cause a non-apoptotic cell death termed ferroptosis, which is iron-dependent (Li et al., 2020).

The brain is highly susceptible to ROS and ferroptosis, due to its high levels of oxygen consumption, abundant redox-active metals such as iron and copper, limited antioxidants and high levels of PUFAs (Patel, 2016). A large body of evidence has indicated the implications of oxidative stress, iron accumulation and ferroptosis in many neurodegenerative diseases, including Alzheimer's disease (AD), Parkinson's disease (PD) and Amyotrophic Lateral Sclerosis (ALS) (Lin and Beal, 2006; Niedzielska et al., 2016; Rouault, 2013), yet a comprehensive understanding of how neurons regulate redox homeostasis and maintain survival under oxidative stress is lacking.

Here, we apply our functional genomics platforms to systematically identify genetic modifiers of ROS levels, lipid peroxidation, and neuronal survival under oxidative stress. These screens uncovered an unexpected role for prosaposin (PSAP), knockdown of which strongly induced ROS and lipid peroxidation levels in neurons and led to neuronal ferroptosis under oxidative stress. We elucidated the underlying mechanism: depletion of PSAP and resulting defects in glycosphingolipids (GSLs) degradation lead to the formation of lipofuscin in the lysosome, which is a hallmark of aged neurons,, driving the accumulation of iron and generation of ROS that oxidize

lipids. Intriguingly, the strong phenotypes of PSAP depletion are only presented in neurons, but not iPSCs or HEK293s. These results demonstrate the power of our platforms in uncovering novel cell-type specific human cell biology.

RESULTS

Genome-wide CRISPRi and CRISPRa screens reveal genes regulating survival of human neurons

We have previously established a CRISPRi platform that enables robust knockdown of endogenous genes and high-throughput loss-of-function genetic screens in human iPSC-derived neurons (Tian et al., 2019). Here, we further expand our toolbox by developing a CRISPRa system that allows us to robustly overexpress endogenous genes in cultured human neurons. We used a published inducible CRISPRa system, DHFR-dCas9-VPH, whose function has been validated in human iPSCs (Weltner et al., 2018). In this system, the CRISPRa machinery is tagged by a DHFR degron so that its activity can only be induced in the presence of trimethoprim (TMP) which stabilizes the DHFR degron and prevent the proteasomal degradation of the entire fused protein. Similarly to our CRISPRi platform, an expression cassette for CRISPRa, CAG promoter-driven DHFR-dCas9-VPH, was stably integrated into the CLYBL safe-harbor locus of an iPSC line (i3N-iPSC) with an inducible Neurogenin 2 (*Ngn2*) expression cassette in the AAVS1 safe-harbor locus (Fig.3.1A). These CRISPRa-iPSCs can be efficiently differentiated into homogenous glutamatergic neurons in a highly scalable manner upon doxycycline-induced Ngn2 expression. A monoclonal line of CRISPRa-iPSC was generated and a normal karyotype was confirmed (Fig.3.2A). In a functionality validation, our CRISPRa system robustly activated expression of an endogenous gene, *CXCR4*, in iPSC-derived neurons in a tightly inducible manner (Fig.3.1B).

We previously conducted a sub-genome scale CRISPRi screen to reveal genes regulating neuronal survival using an sgRNA library targeting 2,325 genes in the "druggable genome". Here, we greatly expanded the screen to target all protein-coding human genes in both loss-of- and gain-of-function screens by CRISPRi and CRISPRa respectively. To our knowledge, these are so far the first genome-wide CRISPR screens in human neurons . Using a similar paradigm as previously described (Tian et al., 2019) (shown in Fig. 3.1C), we transduced our CRISPRi and CRISPRa iPSCs via lentiviral delivery with the genome-wide hCRISPRi/a-v2 sgRNA libraries (Horlbeck et al., 2016). After selection and expansion, the transduced iPSCs (Day -3 iPSCs) were differentiated into neurons by doxycycline-induced Ngn2 expression. For the CRISPRa screen, TMP was added to Day 0 neurons to induce CRISPRa activity. For both screens, iPSCs prior to differentiation (Day -3) and Day10 neurons were collected and sgRNA frequencies in each sample were determined by next-generation sequencing of the sgRNA-encoding region. Based on the depletion or enrichment of sgRNAs targeting specific genes at Day10 compared to Day-3, we identified genes for which knockdown or overexpression inhibits or promotes neuronal survival. A phenotype score and a significance p value for each gene was calculated using our previously published pipeline, MAGeCK-iNC (Tian et al., 2019). We defined a 'gene score' as the product of phenotype score and $-\log_{10}$(p value) and called genes as hits based on gene score cutoff corresponding to an empirical false discovery rate (FDR) of 5% (Fig.3.1D).

Next, we focused on top enrichment and depletion hit genes in each screen. For CRISPRi, among the top 10 depletion hits were genes encoding superoxide dismutases, including *SOD1* and *SOD2*, which protect cells from oxidative stress, suggesting that redox homeostasis is pivotal for neuronal survival. Genes encoding subunits of vacuolar ATPase(V-ATPase) complex (e.g. *ATP6V1H*, *ATP6V1C1*, *ATP6AP1*, etc.,), which mediates acidification of endo-lysosomal vesicles through ATP hydrolysis coupled proton transport, were also among the top depletion hits, suggesting their indispensable role for neuronal survival, in line with the evidences that altered v-ATPase activity and lysosomal pH dysregulation could lead to aging and adult-onset neurodegenerative diseases, including Parkinson Disease and Alzheimer Disease (Colacurcio and Nixon, 2016). Interestingly, all 7 genes encoding components of the N6-methyltransferase writer complex including *METTL3*, *METTL14*, *KIAA1429* (also knowns as VIRMA), *WTAP*, *ZC3H13 RBM15 and CBLL1*, were among the top enrichment hits in CRISPRi screen, with 6 of them (except *CBLL1*) in the top 10 hits (Fig.3.1E). The N6-methyltransferase writer complex is responsible for the catalytic addition of N6-methyladenosine (m6A) modification to target RNAs, regulating their stability, processing and translation efficiency. M6A regulates various cellular processes and the result here indicates an interesting uncharacterized role of m6A in regulating neuronal survival. Moreover, Gene Ontology (GO) analysis revealed additional pathways that were enriched in the top 100 enrichment and depletion hits in the CRISPRi screen (Fig.3.1F). For example, genes involved in cholesterol biosynthesis were strongly enriched in depletion hits, suggesting an important role of cholesterol in

maintaining neuronal survival, consistent with our previous findings (Tian et al., 2019). We also identified other pathways, such as iron homeostasis, protein folding, mRNA processing and autophagy, were essential for neuronal survival. For CRISPRa, GO analysis revealed that overexpression of pro- and anti-apoptotic genes were enriched in top depletion and enrichment hits respectively, as expected, validating our approach.

We next compared survival-related hits we identified here for neurons with genes affecting survival of other cell types based on previous studies (Fig.3.2B). For CRISPRi, we compared essential genes for neurons (i.e. depletion hits) with those for either human pluripotent stem cells (integrated from 3 studies, Ihry et al., 2019, Mair et al., 2019 and Yilmaz et al., 2018) or cancer cells ('gold-standard' essential, Hart et al., 2017). This analysis revealed a shared core set of essential genes, as expected, and a large number of neuron-specific essential genes. Similarly, comparison between neurons and human pluripotent stem cells on genes for which knockdown promotes survival revealed minimal overlap,suggesting different roles genes may play in different cell types. For CRISPRa, we reanalyzed a published genome-wide survival screen in K562 cells (Horlbeck et al., 2016) using the same MAGeCK-iNC pipeline as in this study. Again, in both depletion and enrichment hits, the majority of them are neuron-specific. Taken together, these results highlighted the usefulness of our approach in uncovering neuron-specific gene function.

Next, we compared hits from our CRISPRi and CRISPRa screens (Fig.3.1E). Overall, there was little overlap between CRISPRi and CRISPRa hits, consistent with a previous study (Gilbert et al., 2014). The fact that CRISPRi and CRISPRa screens

uncover distinct sets of hit genes can be explained by several factors. First, a gene that is not expressed in neurons will not have a CRISPRi knockdown phenotype, but may have a CRISPRa overexpression phenotype. Indeed, genes expressed at low or undetectable levels were strongly depleted from CRISPRi hits (Fig.3.1G, left), whereas CRISPRa hits were not restricted by endogenous expression levels (Fig.3.1G, right). Second, CRISPRi hit genes encoded proteins that form a complex (such as the V-ATPase complex or the N6-methyltransferase writer complex), for which knockdown of a single component could abrogate the function of the entire complex and result in a phenotype, whereas overexpression of a single subunit by CRISPRa would generally be insufficient to induce an increased function of the complex. Last, knockdown of a single gene may not lead to a phenotype due to redundancy. Taken together, CRISPRi and CRISPRa screens can uncover complementary biological insights.

Nevertheless, there were a number of overlapping hit genes in the two screens (Fig.3.1E). Many of these genes showed opposing phenotypes on neuronal survival upon CRISPRa induction and CRISPRi repression. For example, the X-linked inhibitor of apoptosis protein (encoded by *XIAP*) affected survival negatively when repressed, but positively when activated. *XIAP* is a well-characterized gene that controls neuronal apoptosis by regulating caspase activity. Reduced XIAP levels or loss-of-function modifications of XIAP lead to axon degeneration and neuronal loss both *in vivo* and *in vitro* (Tsang et al., 2009; Unsain et al., 2013), whereas overexpression of *XIAP* is neuroprotective (Kügler et al., 2000; Xu et al., 1999). *GDPGP1* (encoding the GDP-D-Glucose Phosphorylase 1) showed similar phenotypes as *XIAP* in our screens.

A recent study showed that *GDPGP1* is a stress-responsive gene of which knockdown led to neuronal death while overexpression protected neurons against stress and neurodegeneration (Schulz et al., 2020). *MAP3K12* (encoding dual leucine zipper kinase DLK), another known factor regulating neuronal survival, when overpressed compromised neuronal survival, while its inhibition enhanced neuronal survival, consistent with our previous screen and other studies (Chen et al., 2008; Le Pichon et al., 2017; Tian et al., 2019; Welsbie et al., 2013).

For some genes, including several involved in protein homeostasis (e.g. *CUL3*, *FBXO2*, *COMMD1* and *HSPD1*), perturbations in both directions were detrimental to neuronal survival, suggesting their endogenous expression levels are narrowly balanced for optimal survival.

In summary, our genome-wide CRISPRi and CRISPRa screens uncovered complete sets of survival-related genes for human iPSC-derived neurons, which are largely different from other proliferating cell types including pluripotent stem cells or cancer cells. These results further demonstrated the potential of our platform to interrogate the biology of differentiated post-mitotic cell types.

Genome-wide CRISPRi/a screens elucidate pathways controlling neuronal response to oxidative stress

Given the unique vulnerability of neurons to redox imbalance-induced oxidative stress, which is often found in the brain of patients with NDDs, we sought to apply our functional genomics toolkit to systematically identify factors that are important for redox

homeostasis and oxidative stress response in human neurons. We performed screens based on two strategies.

First, we conducted genome-wide CRISPRi and CRISPRa screens to identify modifiers of neuronal survival under oxidative stress conditions (Fig.3.3A). Standard neuronal culture medium contains a combination of antioxidants, including vitamin E, vitamin E acetate, superoxide dismutase, catalase, and glutathione. To create an environment of chronic low-level oxidative stress, we cultured neurons in medium lacking the above antioxidants (–AO medium). We reasoned that compared to acute harsh treatments to induce ROS, such as adding H_2O_2 or rotenone, –AO medium provided a more physiologically relevant approximation of chronic oxidative stress .

We next compared modifiers of neuronal survival in this oxidative stress condition to the modifiers of survival in the standard,unstressed condition (Fig. 2B). Interestingly, in the comparison for CRISPRi hits, we identified that *GPX4* (encoding the selenoprotein Glutathione Peroxidase 4) and genes responsible for selenocysteine incorporation into proteins (including *PSTK*, *SEPHS2* and *SEPSECS*) were particularly essential for neurons to survive under oxidative stress (Fig.3.3B,C). GPX4 utilizes glutathione to reduce peroxidized lipids and thus prevents cells from ferroptosis, which is a non-apoptotic type of cell death caused by iron-dependent lipid peroxidation. This result suggested that neurons could be susceptible to ferroptosis under oxidative stress conditions. Hits for CRISPRa screens showed a high correlation between oxidative stress and unstressed conditions, suggesting no strong stress-specific phenotypes for overexpressed genes (Fig.3.4).

Second, we conducted genome-wide CRISPRi screens for modifiers of levels of ROS and peroxidized lipids in neurons. Specifically, we stained CRISPRi neurons transduced with genome-wide sgRNA libraries with fluorescent indicators of ROS and lipid peroxidation (CellRox and Liperfluo, respectively) and sorted them into high and low fluorescence populations by FACS (Fig.3.3B). The MAGeCK-iNC pipeline was used to identify hit genes knockdown of which led to an increase (‘high signal’’) or decrease (‘low signal’) in ROS or peroxidized lipids. From these screens, we identified both known and unexpected genetic modifiers of ROS and peroxidized lipid levels. We found that knockdown of components of the electron transport chain increased both ROS and lipid peroxidation levels (Fig.3.3D, 3.4B). This was expected, because ROS are mainly generated by proton leak from the electron transport chain, and knockdown subunits of electron transport chain complexes could increase proton leakage. Many autophagy-related genes were also common hits in the two screens (Fig.3.3D, 3.4B), suggesting an important role of autophagy in maintaining redox homeostasis in cells, as reported in previous studies (Filomeni et al., 2015; Guerrero-Gómez et al., 2019; Yan and Finkel, 2017).

Disruption of genes involved in the mTORC1 pathway, including components of the mTORC1 complex (*MTOR*, *RPTOR* and *MLST8* or its activator *RHEB* reduced ROS and/or lipid peroxidation levels in neurons (Fig.3.3E), consistent with previous observations that increasing mTORC1 signalling induced ROS production (Reho et al., 2019), whereas inhibiting mTORC1 reduced ROS (Nacarelli et al., 2014; Reho et al., 2019; Shin et al., 2011). Moreover, GO term enrichment analysis of lipid peroxidation

hits revealed a strong enrichment of peroxisomal genes, knockdown of which increased lipid peroxidation, consistent with the important roles of peroxisomes in redox regulation (Cipolla and Lodhi, 2017) and degradation of (poly-)unsaturated fatty acids (van Roermund et al., 1998).

FBXO7, a gene associated with Parkinson's disease, whose deficiency was found to cause complex I respiratory impairment and ROS production (Delgado-Camprubi et al., 2017), also increased ROS levels when knocked down in our screens. Knockdown of other previously characterized ROS regulators, including positive regulators such as *PARP1* (Hocsak et al., 2017), *SAT1* (Ou et al., 2016) and *NOX5* (Bánfi et al., 2001) and negative regulators such as *PTEN* (Bankoglu et al., 2016) and *FH* (encoding fumarate hydratase) (Bardella et al., 2012; Sudarshan et al., 2009) showed the expected effects on ROS and/or peroxidized lipid levels in our screens.

Interestingly, key regulators of ferroptosis were also hits in the lipid peroxidation screen. *ACSL4,* encoding Acyl-CoA Synthetase Long Chain Family Member 4, which enriches cellular membranes with long PUFAs is required for ferroptosis (Doll et al., 2017; Yuan et al., 2016). ACLS4 inhibition has been shown to prevent ferroptosis (Doll et al., 2017), consistent with reduction of peroxidized lipids upon knockdown in our screen (Fig.3.3E). By contrast, knockdown of *CD44*, whose splicing variant CD44v stabilizes the cystine/glutamate antiporter xCT at the plasma membrane and increases cysteine uptake for GSH synthesis, thereby inhibiting ferroptosis (Li et al., 2020), increased lipid peroxidation.

To further investigate hit genes from the genome-wide ROS and lipid peroxidation screens in high-throughput, we conducted 'batch characterization' screens. We generated an sgRNA library containing 2,190 sgRNAs targeting 730 hit genes from the genome-wide ROS and lipid peroxidation screens (3 sgRNAs per gene) plus 100 non-targeting sgRNAs. We screened these libraries for their effect on intracellular labile ferrous iron (Fe^{2+}) levels (by FeRhoNox-1 stain) and lysosomal status (by Lysotracker stain), given the important roles for iron in redox homeostasis and for lysosomes in metabolic signaling and autophagy (Fig.3.3A). These screens uncovered that several of our original ROS/lipid peroxidation hit genes also strongly affected iron and/or lysosome levels (Fig.3.3F). We found that knockdown of many lysosome/autophagy-related genes affected both lysosomal status and iron levels, reflecting the key role of lysosomes in iron homeostasis (Bogdan et al., 2016; Weber et al., 2020). Among these genes, we found *WDR45* and *WIPI2*, which are involved in autophagosome formation and lysosomal degradation and are also associated with Neurodegeneration with Brain Iron Accumulation (NBIA) in line with previous studies (Seibler et al., 2018; Wan et al., 2018). We also identified other known iron regulators for which knockdown increased iron levels, including *FBXL5,* a negative regulator of iron levels (Muto et al., 2017), the Fe/S cluster biogenesis genes *NFU1* and *NUBPL*, and *MCOLN1*, which encodes an endolysosomal iron release channel (Dong et al., 2008). Interestingly, depletion of genes involved in the electron transport chain increased free ferrous iron (Fig.3.3F), supporting the role of mitochondria as a major hub of cellular iron storage and utilization

in processes such as heme synthesis and iron-sulfur cluster biogenesis (Ward and Cloonan, 2019).

In summary, our screens for survival of oxidative stress and levels of ROS and peroxidized lipids uncovered many categories of known redox regulators, validating the sensitivity of our approach and supporting the notion that core mechanisms of redox regulation are conserved across different cell types. A substantial fraction of the hit genes were also modifiers of ferrous iron levels and/or lysosomal status (Fig.3.3G). Surprisingly, we identified that knockdown of *PSAP,* encoding the lysosomal protein prosaposin which facilitates glycosphingolipids (GSLs) degradation, altered lysosomal status and strongly induced ROS, lipid peroxidation and iron levels when depleted (Figure E-G). Given the unexpected link between the known functions of PSAP and its screen phenotypes, we further investigated the underlying mechanisms of *PSAP* in redox regulation in the later sections of this paper.

Transcriptomic signatures of perturbations of disease-associated genes in human neurons

Over the past decade, genome-wide association studies (GWASs) have uncovered hundreds of genes that are associated with human neurodegenerative diseases (NDD), including Alzheimer's disease, Parkinson's disease and others (Chang et al., 2017; Shen and Jia, 2016). However, functional characterizations of these risk genes are largely lacking (Gallagher and Chen-Plotkin, 2018). Our CRISPRi and CRISPRa platforms provide a high-throughput approach to systematically interrogate

gene function in human neurons. Beyond one-dimensional phenotypes such as survival or fluorescent reporter levels, CRISPR perturbation can be coupled to single-cell RNA sequencing, using CROP-seq or Perturb-Seq strategies, to provide rich transcriptomic phenotypes.

The hit genes from our unbiased genome-wide CRISPRi and CRISPRa screens included hundreds of genes associated with NDDs (based on DisGeNet annotation and literature research). To better characterize these NDD risk genes, we performed CROP-seq experiments, targeting 184 genes for CRISPRi and 100 genes for CRISPRa with 2 sgRNAs per gene (see Method for details). Robust on-target gene knockdown and overexpression were detected for CRISPRi and CRISPRa, respectively (Fig.3.5B-D). Within the population of cells expressing sgRNAs for a specific target gene, the levels of target knockdown or overexpression were heterogeneous in some cases (Fig.3.5B,C). This could be due to different efficiencies of the two sgRNAs targeting that gene, misassignment of sgRNA identities for some cells or stochastic silencing of the CRISPR machinery in some cells. To select cells in which intended genes were effectively targeted, we employed an unsupervised classification method based on outlier detection using a local outlier factor. The classifier was first trained by the gene expression profiles of cells containing non-targeting sgRNAs. Then the classifier will detect for each group of cells containing sgRNAs for a specific target gene, whether a cell was an ‘outlier’ compared to training samples, i.e. non-targeting control cells. If the sgRNA in a cell was not active, the expression profile of that cell will be similar to cells with non-targeting control sgRNAs, and it will therefore be classified as a

non-outlier(Fig.3.5B, see Method for details). This classification method was particularly useful for CRISPRi when the basal expression level of the target gene was too low to be detected by single-cell RNA-seq thus did not allow selecting cells based on knockdown level of target gene. Using this classification method, we retained cells with functional perturbations for downstream analysis.

To characterize how gene knockdown or overexpression altered transcriptomes of neurons, we performed differential gene expression analysis between cells containing perturbations and cells containing non-targeting control sgRNAs. From this analysis, we identified differentially expressed genes (DEGs) for each perturbation. To identify convergent transcriptomic responses across different perturbations of disease-associated genes, we determined pairwise DEG similarities among all perturbations using a method relying on weighted sum of overlap in top-ranking DEGs(see Methods). This analysis revealed clusters of genes that shared common DEG signatures (Fig.3.5E). As expected, knockdown of functionally related genes had similar transcriptomic consequences. For example, knockdown mitochondria-related genes, including *COX10, NDUFS8, NDUFV1, MRPL10 and SOD2,* resulted in similar DEGs, as did knockdown of the anti-apoptotic genes *BNIP1* and *XIAP*.. However, we also identified unexpected gene clusters. For example, knockdown of *VPS54*, *PAXIP1* and *PON2* caused highly correlated transcriptomic changes (Fig.3.6). , *VPS54* and *PON2* have been implicated in Amyotrophic Lateral Sclerosis (ALS) whereas *PAXIP1* is associated with AD (Chen et al., 2015; Schmitt-John et al., 2005; Slowik et al., 2006). Shared transcriptomic changes included: (i) upregulation of *EBF3*, an apoptosis inducer

that is also upregulated in the hippocampus of AD model mice (Gu et al., 2018; Zhao et al., 2006), (ii) downregulation of components of neurofilaments, including *NEFL*, *NEFM* and *NEFH*, which are biomarkers for ALS and AD progression. Importantly, *NEFL*, *NEFM* and *NEFH* mRNA levels are decreased in patients with NDDs, including ALS, AD and PD (Julien and Mushynski, 1998; Mathys et al., 2019; Rosengren et al., 1996) and (iii) downregulation of other genes important for neuronal function, including *PCDH11X* and *PCDH11Y,* encoding protocadherin proteins, and *SYT2,* encoding synaptotagmin 2.

To identify genes that were co-regulated under different genetic perturbations, we performed weighted gene co-expression network analysis (WGCNA). This analysis identified 10 modules for CRISPRi and 8 modules for CRISPRa that were co-regulated across different perturbations (Fig.3.5F). These modules contained genes enriched in various pathways (Fig.3.5G). Interestingly, we found a cluster of genes including *INSR*, *ATP5F1C*, *SOX5*, *GSX2* and *GBX2* (Fig.3.5E, right) overexpression of which downregulated a gene module related to neurogenesis (M1) and upregulated a gene module related to the cell cycle (M5) (Fig.3.5F, bottom), suggesting that overexpression of these genes interfered with neuronal differentiation thus kept cells in a proliferating state. This result was expected for *SOX5*, *GSX2* and *GBX2*, which are transcription factors maintaining neural progenitor cell fate and/or their self-renewal (Luu et al., 2011; Martinez-Morales et al., 2010; Méndez-Gómez and Vicario-Abejón, 2012), but unexpected for *INSR* (encoding the insulin receptor) and *ATP5F1C* (encoding a subunit of mitochondrial ATPsynthase), suggesting these genes might have uncharacterized functions in neuronal fate regulation, which require further investigation.

The CROP-seq data also generated hypotheses for disease mechanisms. For example, *NQO1*, encoding the NAD(P)H:Quinone Oxidoreductase 1, is thought to be a cytoprotective factor through its antioxidant functions (Ross and Siegel, 2017). Elevated levels and activity of NQO1 has been found in the brains of patients with different NDDs, including AD and PD (Bian et al., 2008; van Muiswinkel et al., 2004; Raina et al., 1999; SantaCruz et al., 2004; Wang et al., 2000), as well as in patient iPSC-derived neurons (Imaizumi et al., 2012). The upregulation of NQO1 was proposed to be a neuroprotective mechanism against oxidative stress in NDDs. Paradoxically, however, *NQO1* overexpression showed a strong negative impact on neuronal survival in our pooled CRISPRa screen (Fig.3.1E). In the CROP-seq data, we observed distinct gene expression profiles for cells overexpressing *NQO1* compared to control (Fig.3.5C, Fig.3.7A). Surprisingly, *NQO1* overexpression strongly induced the NRF2 pathway (Fig.3.7B,C). The transcription factor NRF2 induces the expression of many antioxidant genes, including *NQO1*, in response to oxidative stress (Ma, 2013). Intriguingly, the NRF2 pathway is also induced in PD, both in patient brains and in patient iPSC-derived neurons (Imaizumi et al., 2012; Ramsey et al., 2007). Based on these findings, we can formulate several testable hypotheses. For example, upregulation of NQO1 in the context of NDDs could be neurotoxic instead of neuroprotective, by inducing or mimicking an oxidative stress condition through unknown mechanisms, in turn activating the NRF2 pathway, which however is insufficient to cope with the stress. Based on this hypothesis, the elevation of NQO1 levels in patients would actually contribute to disease, rather rather than being an effective defense mechanism. Alternatively, the

toxicity of NQO1 overexpression is caused by other mechanisms, such as downregulation of genes involved in axon development or cholesterol metabolism, which we observed in the CROP-seq data (Fig.3.7B,C). In this scenario, the NRF2 pathway would be activated through an unknown feedback mechanism by which cells attempt to match the levels of different antioxidant strategies to that of NQO1 in NQO1-overexpressing cells (Fig.3.7B,C).

Taken together, our CROP-seq results provide a rich resource for investigating consequences of perturbations of NDD-associated genes in human neurons and for generating testable hypotheses for the NDD mechanisms and potential therapeutic strategies.

Depletion of prosaposin increases ROS and lipid peroxidation levels in neurons and causes neuronal ferroptosis under oxidative stress

As described above, we surprisingly identified prosaposin (encoded by *PSAP*) as one of the strongest hits in our FACS screens for redox modifiers, knockdown of which increased ROS and lipid peroxidation levels (Fig.3.8A). Prosaposin is a pro-protein that is proteolytically processed by cathepsin D (encoded by *CTSD*) in the lysosome to generate four cleavage products: saposins A, B, C, and D (Hiraiwa et al., 1997). These four saposins, along with the lysosomal protein GM2A (GM2 Ganglioside Activator), function as activators for glycosphingolipid (GSL) degradation by lysosomal hydrolases (Sandhoff and Harzer, 2013). Intriguingly, both *CTSD* and *GM2A* were also hits in at

least one of the redox screens, showing similar knockdown phenotypes as *PSAP*, which suggested an important and unexpected role of GSL degradation in redox homeostasis.

To validate our screen results using an independent approach, we generated a clonal *PSAP* knockout (KO) iPSC line by CRISPR/Cas9. Western blot and immunostaining confirmed a complete depletion of PSAP in the KO line (Fig.3.8C & D). Next, we measured ROS and lipid peroxidation levels in WT and *PSAP* KO neurons. We included C11-BODIPY, another indicator for oxidized lipid, as additional validation for lipid peroxidation levels. Indeed, we observed a substantial increase in ROS and oxidized lipid levels in *PSAP* KO neurons, confirming our screen results (Fig.3.8E). Moreover, ROS induction in PSAP KO neurons can be rescued by the overexpression of *PSAP* cDNA, confirming that phenotypes were not driven by off-target genome editing. Interestingly, *PSAP* KO or knockdown in other cell types, including iPSCs and HEK293s, did not increase ROS levels (Fig.3.8F), suggesting a neuron-specific role of PSAP in redox regulation.

Next, we asked if increased ROS in *PSAP* KO neurons affect survival. Interestingly, we did not observe a survival defect of *PSAP* KO neurons over two weeks of culture in standard neuronal medium (+AO). Strikingly, however, when we cultured these neurons in the medium lacking antioxidants (–AO), *PSAP* KO caused a dramatic decrease in survival on Day 8, and complete death of all neurons by Day 14 (Fig.3.8G).

To further investigate the underlying mechanism of cell death, we treated WT and *PSAP* KO neurons with compounds that inhibit different cell death pathways. Intriguingly, the viability of *PSAP* KO neurons under the -AO condition was not rescued

by Z-VAD-FMK, a pan-caspase inhibitor that blocks apoptosis, but was fully rescued by ferroptosis inhibitors, including the iron chelator deferoxamine (DFO) and the lipid peroxidation inhibitor ferrostatin-1 (Fig.3.8H,I).

In summary, we validated the unexpected strong hit gene from our unbiased screens, *PSAP,* as a strong redox modifier in human neurons. Depletion of *PSAP* increases ROS levels and leads to increased lipid peroxidation, resulting in neuronal ferroptosis under mild oxidative stress.

Depletion of *PSAP* leads to GSL accumulation and lipofuscin formation in lysosomes, which impairs lysosomal functions and causes iron accumulation, resulting in increased ROS and lipid peroxidation levels

Given the surprising connection between *PSAP* and ferroptosis, we further investigated the underlying mechanism. We first asked if depletion of *PSAP* blocked GSL degradation, given the canonical function of saposins. To answer this question, we performed untargeted lipidomics on WT and *PSAP* KO neurons. Indeed, almost all GSL species accumulated significantly in *PSAP* KO neurons compared to WT neurons (FDR < 0.01, Fig.3.9 A,B). Ether lipids, which are peroxisome-derived glycerophospholipids, were also enriched in *PSAP* KO neurons. Whether ether lipid accumulation was due to a protective or maladaptive mechanism remains to be investigated. Interestingly, the accumulation of ether lipids was also characterized as a feature of hypoxia in a recent study (Jain et al., 2020).

We also confirmed the accumulation of a specific GSL species, GM1 ganglioside, by immunostaining in *PSAP* KO neurons (Fig.3.9C). Interestingly, we did not observe GM1 accumulation in *PSAP* KO iPSCs (Fig.3.9D), suggesting a cell-type specific role of *PSAP*. Strikingly, we observed dramatically enlarged lysosomes (by LAMP2 staining) in *PSAP* KO neurons (Fig.3.9C), which were also reflected in an increased lysotracker signal by flow cytometry (Fig.3.9E), as expected based on our screen results (Fig.3.3F). Again, this phenotype was neuron-specific, as *PSAP* depletion did not cause enlarged lysosomes in other cell types , iPSCs or HEK293s (Fig.3.9F).

We observed colocalization of accumulated GM1 and LAMP2-positive lysosomes by conventional confocal microscopy and by super-resolution microscopy (Fig.3.9C & 6G), consistent with the notion that lysosome is the main compartment for GSL degradation.

To further characterize the enlarged, LAMP2-positive lysosome-like structures accumulating in *PSAP* KO neurons, we performed electron microscopy (EM). Remarkably, we observed a large number of electron-dense granules that resembled the structure of lipofuscin (also known as age pigment), an aging-associated insoluble aggregate of oxidized lipids and proteins and metals in lysosomes of postmitotic cells, such as neurons, which forms through unknown mechanisms (Terman and Brunk, 1998). One feature of lipofuscin is its autofluorescence when excited by ultraviolet (UV) light (Mochizuki et al., 1995). Indeed, we detected strong autofluorescence in the FITC channel (525/20 nm) in *PSAP* KO neurons when excited by UV light (405 nm) (Fig.3.9I), confirming the formation of lipofuscin in *PSAP* KO neurons. lipofuscin is known to

accumulate iron from lysosomal degradation of iron-rich proteins or organelles (e.g. mitochondria), and accumulated iron in lipofuscin can generate ROS through the Fenton reaction, which is promoted by the low pH of the lysosome (Terman and Brunk, 2004). Indeed, we observed an substantial increase of iron levels in *PSAP* KO neurons using a panel of different iron indicators (Fig.3.9J, K, 3.10A,B), This result was consistent with our finding of PSAP as a top hit in our iron level screen (Fig.3.3F). The accumulated iron in *PSAP* KO neurons was colocalized with lysosomes and was partially rescued by the iron chelator DFO (Fig.3.9K, 3.10A&B). As a consequence of iron accumulation, dramatically increased lipid peroxidation was detected in lysosomes of *PSAP* KO neurons (Fig.3.9L), consistent with the strong lipid peroxidation-inducing phenotype of *PSAP* knockdown in our screen (Fig.3.3E).

The formation of lipofuscin also disrupted other lysosomal functions in *PSAP* KO neurons. We observed a massive accumulation of autophagosomes in *PSAP* KO neurons as indicated by the increased ratio of PE-conjugated form of LC3B to its unconjugated form (LC3B-II / LC3B-I) by western blot (Fig.3.9M,N), and increased LC3B puncta by immunostaining (Fig.3.9O) . Treatment with Bafilomycin A1 (BafA1), an inhibitor for degradation of autophagosomes by lysosomes, increased the LC3B-II / LC3B-I ratio in WT, but not *PSAP* KO neurons (Fig.3.9M), suggesting a blockade of autophagic flux in *PSAP* KO neurons.

Moreover, we performed RNA-seq on WT and *PSAP* KO neurons. Interestingly, a number of genes involved in cholesterol biosynthesis were upregulated in *PSAP* KO neurons (Fig.3.10C and 3.10D). Consistent with the induction of this pathway, we found

increased cholesterol levels in lysosomes of *PSAP* KO neurons, as measured by Filipin staining (Fig.3.10E and 3.10F). This finding mirrored the results of previous studies showing that *PSAP* is a strong genetic modifier for cholesterol levels (Bartz et al., 2009) and accumulated GSLs can lead to accumulation of cholesterol in lysosomes by inhibiting cholesterol efflux (Glaros et al., 2005; Harbison et al., 1976; Puri et al., 2003).

In summary, we elucidated that *PSAP* depletion blocks GSL degradation in lysosomes, leading to the formation of lipofuscin, which in turn accumulates iron and generates ROS that oxidized lipids. The accumulation of oxidized lipids leads to neuronal ferroptosis in the absence of antioxidants (Fig.3.11).

DISCUSSION

In this study, we developed a CRISPRa platform in human iPSC-derived neurons, complementing our previously established CRISPRi platform, to enable robust gene perturbation and large-scale, multimodal genetic screens in human neurons.

We demonstrated the power of our screening platforms in multiple large-scale screens in human iPSC-derived neurons, including genome-wide CRISPRi and CRISPRa survival screens under unstressed and oxidative stress conditions, genome-wide CRISPRi screens based on ROS and peroxidized lipid levels, secondary CRISPRi screens based on iron levels and lysosomal status, and CROP-seq screens on NDDs-associated genes.

Compared to other published CRISPR screens focusing on ROS toxicity in human cells (Dubreuil et al., 2020; Reczek et al., 2017), our screens are unique in the following aspects. First, we used post-mitotic neurons instead of cancer cell lines. Second, we induced milder oxidative stress in cells by prolonged culture of cells in an antioxidant-free medium, compared to severe oxidative stress induced by paraquat or H_2O_2 in other studies. Thirdly, we screened not only based on cell survival, but also on direct ROS and lipid peroxidation levels, while other studies focused on survival only. Given these major differences, it is not surprising that the majority of our hits were not identified in previous screens.

Numerous novel biological insights have emerged from our rich datasets. In particular, we identified the first comprehensive inventories of genes that, when depleted or activated, modulate survival of human neurons under normal or oxidative

stress conditions. Intriguingly, many of these genes only affect survival in neurons, but not stem cells or cancer cells, supporting the notion that neurons have cell-type specific vulnerabilities, which may explain why defects in some generally expressed genes specifically cause neurological diseases. .

Our screens also identified that GPX4 and genes related to GPX4 synthesis are indispensable for neurons to survive oxidative stress. Given the major role of GPX4 in reducing lipid peroxidation and suppressing ferroptosis, this result suggests that lipid peroxidation-induced ferroptosis, rather than other forms of cell death, may be the main cause of neuronal loss under oxidative stress conditions that are commonly found in the brains of patients with NDDs. This is supported by numerous studies reporting high levels of iron and lipid peroxidation in NDD patient brains (Han et al., 2020a; Ndayisaba et al., 2019), and by the finding that ferroptosis inhibitors such as iron chelators and the lipid-peroxidation inhibitor Ferrostatin-1 are neuroprotective in animal and cellular models of NDDs, including AD, PD and HD (Han et al., 2020a).

Among all tissues in the human body, the brain is one of the richest in lipid content and lipid diversity. Lipids are not only an essential structural component of membranes, but also important signaling molecules in the brain (Bazan, 2005). Therefore, maintaining lipid homeostasis is of vital importance for brain cells, especially neurons with long neurites and dynamic synaptic vesicles release and recycling. Although abnormal lipid metabolism has been observed in NDDs (Hallett et al., 2019; Yadav and Tiwari, 2014), its role as a pathogenic mechanism has not been investigated as extensively as ‘protein-centric’ mechanisms, in particular protein aggregation. Our

results indicate that disruption of lipid metabolism, in particular glycosphingolipid degradation in the lysosome by depletion of prosaposin (PSAP), drives the formation of lipofuscin in neurons, which leads to iron accumulation and strongly induces ROS production, oxidizing lipids and leading to neuronal ferroptosis under oxidative stress.

While lipofuscin has traditionally been considered a byproduct of aging and as a consequence of defective cellular homeostasis, our result argues that lipofuscin can have a direct pathogenic role in inducing neuronal ferroptosis. Given the presence of lipofuscin in many neurodegenerative diseases, including neuronal ceroid lipofuscinosis (NCL) (Grubman et al., 2014) and frontotemporal dementia (FTD) (Ward et al., 2017), this result suggests that inhibiting ferroptosis or lipofuscin formation may serve as new therapeutic strategies.

Furthermore, studying biological functions and biophysical properties of lipofuscin rely on a robust system to generate it. The fact that lipofuscin is normally only formed in aged post-mitotic cells makes it very difficult to model them. Our PSAP depletion neurons provide a reliable genetic system to model and study the biology of lipofuscin in live cells.

Our result highlights the importance of balanced levels of GSLs for neuronal health. This is supported by a recent study which shows that the accumulation of certain GSLs, especially simple gangliosides caused by inhibition of lysosome membrane recycling contributes to neurodegeneration both in cultured neurons and in animal models (Boutry et al., 2018)..

Many important questions around neuronal ferroptosis remain to be investigated. For example, since neurons have very long neurites, how do neurons sense and respond to a local lipid peroxidation event on cell membrane? Is GPX4 or other enzymes recruited to sites of lipid peroxidation, or are peroxidized lipids internalized and delivered to GPX4 or other enzymes for detoxification? What are the sensors and mediators in these processes? How do peroxidized lipids cause neuronal death? Is it a passive physical process or a regulated biological program? If the latter is true, what are the players mediating cell death downstream of lipid peroxidation? Many of these questions can be readily investigated using our functional genomics platform.

There are several areas for future development. First, a robust inducible CRISPRi system that allows temporal control of gene knockdown in mature neurons will help avoiding false-positive screening phenotypes due to interference with the differentiation process. For example, the inducible CRISPRi system will help to determine whether the strong enrichment phenotypes of genes in the N6-methyltransferase writer complex (Fig.3.1E) is due to increased neuronal survival or defects in neuronal differentiation, since m6A can regulate neuronal differentiation (Edens et al., 2019; Li et al., 2018). Second, a high-throughput imaging-based application of our platform in an arrayed format will allow screens for complex neuronal phenotypes, including electrophysiological signals (by voltage imaging or calcium imaging), neurite outgrowth, synaptic vesicle dynamics, axonal transport and so on. This can also be coupled with transcriptomic profiling, thus allowing association of gene expression with imaging phenotypes for a given genetic perturbation. Lastly, by

combining our platform with the recently developed prime editing technology (Anzalone et al., 2019), we will be able to directly assess the effect of disease-associated mutations on given cellular phenotypes in a scalable, massively parallel format.

We anticipate that our iPSC-based functional genomics platforms can be broadly applied to a variety of human differentiated cell types. Parallel genetic screens across the full gamut of isogenic human cell types will uncover context-specific roles of human genes, leading to a deeper mechanistic understanding of how they control human biology and disease.

FIGURES

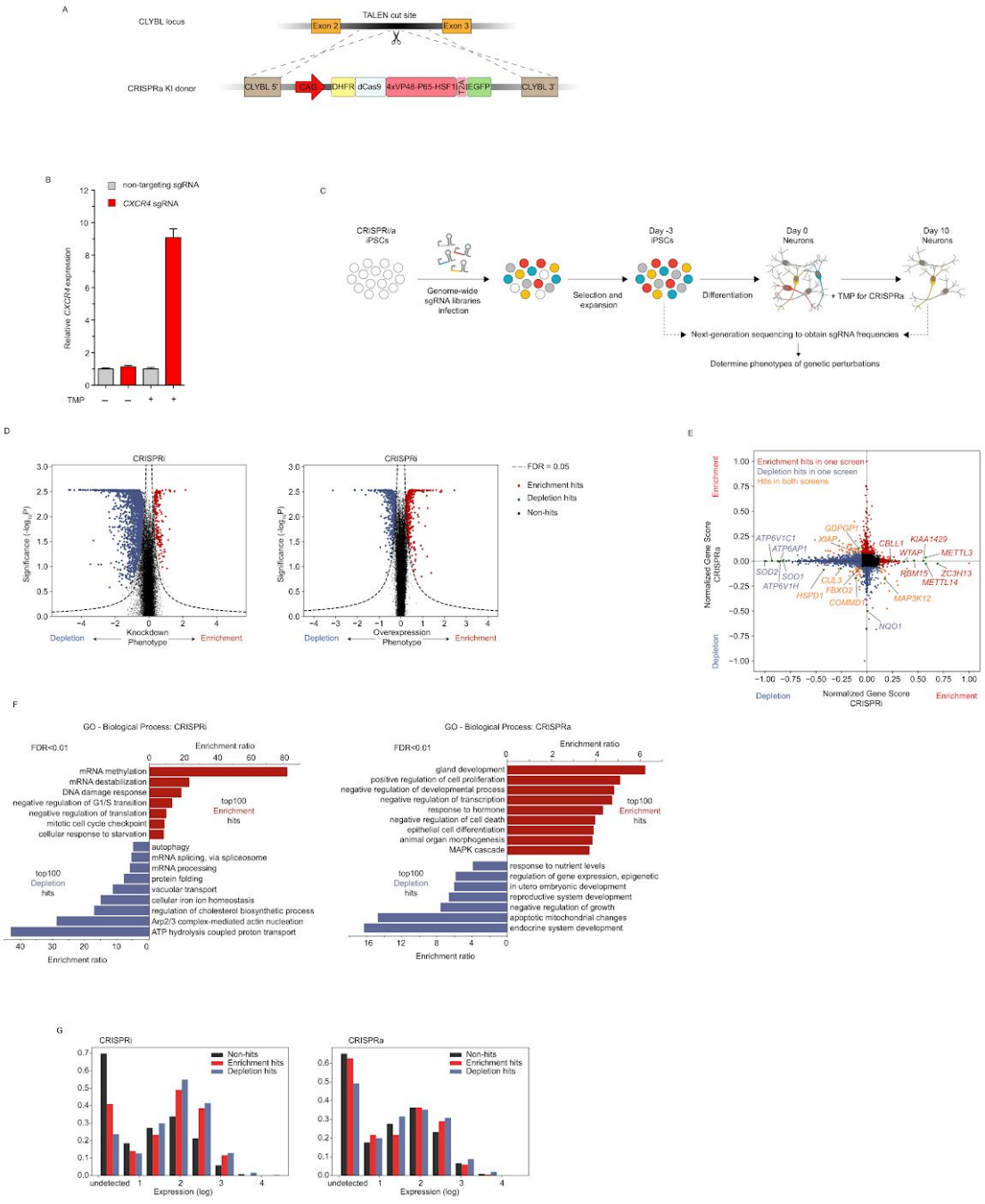

Fig.3.1. Genome-wide CRISPRi & CRISPRa screens in human iPSC-derived neurons identify regulators of neuronal survival

(A) Strategy for generating the CRISPRa iPSC line: an inducible CRISPRa construct, CAG promoter-driven DHFR-dCas9-VPH, was stably integrated into the CLYBL safe

harbor locus through TALEN-mediated knock-in. dCas9, catalytically dead cas9. VPH, activator domains containing 4X repeats of VP48, P65 and HSF1.

(B) Functional validation of CRISPRa activity. qPCR quantification of the relative fold change of *CXCR4* mRNA levels in CRISPRa-neurons expressing a *CXCR4* sgRNA as compared to a non-targeting control sgRNA in the presence or absence of trimethoprim (TMP), which stabilizes the DHFR degron (mean ±sd, n = 3). *CXCR4* levels are normalized to the housekeeping gene *ACTB*.

(C) Schematic for neuronal survival screens. CRISPRi/a iPSCs were transduced with genome-wide sgRNA libraries, containing ~100,000 sgRNAs targeting ~19,000 protein-coding genes and ~1,800 non-targeting control sgRNAs. TMP was added to CRISPRa neurons from Day 0 to induce CRISPRa activity. Frequencies of cells expressing a given sgRNA were determined by next-generation sequencing for Day 10 neurons and Day -3 iPSCs.

(D) Volcano plots summarizing knockdown or overexpression phenotypes and statistical significance (Mann-Whitney U test) for genes targeted in the CRISPRi (left) and CRISPRa (right) screens. Dashed lines: gene score cutoff for hit genes (FDR = 0.05, see Methods)

(E) Comparing hits from CRISPRi and CRISPRa screens. Genes that are enrichment and depletion hits in either screen are shown in red and blue, respectively. Genes that are hits in both screens are shown in orange. Genes discussed in this paper are highlighted in green.

(F) Gene Ontology (GO) term enrichment analysis for the top 100 enrichment and depletion hits in CRISPRi (left) and CRISPRa (right) survival screens. Significantly enriched Biological Process terms (FDR<0.01) are shown.

(G) Expression levels of hit genes (enrichment or depletion) and non-hit genes from CRISPRi (left) or CRISPRa (right) screens.

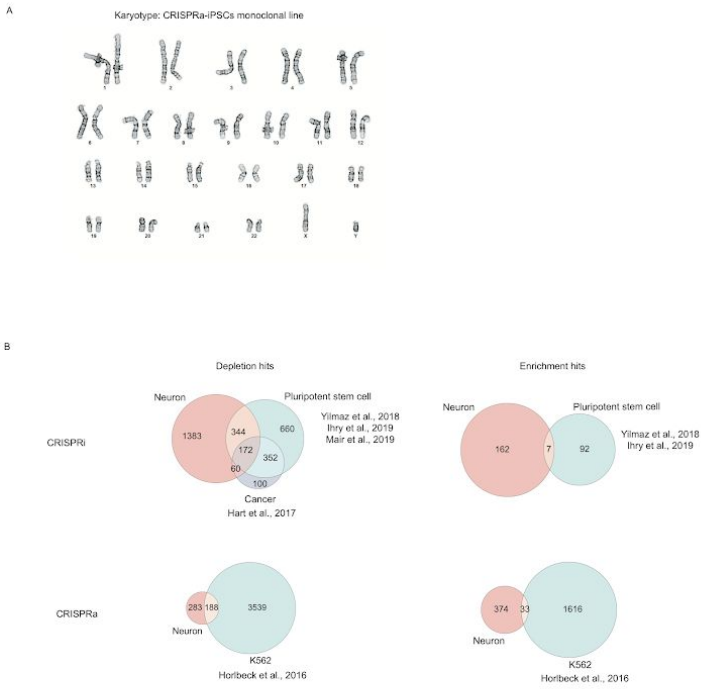

Fig.3.2. Karyotyping of the monoclonal CRISPRa-iPSC line and comparison of CRISPRi and CRISPRaa screen results for neuronal survival with other published survival screens for different cell types

(A) A normal karyotype was confirmed for the monoclonal CRISPRa-iPSC line.

(B) Venn diagrams comparing CRISPRi and CRISPRa screen results for neuronal survival from this paper with other published survival screens for different human cell types. For CRISPRi, depletion hits for the survival of neurons were compared with those for cancer cells ('gold-standard' essential genes, Hart et al., 2017) and pluripotent stem cells (integrated from Ihry et al., 2019; Mair et al., 2019 and Yilmaz et al., 2018); genes that were identified as essential in more than one studies were retained for comparison).Enrichment hits for the survival of neurons were compared with those for human pluripotent stem cells (integrated from Ihry et al., 2019; Yilmaz et al., 2018. Genes that were identified as essential in both studies were retained for comparison). For CRISPRa, hits were compared with a published survival screen in K562 cells (Horlbeck et al., 2016) reanalyzed using our MAGeCK-iNC pipeline.

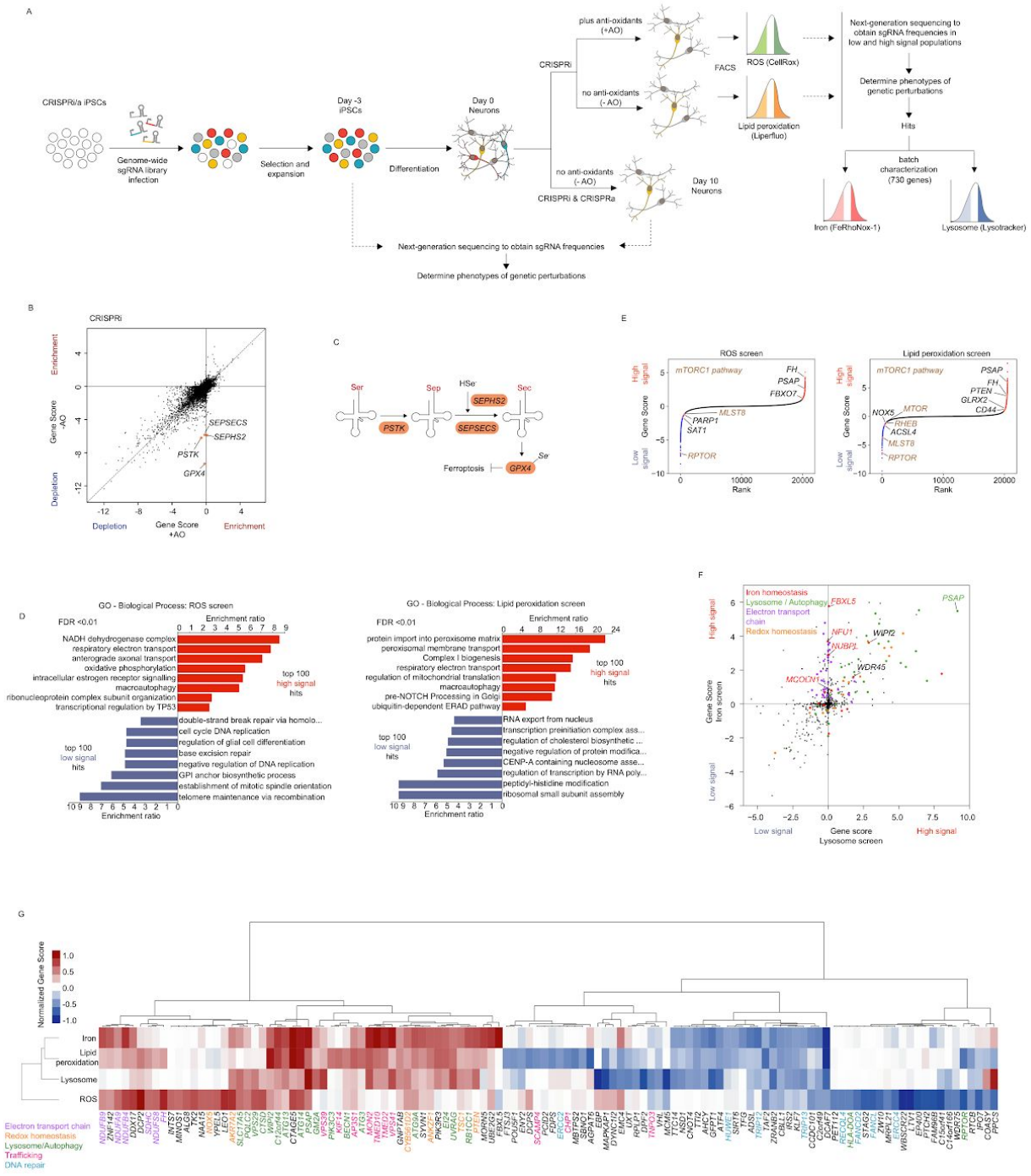

Fig.3.3. Genome-wide CRISPRi & a screens in human iPSC-derived neurons identify regulators of oxidative stress response and redox homeostasis

(A) Screening strategies. First, survival-based screens were conducted to identify modifiers of neuronal survival under mild oxidative stress induced by anti-oxidant removal from the neuronal medium (-AO). Second, FACS-based screens were

conducted for modifiers of ROS and lipid peroxidation levels. Last, batch characterization screens were conducted to further characterize hit genes.

(B) Comparison of gene scores in +AO and -AO conditions for CRISPRi survival screens.

(C) Pathway for selenocysteine incorporation into GPX4. Hit genes are highlighted in orange.

(D) GO term enrichment analysis for the top 100 high-signal and low-signal hits in the ROS screen (left) and the lipid peroxidation screen (right). Significantly enriched Biological Process terms (FDR<0.01) are shown.

(E) Ranked gene scores from the ROS screen and the lipid peroxidation screen. High-signal hits are shown in red and low signal hits in blue. Genes discussed in the paper are highlighted in orange.

(F) Gene scores from the lysosome screen and the iron screen. Genes are color-coded by pathways.

(G) Heatmap showing gene scores across screens (rows) for genes that are among the top 20 high-signal or low-signal hits in at least one screen (columns) . Rows and columns are hierarchically clustered. Genes are color-coded by pathways.

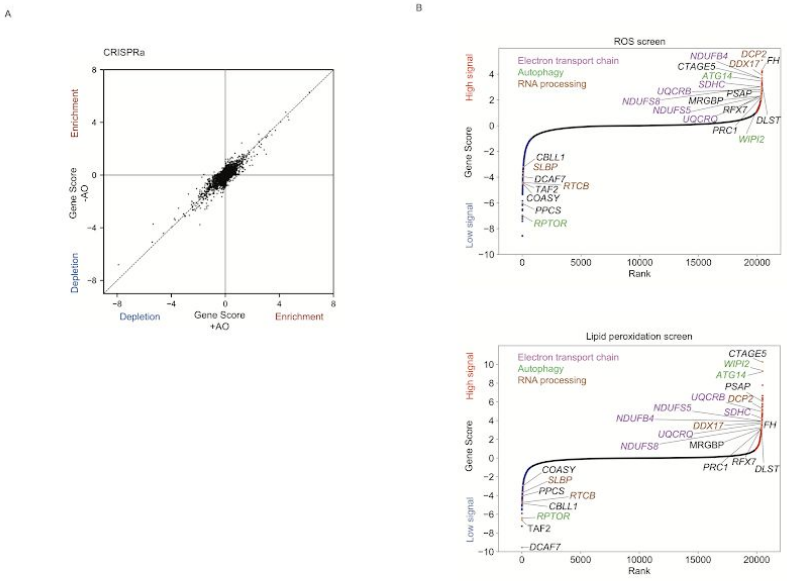

Fig.3.4. Comparing CRISPRa survival screens in +AO and -AO conditions and common hits in ROS and lipid peroxidation screens

(A) Comparing gene scores in +AO and -AO conditions for CRISPRa survival screens

(B) Screen results from ROS and lipid peroxidation screens shown as ranked gene scores, highlighting genes that are among the top 100 enrichment or depletion hits in both screens. Gene labels are color-coded by pathways.

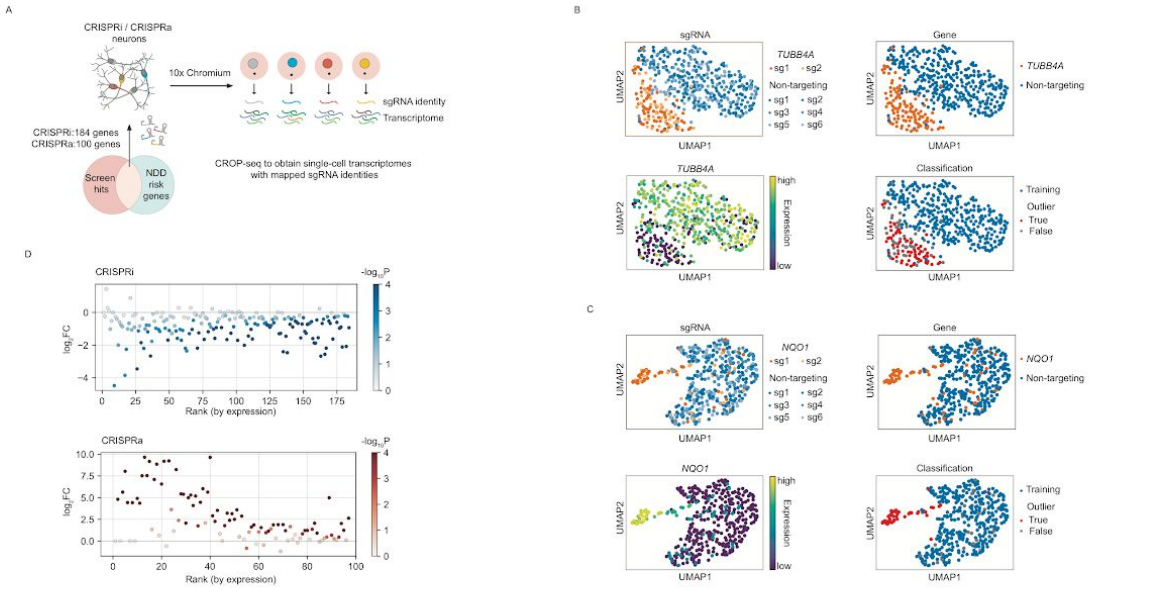

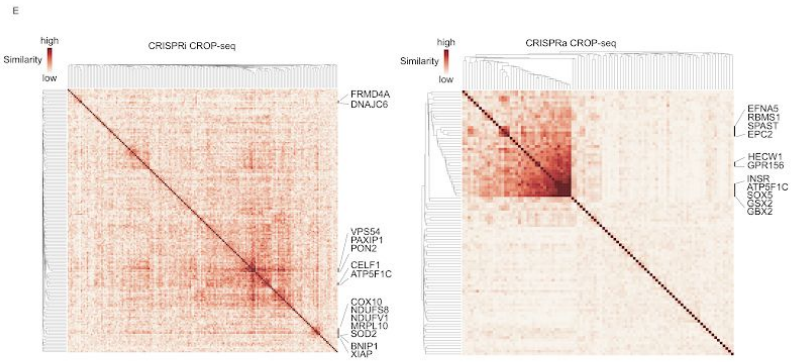

G

	Gene module	Enriched pathway(s)	
CRISPRi	M1	ribosomal proteins	intracellular transport
	M2	zinc-finger proeins	transcription regulation
	M3	response to external stimulus	cell communication
	M4	oxidative phosphorylation	
	M5	neurogenesis	synaptic transmission
	M6	N/A	
	M7	regulation of cell motility	regulation of response to stress
	M8	N/A	
	M9	axon guidance	phosphatidylinositol phosphorylation
	M10	transcription regulator activity	
CRISPRa	M1	neurogenesis	intracellular transport
	M2	ribosome biogenesis	ncRNA metabolic process
	M3	N/A	
	M4	zinc-finger proeins	
	M5	cell cycle	
	M6	gene expression	
	M7	oxidative phosphorylation	mitochondria-encoded genes
	M8	neuron differentiation	spinal cord motor neuron cell fate specification

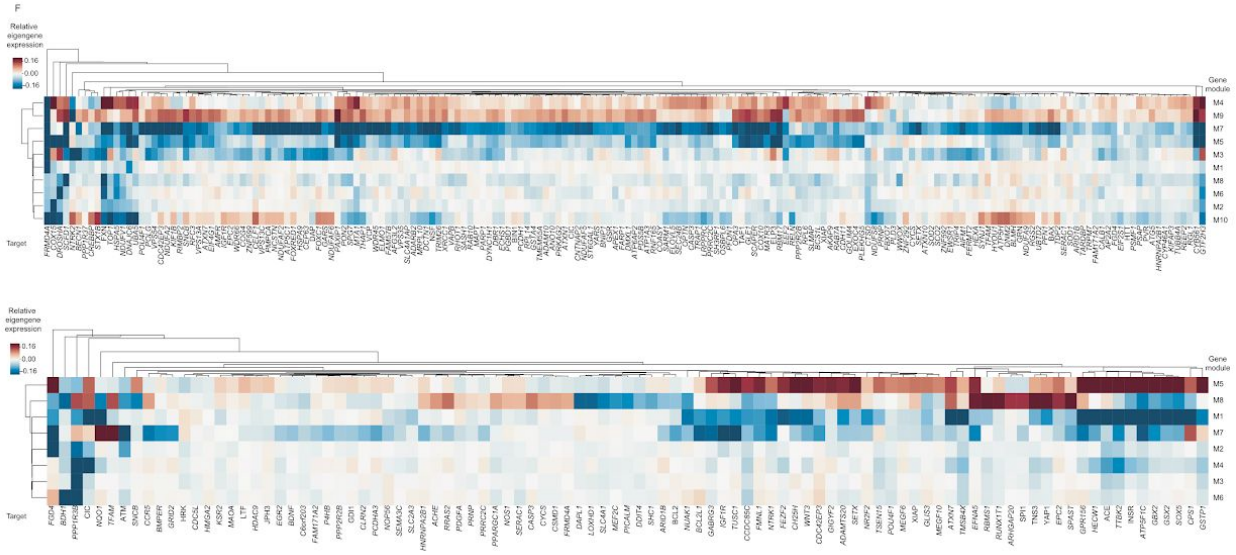

Fig.3.5. CROP-seq reveals transcriptomic responses to perturbations of neurodegenerative disease-associated hit genes in human iPSC-derived neurons

(A) Hit genes from our screens that are also associated with neurodegenerative diseases are analyzed by CROP-seq to detect their knockdown or overexpression effects on gene expression at single-cell resolution in human iPSC-derived neurons.

(B&C) Examples of CROP-seq results showing on-target knockdown (*TUBB4A* in CRISPRi, B) or overexpression (*NQO1* in CRISPRa, C) and the classification method, shown as 2-dimensional UMAP projection.

(D) Summary of on-target knockdown in CRISPRi (top) or overexpression in CRISPRa (bottom) for all target genes in the CROP-seq libraries. $\log_2$FC represents the $\log_2$ fold change of the mean expression of a target gene in perturbed cells (i.e. cells expressing sgRNAs targeting that gene) compared to unperturbed cells (i.e. cells expressing non-targeting control sgRNAs). P values were calculated by the Wilcoxon rank-sum test. Target genes are ranked by their expression in unperturbed cells.

(E) Pairwise similarities of differentially expressed genes among perturbations. Similarity scores were determined by the OrderedList package in R (see Methods). Genes in strong clustered are indicated.

(F & G) Eigengene expression of gene modules identified from WGCNA analysis in cells containing different perturbations relative to unperturbed cells (F). Enriched pathways in each module are shown in G.

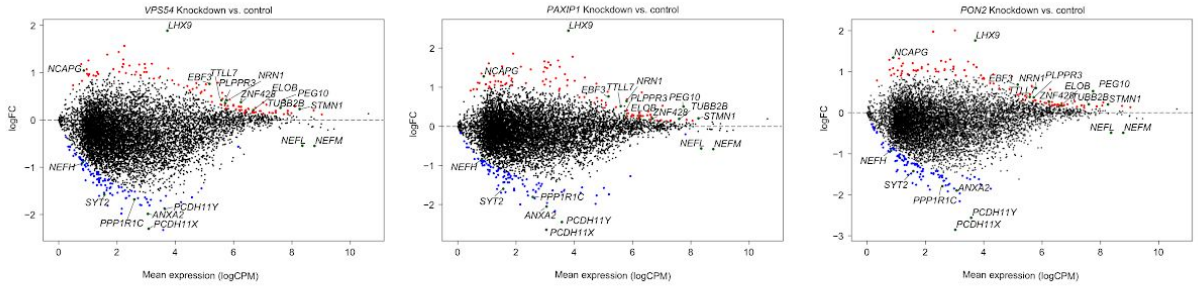

Fig.3.6. Shared signatures of transcriptomic responses to the knockdown of *VPS54*, *PAXIP1* and *PON2* in human iPSC-derived neurons

Transcriptomic changes induced by knockdown of *VPS54* (left), *PAXIP1* (middle) and *PON2* (right) in neurons. For each perturbation, the top 200 upregulated and downregulated genes compared to control (i.e. unperturbed cells) are shown in red and blue, respectively. Within these, shared genes among all three perturbations are highlighted in green.

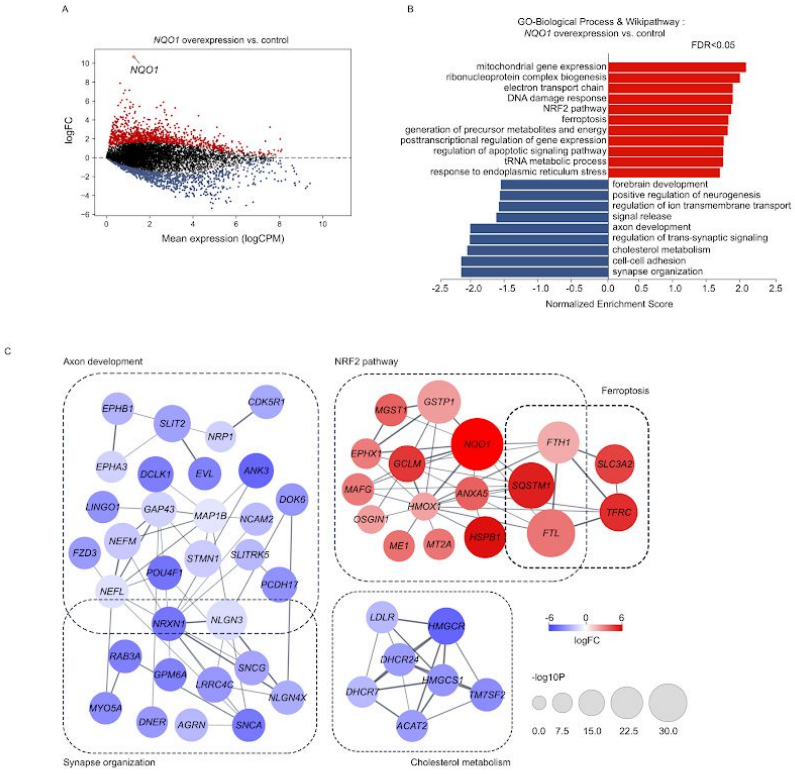

Fig.3.7. Overexpression of *NQO1* induces unexpected transcriptome changes in human iPSC-derived neurons

(A) Transcriptomic changes induced by *NQO1* overexpression in neurons. Significantly upregulated and downregulated genes (q-value < 0.01) are shown in red and blue, respectively.

(B) Pathway analysis showing enriched pathways in upregulated and downregulated genes in *NQO1*-overexpressing neurons.

(C) String-db association networks of selected pathways enriched in upregulated and downregulated genes. Genes with stronger associations are connected by thicker lines. Colors and sizes of nodes reflect $\log_2$ fold changes (logFCs) and significances ($-\log_{10}$P) of DEGs, respectively.

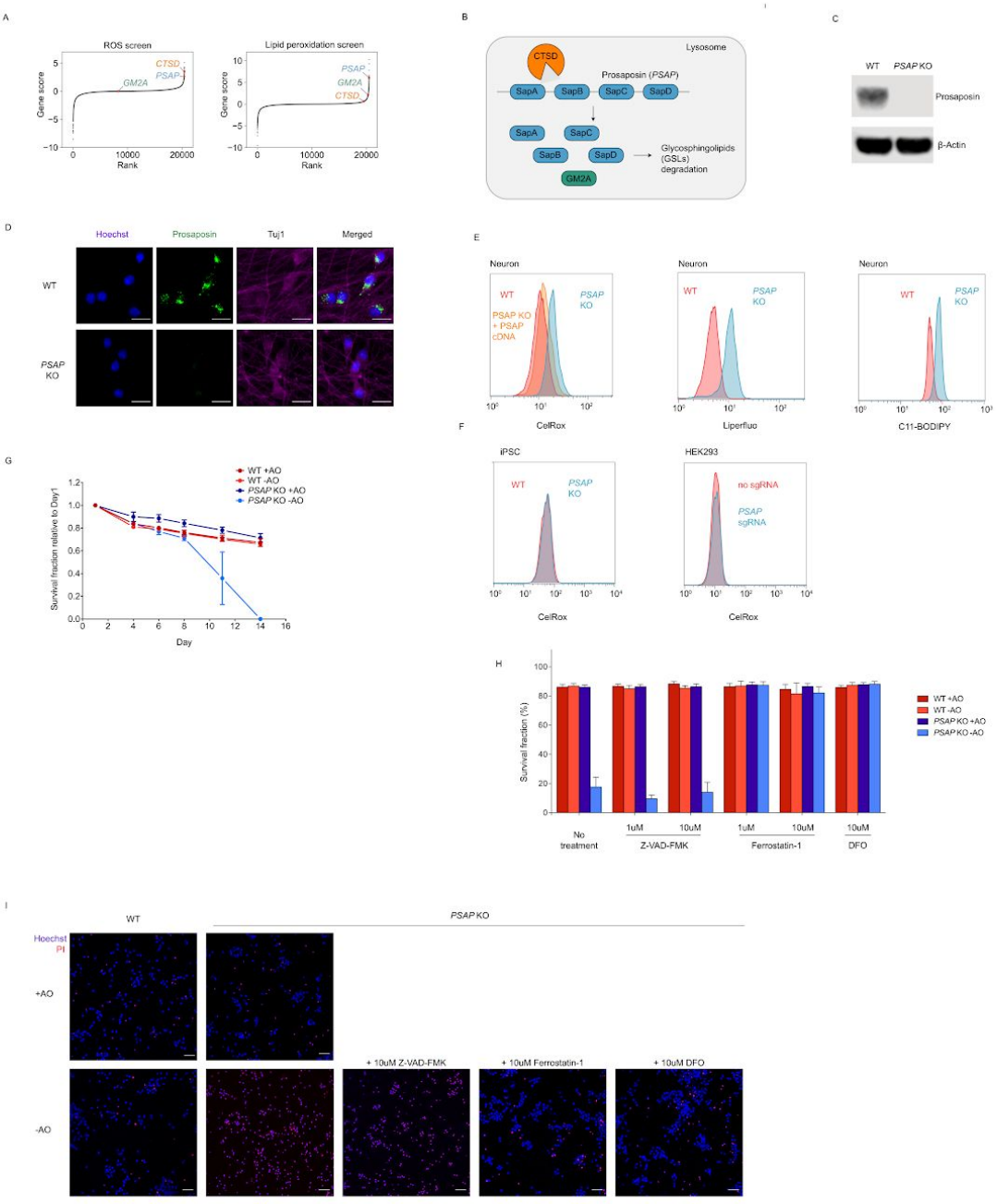

Fig.3.8. Depletion of *PSAP* induces ROS and lipid peroxidation in neurons and causes neuronal ferroptosis in the absence of antioxidants

(A) Results from the ROS screen and the lipid peroxidation screen, highlighting *PSAP* and the related genes *CTSD* and *GM2A*.

(B) Prosaposin is processed in the lysosome by cathepsin D (encoded by *CTSD*) into saposin subunits, which function together with GM2A as activators for GSL degradation.

(C) Western blot showing the depletion of prosaposin in the *PSAP* KO iPSC line.

(D) Representative immunofluorescence microscopy images showing the depletion of prosaposin in *PSAP* KO neurons. WT and *PSAP* KO neurons were fixed and stained by antibodies against prosaposin (shown in green) and the neuronal marker Tuj1 (shown in purple). Nuclei were counterstained by Hoechst, shown in blue. Scale bar, 20 μm.

(E) ROS levels (as indicated by CellRox, left) and lipid peroxidation levels (as indicated by Liperfluo and C11-BODIPY) in WT and *PSAP* KO neurons, measured by flow cytometry.

(F) ROS levels in iPSCs and HEK293s in WT and *PSAP* depletion backgrounds (*PSAP* KO for iPSCs and *PSAP* knockdown by CRISPRi in HEK293s), measured by flow cytometry.

(G) Survival curves for WT and *PSAP* KO neurons cultured in normal neuronal medium (+AO) or medium lack of antioxidants (-AO), quantified by imaging using Hoechst stain (cells)and propidium iodide (PI) (dead cells). Survival fraction is calculated as (total cell count - dead cell count) / total cell count. Data is shown as mean ± sd, n = 4 culture wells per group. 16 imaging fields were averaged for each well.

(H) Survival fractions of WT and *PSAP* KO neurons treated with different cell death inhibitors under +AO or -AO conditions, quantified by imaging in the same way as for G. Data is shown as mean ± sd, n = 32 imaging fields per group.

(I) Representative images for the Hoechst (shown in blue) and PI (shown in red) staining in H. Scale bar, 50 μm.

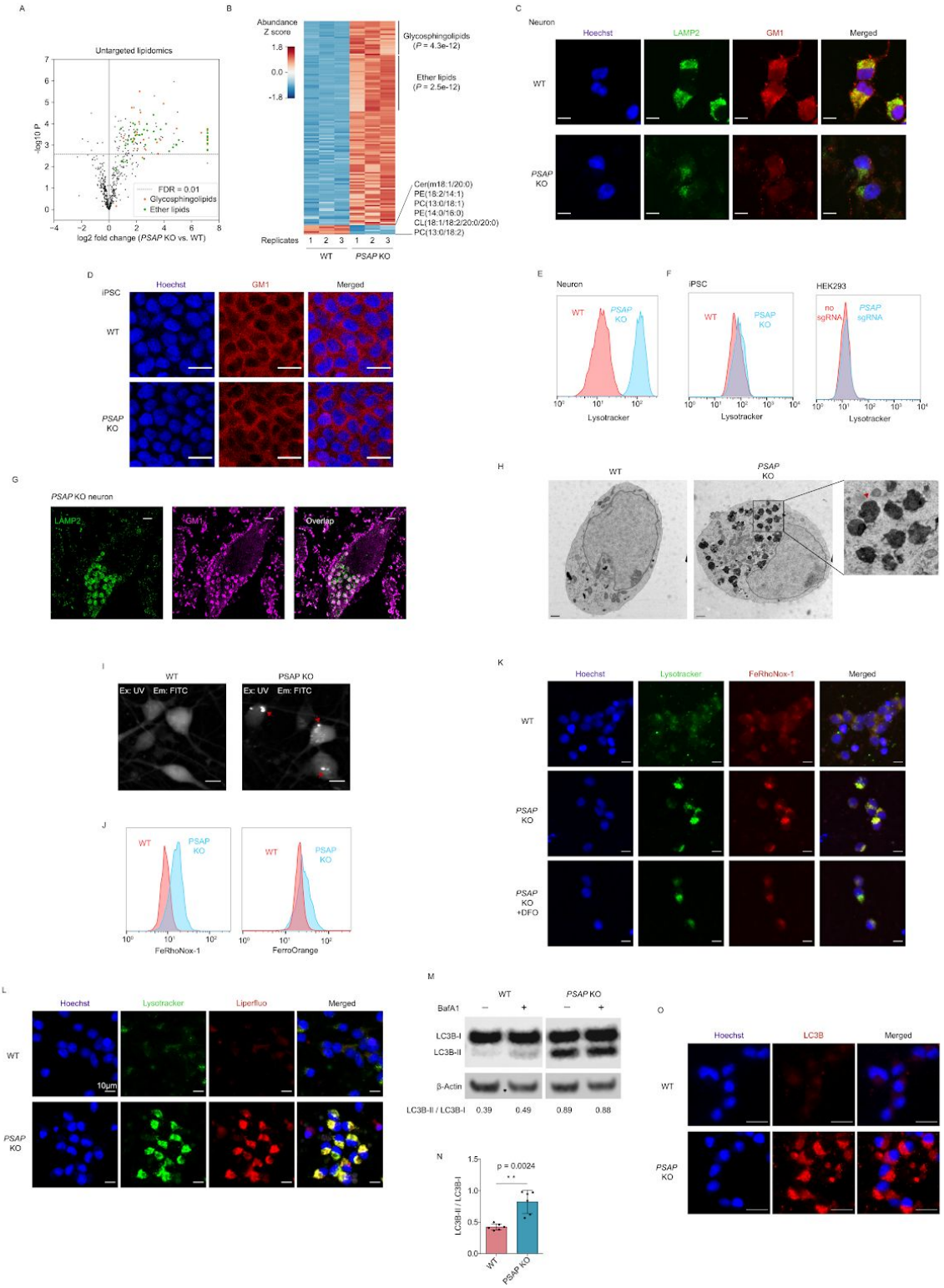
A
Untargeted lipidomics
-log10 P
log2 fold change (PSAP KO vs. WT)
FDR = 0.01
Glycosphingolipids
Ether lipids
B
Abundance
Z score
Glycosphingolipids
(P = 4.3e-12)
Ether lipids
(P = 2.5e-12)
Cer(m18:1/20:0)
PE(18:2/14:1)
PC(13:0/18:1)
PE(14:0/16:0)
CL(18:1/18:2/20:0/20:0)
PC(13:0/18:2)
Replicates
WT
PSAP KO
C
Neuron
Hoechst
LAMP2
GM1
Merged
WT
PSAP KO
D
iPSC
Hoechst
GM1
Merged
WT
PSAP KO
E
Neuron
WT
PSAP KO
Lysotracker
F
iPSC
HEK293
WT
PSAP KO
no sgRNA
PSAP sgRNA
Lysotracker
G
PSAP KO neuron
LAMP2
GM1
Overlap
H
WT
PSAP KO
I
WT
PSAP KO
Ex: UV
Em: FITC
J
WT
PSAP KO
FeRhoNox-1
FerroOrange
K
Hoechst
Lysotracker
FeRhoNox-1
Merged
WT
PSAP KO
PSAP KO +DFO
L
Hoechst
Lysotracker
Liperfluo
Merged
WT
PSAP KO
10μm
M
WT
PSAP KO
BafA1
LC3B-I
LC3B-II
β-Actin
LC3B-II / LC3B-I
0.39
0.49
0.89
0.88
N
LC3B-II / LC3B-I
p = 0.0024
WT
PSAP KO
O
Hoechst
LC3B
Merged
WT
PSAP KO

Fig.3.9. Depletion of *PSAP* in neurons disrupts glycosphingolipid degradation and causes lipofuscin formation in the lysosome, which accumulates iron and generates ROS that oxidize lipids

(A) Untargeted lipidomics comparing abundances of different lipid species in WT and *PSAP* KO neurons. P values were calculated using tudent's t-test (n=3 replicates per group). Dashed line, P value cutoff for FDR<0.01. All glycosphingolipids (GSLs) are shown in orange and ether lipids in green.

(B) Heatmap showing the abundances of significantly increased or decreased lipids in *PSAP* KO neurons as compared to WT (FDR<0.01). Enrichment P values for glycosphingolipids and ether lipids were calculated using Fisher's exact test. Lipid abundances were Z score-normalized across samples.

(C) Representative immunofluorescence microscopy images for WT and *PSAP* KO neurons stained with LAMP2 antibodies (shown in green) and GM1 antibodies (shown in red). Nuclei were counterstained by Hoechst, shown in blue. Scale bar, 10 μm.

(D) Representative immunofluorescence microscopy images for WT and *PSAP* KO iPSCs stained with GM1 antibodies (shown in red). Nuclei were counterstained by Hoechst, shown in blue. Scale bar, 20 μm

(E&F) Lysotracker signals measured by flow cytometry in WT and *PSAP* KO neurons (E), WT and *PSAP* KO iPSCs (F, left) and WT (no sgRNA) and *PSAP* knockdown (*PSAP* sgRNA) HEK293s (F,right).

(G) Two-color STORM super-resolution images for neurons stained with LAMP2 antibodies (shown in green) and GM1 antibodies (shown in magenta). Scale bar, 2 μm.

(H) Electron microscopy images for WT and *PSAP* KO neurons. Arrow, a representative structure of lipofuscin. Scale bar, 1 μm.

(I) Representative images for autofluorescence in WT and *PSAP* KO neurons. Excitation, UV (405nm). Emission, FITC (525/20 nm). Scale bar, 10 μm.

(J) Labile iron levels in WT and *PSAP* KO neurons. Neurons were stained with iron indicators, including FeRhoNox-1 (left) and FerroOrange (right). Staining signals were measured by flow cytometry.

(K) Representative fluorescence microscopy images for WT neurons, *PSAP* KO neurons and *PSAP* KO neurons treated with 10 µM DFO for 3 days, stained with Lysotracker (shown in green) and FeRhoNox-1 (shown in red). Nuclei were counterstained by Hoechst, shown in blue. Scale bar, 10 µm.

(L) Representative fluorescence microscopy images for WT and *PSAP* KO neurons stained with Lysotracker (shown in green) and Liperfluo (shown in red). Nuclei were counterstained by Hoechst, shown in blue. Scale bar, 10 µm.

(M) Western blot showing protein levels of phosphatidylethanolamine (PE)-conjugated LC3B (LC3B-II) and unconjugated LC3B (LC3B-I) in WT and *PSAP* KO neurons in the absence or presence of Bafilomycin A1 (BafA1). β-Actin was used as loading control. Ratios of LC3B-II to LC3B-I are indicated at the bottom.

(N) Quantification of LC3B-II / LC3B-I ratios for WT and *PSAP* KO neurons (mean ± sd, n = 6 independent experiments).

(O) Representative immunofluorescence microscopy images for WT and *PSAP* KO neurons, stained with LC3B antibodies (shown in red). Nuclei were counterstained by Hoechst, shown in blue. Scale bar, 20 µm.

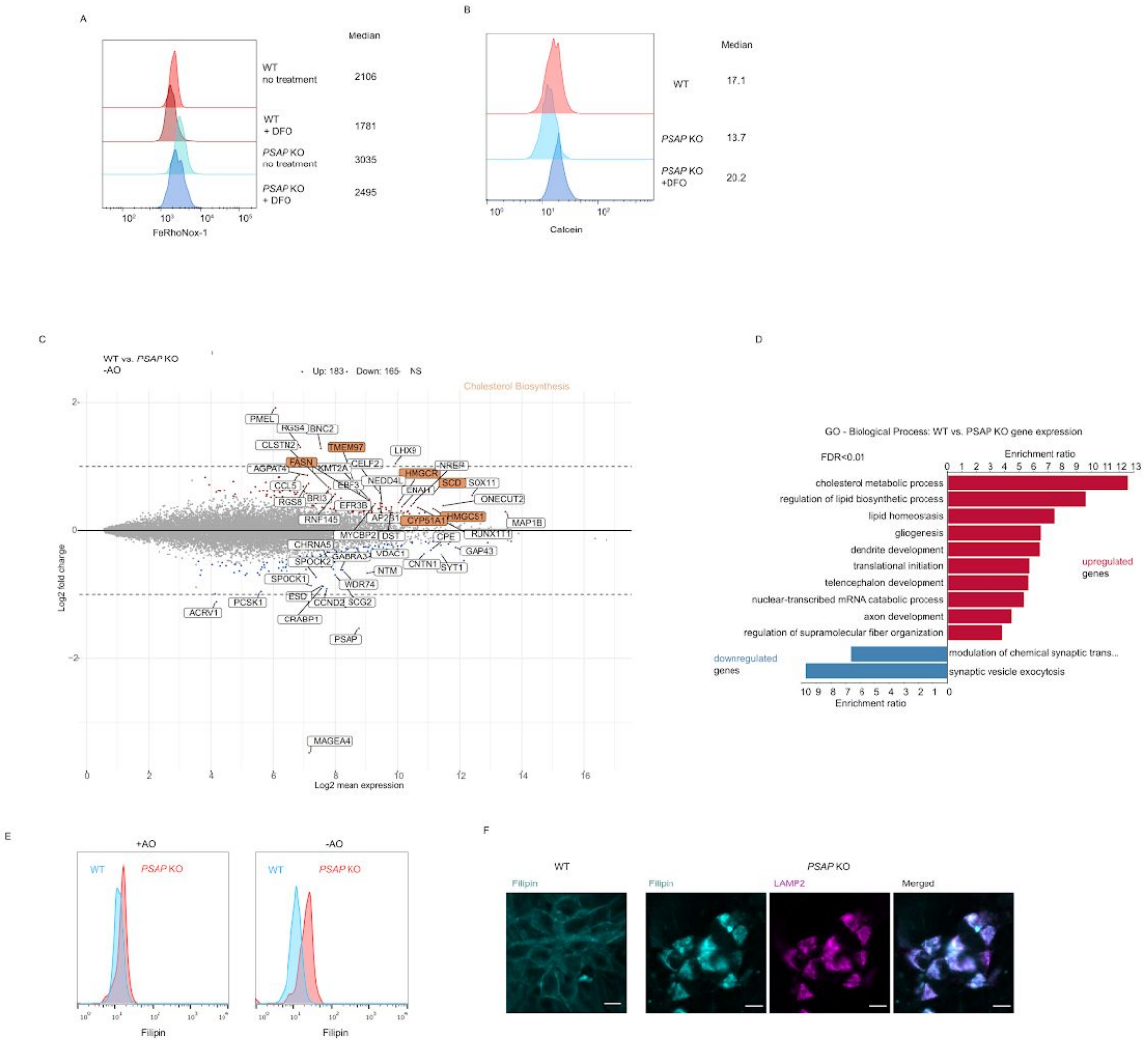

Fig.3.10. Characterization of *PSAP* KO neurons

(A) Labile iron levels in WT and *PSAP* KO neurons with or without DFO treatment. Cells were stained by FeRhoNox-1 and measured by flow cytometry. Median signal intensities are indicated.

(B) Labile iron levels in WT neurons, *PSAP* KO neurons and *PSAP* KO neurons with DFO treatment. Cells were stained by Calcein and measured by flow cytometry. Median signal intensities are indicated.

(C) Gene expression changes in *PSAP* KO neurons as compared to WT. Genes that are significantly upregulated and downregulated in *PSAP* KO neurons are shown in red and blue respectively (FDR<0.05). Top 50 up- and down-regulated genes are labeled, among which genes involved in the cholesterol biosynthesis pathway are highlighted in orange.

(D) GO term enrichment analysis for significantly up- and down-regulated genes (FDR<0.05) in *PSAP* KO neurons. Significantly enriched Biological Process terms are shown (FDR<0.01).

(E) Cholesterol levels measured by flow cytometry of Filipin-stained WT and *PSAP* KO neurons in +AO and -AO conditions.

(F) Representative fluorescence microscopy images of WT and *PSAP* KO neurons stained with Filipin (shown in cyan) and LAMP2 antibodies (shown for *PSAP* KO neurons, in red). Scale bar, 10 μm.

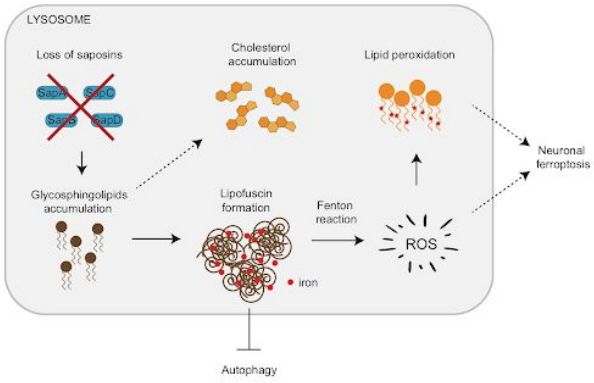

Fig.3.11. A working model for *PSAP* depletion inducing neuronal ferroptosis
Knocking out *PSAP* leads to loss of saposins, which blocks glycosphingolipid (GSL) degradation in the lysosome. The build-up of GSLs leads to lipofuscin formation, which accumulates iron and generates ROS through the Fenton reaction. ROS then peroxidize lipids and cause neuronal ferroptosis in the absence of antioxidants

MATERIALS AND METHODS

Human iPSCs culture and neuronal differentiation

Human iPSCs (male WTC11 background (Miyaoka et al., 2014)) were cultured in StemFlex Medium (GIBCO/Thermo Fisher Scientific; Cat. No. A3349401) in plates or dishes coated with Growth Factor Reduced, Phenol Red-Free, LDEV-Free Matrigel Basement Membrane Matrix (Corning; Cat. No. 356231) diluted 1:100 in Knockout DMEM (GIBCO/ v; Cat. No. 10829-018). StemFlex Medium was replaced every other day or every day once cells reached 50% confluence. When 80%–90% confluent, cells were dissociated using StemPro Accutase Cell Dissociation Reagent (GIBCO/Thermo Fisher Scientific; Cat. No. A11105-01) at 37°C for 5 min, centrifuged at 200 g for 5 min, resuspended in StemFlex Medium supplemented with 10 nM Y-27632 dihydrochloride ROCK inhibitor (Tocris; Cat. No. 125410) and plated onto Matrigel-coated plates or dishes at desired number. Studies with human iPSCs at UCSF were approved by the Human Gamete, Embryo and Stem Cell Research (GESCR) Committee.

The CRISPRi- and CRISPRa-iPSC lines used in this study were engineered to express mNGN2 under a doxycycline-inducible system in the AAVS1 safe harbor locus. For their neuronal differentiation, we followed our previously described protocol (Tian et al., 2019). Briefly, iPSCs were pre-differentiated in matrigel-coated plates or dishes in N2 Pre-Differentiation Medium containing the following: Knockout DMEM/F12 (GIBCO/Thermo Fisher Scientific; Cat. No. 12660-012) as the base, 1X MEM Non-Essential Amino Acids (GIBCO/Thermo Fisher Scientific; Cat. No. 11140-050), 1X N2 Supplement (GIBCO/ Thermo Fisher Scientific; Cat. No. 17502-048), 10 ng/mL NT-3

(PeproTech; Cat. No. 450-03), 10ng/mL BDNF (PeproTech; Cat. No. 450-02), 1 µg/mL Mouse Laminin (Thermo Fisher Scientific; Cat. No. 23017-015), 10nM ROCK inhibitor, and 2 µg/mL doxycycline to induce expression of mNGN2. After three days, on the day referred to hereafter as Day 0, pre-differentiated cells were re-plated into BioCoat Poly-D-Lysine-coated plates or dishes (Corning; assorted Cat. No.) in regular Neuronal Medium, which we will refer to as +AO Neuronal Medium, containing the following: half DMEM/F12 (GIBCO/Thermo Fisher Scientific; Cat. No. 11320-033) and half Neurobasal-A (GIBCO/Thermo Fisher Scientific; Cat. No. 10888-022) as the base, 1X MEM Non-Essential Amino Acids, 0.5X GlutaMAX Supplement (GIBCO/Thermo Fisher Scientific; Cat. No. 35050-061), 0.5X N2 Supplement, 0.5X B27 Supplement (GIBCO/Thermo Fisher Scientific; Cat. No. 17504-044), 10ng/mL NT-3, 10ng/mL BDNF and 1 µg/mL Mouse Laminin. For -AO experiments, we used a medium we refer to as -AO Neuronal Medium, in which B-27 Supplement minus antioxidants (GIBCO/Thermo Fisher Scientific; Cat. No. 10889-038) was used instead of regular B27 in the +AO Neuronal Medium . Neuronal Medium was half-replaced every week.

Molecular cloning

The CLYBL-targeting inducible CRISPRa vector pRT43 containing CAG-driven DHFR-dCas9-VPH-T2A-EGFP was generated by sub-cloning DHFR-dCas9-VPH-T2A-EGFP from plasmid PB-CAG-DDdCas9VPH-T2A-GFP-IRES-Neo to the downstream of a CAG promoter in CLYBL-targeting plasmid pUCM-CLYBL-hNIL digested by SalI and EcoRV.

(PB-CAG-DDdCas9VPH-T2A-GFP-IRES-Neo was a gift from Timo Otonkoski (Addgene plasmid # 102886 ; http://n2t.net/addgene:102886 ; RRID:Addgene_102886) and pUCM-CLYBL-hNIL was a gift from Michael Ward (Addgene plasmid # 105841 ; http://n2t.net/addgene:105841 ; RRID:Addgene_105841))

CRISPRa-iPSC cell line generation

WTC11 iPSCs harboring a single-copy of doxycycline-inducible mouse NGN2 at the AAVS1 locus (Ngn2-iPSCs, Wang et al., 2017; Fernandopulle et al., 2018) were used as the parental iPSC line for further genetic engineering. iPSCs were transfected with pRT43 containing DHFR-dCas9-VPH and TALENS targeting the human CLYBL intragenic safe harbor locus (between exons 2 and 3) (pZT-C13-R1 and pZT- C13-L1, gifts from Jizhong Zou (Addgene plasmid # 62196 ; http://n2t.net/addgene:62196 ; RRID:Addgene_62196, and Addgene plasmid # 62197 ; http://n2t.net/addgene:62197 ; RRID:Addgene_62197) using Lipofectamine Stem (Invitrogen/Thermo Fisher Scientific; Cat. No. STEM00003). Monoclonal lines were isolated by limiting dilution and CLYBL integration was confirmed by PCR genotyping. Karyotype testing (Cell Line Genetics) was normal for the clonal line used for further experiments in this study, which we termed CRISPRa iPSCs.

Genome-wide survival-based and FACS-based screens

The genome-wide CRISPRi and CRISPRa libraries hCRISPRi-v2 and hCRISPRa-v2 (Horlbeck et al., 2016), consisting of 7 sublibraries each (H1-H7), were

packaged into lentivirus as previously described (Tian et al., 2019). CRISPRi- and CRISPRa-iPSCs were infected by the sgRNA libraries at MOIs of 0.4-0.6 (as measured by the BFP fluorescence from the lentiviral vector) with approximately 1000x coverage per library element. Two days after infection, the cells were selected for lentiviral integration using puromycin (1 μg/mL) for 3 days as the cultures were expanded for the screens. After selection and expansion, a fraction of the cells (Day -3 iPSCs) were harvested and subjected to sample preparation for next-generation sequencing. Another fraction of Day -3 iPSCs, with a cell count corresponding to 1000x coverage per library element, were differentiated into neurons as described in the Human iPSCs Culture and Neuronal Differentiation subsection.

Neurons were cultured in either the +AO or -AO Neuronal Medium (see Human iPSCs Culture and Neuronal Differentiation subsection) for ten days. For the survival screens, Day 10 neurons were harvested and subjected to sample preparation for next-generation sequencing. For the FACS screens, Day 10 CRISPRi neurons cultured in the +AO medium and -AO medium were dissociated using Papain (Worthington; Code: PAP2; Cat. No.LK003178) and stained by CellRox Green (Invitrogen/Thermo Fisher Scientific; Cat. No. C10444) and Liperfluor (Dojindo Molecular Technologies, Inc.; Cat. No. L248-10) respectively (see Cell Staining by Fluorescent Probes) and sorted into high and low signal populations in each screen corresponding to the top 40% and bottom 40% of the staining signal distribution, followed by sample preparation for next-generation sequencing.

For each screen sample, genomic DNA was isolated using a Macherey-Nagel Blood L kit (Machery-Nagel; Cat. No. 740954.20). sgRNA-encoding regions were amplified and sequenced on an Illumina HiSeq- 4000 as previously described (Gilbert et al., 2014).

Batch characterization screens

The batch characterization library contained 2,190 sgRNAs targeting 730 genes that were hits in at least one of the ROS and lipid peroxidation screens with 3 sgRNAs per gene selected based on their phenotypes in the primary screens, and 100 non-targeting control sgRNAs. A pool of sgRNA-containing oligonucleotides were synthesized by Agilent Technologies and cloned into our optimized sgRNA expression vector as previously described (Gilbert et al., 2014). CRISPRi-iPSCs were transduced with the batch characterization library, puromycin selected and differentiated into neurons as for the primary screens. Day10 neurons were stained with FeRhoNox-1 (Goryo Chemical; Cat. No. GC901) or Lysotracker-green (Cell Signaling Technology; Cat. No. 8783S) and sorted into high and low signal populations corresponding to the top 40% and bottom 40% of the staining signal distribution. Screen samples were processed and sequenced by next-generation sequencing as described above.

CROP-seq

For the CROP-seq experiments, we included 184 genes for CRISPRi and 100 genes for CRISPRa, which were hits in at least one of our genome-wide pooled screens

and were also associated with human neurodegenerative diseases (NDDs). We curated a list of NDD-associated genes based on the literature and the DisGeNET database (https://www.disgenet.org/). The CROP-seq libraries included 2 sgRNAs per gene plus 6 non-targeting control sgRNAs, for a total of 374 sgRNAs for CRISPRi and 206 sgRNAs for CRISPRa. Top and bottom strands of sgRNA oligos were synthesized (Integrated DNA Technologies) and annealed in an arrayed format. The annealed sgRNAs were then pooled in equal amounts and ligated into our optimized CROP-seq vector (Gilbert et al., 2014).

The CROP-seq experiments were carried out similarly as previously described (Tian et al., 2019). Briefly, Day 0 CRISPRi and CRISPRa neurons were infected by the corresponding CROP-seq sgRNA library at a MOI of 0.1-0.2, followed by puromycin selection at 4 μg/ml for 3 days and recovery. On Day 10, neurons were dissociated with Papain and approximately 98,000 CRISPRi neurons and 50,000 CRISPRa neurons were loaded into 10X chips with about 25,000 input cells per lane. Sample preparations were performed using the ChromiumNext GEM Single Cell 3′ Reagent Kits v3.1 (10X Genomics; Cat. No.PN-1000121) according to the manufacturer's protocol. To facilitate sgRNA assignment, sgRNA-containing transcripts were additionally amplified by hemi-nested PCR reactions as described (Tian et al., 2019). The sgRNA-enrichment libraries were separately indexed and sequenced as spike-ins alongside the whole-transcriptome scRNA-seq libraries using a NovaSeq 6000 using the following configuration: Read 1: 28, i7 index: 8, i5 index: 0, Read 2: 91.

Cell Staining by Fluorescent Probes

All stains were performed according to manufacturing protocols. For Filipin staining, cells were washed with PBS for 3 times and fixed with 3% paraformaldehyde for 1 hr at room temperature. Cells were then washed 3 times with PBS and incubated with 0.05 mg/ml Filipin III from *Streptomyces filipinensis* (Sigma; Cat. No. F4767-1MG) in PBS for 2 h at room temperature. Cells were washed with PBS 3 times before analysis. For staining using other live cell probes, cells were washed with PBS and incubated in DMEM containing appropriate concentrations of the probes at 37 °C as detailed below. Cells were washed with PBS before analysis. Concentrations and staining conditions for different probes were as follows: CellRox Green, 2.5 μM for 30 minutes; Lysotracker Green, 50 nM for 5 minutes; FeRhoNox-1, 5 μM for 60 minutes; Liperfluo, 5 μM for 30 minutes; C11-BODIPY, 2.5 μM for 30 minutes; FerroOrange (Dojindo Molecular Technologies, Inc.; Cat. No. F374-10), 1 μM for 30 minutes; Hoechst 33342 (Thermo Fisher Scientific; Cat. No. H3570), 1 μg/ml for 10 minutes; Propidium Iodide (PI)(Thermo Fisher Scientific; Cat. No. P1304MP), 1 μg/ml for 10 minutes.

Immunofluorescence

Cells were washed with PBS and fixed with 4% paraformaldehyde for 15 min at room temperature. After washing with PBS for 3 times, cells were permeabilized with 0.1% Triton X-100 for 10 min and blocked with 5% normal goat serum with 0.01% Triton X-100 in PBS for 1 hr at room temperature. Cells were then incubated with primary antibodies diluted in blocking buffer at 4 °C overnight. After that, cells were washed with

PBS for 3 times and incubated with secondary antibodies diluted in blocking buffer for 1 hr at room temperature. Cells were then washed with PBS for 3 times and stained with 10 μg/ml Hoechst 33342 (Thermo Fisher Scientific; Cat. No. H3570) for 10 min. Cells were imaged using a confocal microscope (Leica SP8) or an IN Cell Analyzer 6000 (GE; Cat. No. 28-9938-51). Primary antibodies used for immunofluorescence in this study were as follows: rabbit anti-PSAP antibody (1:50 dilution; Proteintech; Cat. No. 10801-1-AP), mouse anti-LAMP2 antibody (1:100 dilution; abcam; Cat. No. ab25631), rabbit anti-GM1 antibody (1:20 dilution; abcam; Cat. No. ab23943), rabbit anti-LC3B antibody (1:200 dilution; Cell Signaling Technology; Cat. No. 2775S) and chicken anti-TUJ1 antibody (1:500; AVES; Cat. No. TUJ). Secondary antibodies used in this study were as follows: goat anti-rabbit IgG Alexa Fluor 555 (1:500 dilution; abcam; Cat. No. ab150078), goat anti-mouse IgG Alexa Fluor 488 (1:500 dilution; abcam; Cat. No. ab150113) and goat anti-chicken IgG Alexa Fluor 647 (1:500 dilution; abcam; Cat. No. ab150171).

Western blots

Cells were lysed in RIPA buffer and 20-30 μg of total proteins were loaded into NuPAGE 4%–12% Bis-Tris Gels (Invitrogen, Cat# NP0336BOX). Subsequently, the gels were transferred onto nitrocellulose membranes and the membranes were blocked by Odyssey Blocking Buffer (PBS) (LI-COR, Cat#927-50000), followed by overnight incubation with primary antibodies at 4°C. After incubation, the membranes were washed three times with TBST and then incubated with secondary antibodies at room

temperature for 1 hr. The membranes were then washed 3 times with TBST and once with TBS and imaged on the Odyssey Fc Imaging system (LI-COR Cat# 2800). Digital images were processed and analyzed using ImageJ.

Primary antibodies used were mouse anti-β-Actin antibody (1:2000 dilution; Cell Signaling Technology; Cat. No. 3700), rabbit anti-PSAP antibody (1:1000 dilution; Proteintech; Cat. No. 10801-1-AP) and rabbit anti-LC3B antibody (1:1000 dilution; Cell Signaling Technology; Cat. No. 2775S). Secondary antibodies were IRDye 680RD goat anti-mouse IgG (1:20,000 dilution; LI-COR; Cat. No. 926-68070) and IRDye 800CW goat anti-rabbit IgG(1:20,000 dilution; LI-COR; Cat. No. 926-32211).

Generating *PSAP* KO iPSC line

An sgRNA targeting *PSAP* exon 2 (sgRNA sequence: GGACTGAAAGAATGCACCA) was cloned into plasmid px330-mcherry (px330-mcherry was a gift from Jinsong Li (Addgene plasmid # 98750 ; http://n2t.net/addgene:98750 ; RRID:Addgene_98750)). The plasmid was transfected into WT Ngn2-iPSCs using Lipofectamine Stem (Invitrogen/Thermo Fisher Scientific; Cat. No. STEM00003). Monoclonal lines were isolated in 96-well plates by limiting dilution. One clonal line was selected and frameshift indels were confirmed by Sanger sequencing. Protein level KO was confirmed by western blot and immunofluorescence (Fig. 5C,D). A normal karyotype was confirmed (Cell Line Genetics).

Bulk RNA sequencing

RNA was extracted from cells using the Quick-RNA Miniprep Kit (Zymo; Cat. No. R1054), and 3′-tag RNA-seq was performed by the DNA Technologies and Expression Analysis Core at the UC Davis Genome Center.

Electron Microscopy

Neurons grown on a poly-D-lysine coated 35-mm ibidi µ-Dish (ibidi; Cat. No. 81156) were fixed with 2.5% glutaraldehyde in 0.1 M sodium cacodylate buffer (EMS) for at least an hour at room temperature. Samples were further post-fixed with 1% osmium tetroxide and 1.6% potassium ferrocyanide, later dehydrated in graded series of ethanols, and embedded in epon araldite resin. Samples were then trimmed, 70nm sections were cut using Ultra cut E (Leica) and stained with 2% uranyl acetate and Reynold's lead citrate. Images were acquired on a FEI Tecnai 12 120KV TEM (FEI) and data was recorded using UltraScan 1000 Digital Micrograph 3 software (Gatan Inc.)

STORM super-resolution microscopy

Sample preparation and STORM imaging were performed as described (Hauser et al., 2018). Samples were fixed in 4% paraformaldehyde (Electron Microscopy Sciences) in PBS (Corning) for 30 minutes at room temperature, followed by three times of washing with PBS. Prior to immunostaining, samples were treated by a blocking buffer (BB) of 3% bovine serum albumin (Sigma) and 0.1% Triton-X100 (Sigma) in PBS for 1 hour at room temperature. Primary antibodies were diluted in BB and labeled at 4C

overnight. Unbound antibodies were rinsed three times, 10 minutes each time with a washing buffer (WB) prepared by 10X dilution of BB in PBS. Secondary antibodies Dye-labeled secondary antibodies from Invitrogen or Jackson ImmunoResearch Laboratories were diluted in BB and labeled at room temperature for 1 hour, followed by three times of washing with WB.

Before STORM imaging, the sample was mounted in a standard STORM imaging buffer of 5% [w/v] glucose (Sigma), 0.1 M cysteamine (Sigma), 0.8 mg/mL glucose oxidase (Sigma), and 40 mg/mL catalase (Sigma) in 0.1 M Tris-HCl pH 7.5 (Corning). Imaging was carried out on a custom setup modified from a Nikon Eclipse Ti-E inverted fluorescence microscope with an oil immersion objective (Nikon CFI Plan Apochromat λ, 100X, numerical aperture 1.45). Lasers at 405, 488, 560, and 647 nm illuminated the sample through the back focal plane of the microscope and were shifted toward the edge of the objective to illuminate an ~1 μm layer above the coverglass. A strong excitation laser of 647 nm or 560 nm (~2 kW/cm^2) was applied to photoswitch most of the AF647 or CF568 dye molecules into the dark state while also exciting the remaining dye molecules at a low density for single-molecule localization. A weak 405-nm laser (0-1 W/cm^2) was used simultaneously with the 647-nm or 560-nm laser to reactivate dye molecules in the dark state into the emitting state to acquire adequate sampling of the labeled molecules. 3D localization was achieved with astigmatism-based optics with a cylindrical lens (f = 1000.0 mm, Thorlabs) (Huang et al., 2008). Images were collected at 110 frames per second with an electron multiplying charge-coupled device camera (Andor iXon Ultra 897) for ~50,000 frames per image.

Raw single-molecule data were processed into 3D-STORM images as previously described [2]. Briefly, the point-spread function of each molecule was fitted by a 2D-Gaussian function to define its location in the image plane as well as in the axial direction (encoded in ellipticity). All localized positions were overlaid and the sample drift during imaging was corrected by autocorrelation in time.

Untargeted Lipidomics

The untargeted lipidomics experiment and primary analysis were performed by Cayman Chemical. Briefly, lipids were extracted using a methyl-tert-butyl ether (MTBE)-based liquid-liquid method. Cell pellets (approximately 100 µL in volume) were thawed on ice and transferred into 8-mL screw-cap tubes before adding 600 µL MeOH, the 600 µL MeOH containing 200 ng each of the internal standards TG(15:0/18:1-d7/15:0), PC(15:0/18:1-d7), PE(15:0/18:1-d7), PG(15:0/18:1-d7), and PI(15:0/18:1-d7) (EquiSPLASH, Avanti Polar Lipids), and finally 4 mL MTBE. After vigorous vortexing, the samples were incubated at room temperature on a shaker for 1 h. For phase separation, 1 mL water was added,and samples were vortexed and centrifuged for 10 min at 1000 x g. The upper organic phase of each sample was carefully removed using a Pasteur pipette and transferred into a pre- weighed empty glass tube. The remaining aqueous phase was re-extracted with 2 mL of clean MTBE/methanol/water 10:3:2.5 (v/v/v). The two upper organic phases were combined and dried under vacuum in a SpeedVac concentrator. The dried lipid extracts were weighed and resuspended in 100 µL isopropanol/acetonitrile 1:1 (v/v) for untargeted

lipidomic analysis by LC-MS/MS. Triplicates of samples for WT and *PSAP* KO neurons were analyzed.

Data analysis

Pooled CRISPR screens

Pooled CRISPR screens were analyzed using the MAGeCK-iNC pipeline as described (Tian et al., 2019). Briefly, raw sequencing reads from next-generation sequencing were cropped and aligned to the reference using Bowtie (Langmead et al., 2009) to determine sgRNA counts in each sample. Counts files for samples subject to comparison were entered into the MAGeCK-iNC software (kampmannlab.ucsf.edu/mageck-inc). Phenotype scores and significance P values were determined for all target genes in the library, as well as for 'negative-control-quasi-genes' that were generated by random sampling from non-targeting control sgRNAs. A gene score was calculated for each gene, which was defined as the product of the phenotype score and $-\log_{10}$(P value). To determine hit genes, a gene score cutoff value was chosen to make sure the false-discovery rate (FDR) is less than 0.05.

CROP-seq

CROP-seq analysis was performed similarly to previously described (Tian et al., 2019). Cellranger (version 3.1.0,10X Genomics) with default parameters was used to align reads and generate digital expression matrices from single-cell sequencing data.

Approximately 58,000 CRISPRi neurons and 38,000 CRISPRa neurons were detected. The mean reads per cell was around 48,000 for CRISPRi and 36,000 for CRISPRa. Median number of genes detected per cell was around 4,341 for iPSCs and 3,100 for CRISPRa.

sgRNA-enrichment libraries were analyzed using methods previously described (Hill et al., 2018) to obtain sgRNA UMI counts for each cell barcode. For a given cell, sgRNA(s) whose UMI counts were greater than 4 standard deviations of the mean UMI counts of all sgRNAs were assigned to that cell as its identity. Single sgRNAs could be assigned to about 35,000 CRISPRi cells and about 21,000 CRISPRa cells, which were retained for further analysis.

The Scanpy package (version 1.4.6) (Wolf et al., 2018) implemented in Python was used for downstream analysis of the digital expression matrices with mapped sgRNA identities. To ensure data quality, a stringent criterion was applied to filter cells based on the number of genes detected (> 2000 for CRISPRi and > 1500 for CRISPRa) and percentage of mitochondrial transcript counts (< 0.15%). Genes that had less than 0.5 UMIs on average in all perturbation groups were filtered out. To select cells in which functional perturbations happened, we leveraged an unsupervised outlier detection method based on the local outlier factor (LOF) using the LocalOutlierFactor function in the Python package scikit-learn (version 0.23.0). A similar strategy was described previously (Adamson et al., 2016). Specifically, for every target gene, we selected two populations of cells, including one population of cells that were mapped with sgRNAs targeting that gene (i.e. perturbed group) and another population of cells that were

mapped with non-targeting control sgRNAs (i.e. control group). We then identified differentially expressed genes (DEGs) between the two populations by t-tests at $p < 0.05$. A gene-expression matrix containing only expression of DEGs in cells from the two populations was generated and principal component analysis (PCA) was performed to reduce the matrix to 4 dimensions. Cells in the control group in the 4-dimensional space were used as the training set to fit a LocalOutlierFactor model. Then, the model was used to determine whether a cell in the perturbed group was an 'outlier' based on the extent it deviated from the controls. The 'outliers' were considered as cells in which functional perturbations occurred and were retained for downstream analysis. DEGs for each perturbation group compared to control group were then determined by t-tests using the diffxpy package in Python.

A mean gene-expression matrix was generated for different perturbation groups (including the control group) by averaging the normalized expression profile of all cells within that group. This matrix was used for weighted correlation network analysis (WGCNA) using the WGCNA package (version 1.69), (Langfelder and Horvath, 2008) implemented in R. The blockwiseModules function was used to detect gene modules that were co-regulated in different perturbation groups and to determine eigengene expression of each module in each perturbation group. Relative eigengene expression values were calculated by subtracting the eigengene expression value of each module in the control group from that in each perturbation group.

RNA-seq

Raw sequencing reads from 3′-tag RNA-seq were mapped to the human reference transcriptome (GRCh38, Ensembl Release 97) using Salmon (v.0.14.139) with the '–noLengthCorrection' option to obtain transcript abundance counts. Gene-level count estimates were obtained using tximport (v.1.8.040) with default settings. Subsequently, genes with more than 10 counts were retained for differential gene-expression analysis, and adjusted P values (P_{adj}) were calculated using DESeq2 (v.1.20.041).

Pathway enrichment analysis

Gene Ontology (GO) term and Wikipathways enrichment analysis was performed using WebGestalt (WEB-based Gene SeT AnaLysis Toolkit) using the over-representation analysis (ORA) method (Liao et al., 2019).

Lipidomics

Lipostar software (Molecular Discovery) was used for feature detection, noise and artifact reduction, alignment, normalization and lipid identification. For each lipid, the $\log_2$-fold change and a significance P value by t-test were determined by comparing the abundances of that lipid in WT and *PSAP* KO neurons (samples in triplicates). The Benjamini-Hochberg (BH) method was used to correct for multiple hypothesis testing.

REFERENCE

Adamson, B., Norman, T.M., Jost, M., Cho, M.Y., Nuñez, J.K., Chen, Y., Villalta, J.E., Gilbert, L.A., Horlbeck, M.A., Hein, M.Y., et al. (2016). A Multiplexed Single-Cell CRISPR Screening Platform Enables Systematic Dissection of the Unfolded Protein Response. Cell *167*, 1867-1882.e21.

Anzalone, A.V., Randolph, P.B., Davis, J.R., Sousa, A.A., Koblan, L.W., Levy, J.M., Chen, P.J., Wilson, C., Newby, G.A., Raguram, A., et al. (2019). Search-and-replace genome editing without double-strand breaks or donor DNA. Nature *576*, 149–157.

Bánfi, B., Molnár, G., Maturana, A., Steger, K., Hegedûs, B., Demaurex, N., and Krause, K.H. (2001). A Ca(2+)-activated NADPH oxidase in testis, spleen, and lymph nodes. J. Biol. Chem. *276*, 37594–37601.

Bankoglu, E.E., Tschopp, O., Schmitt, J., Burkard, P., Jahn, D., Geier, A., and Stopper, H. (2016). Role of PTEN in Oxidative Stress and DNA Damage in the Liver of Whole-Body Pten Haplodeficient Mice. PLoS ONE *11*, e0166956.

Bardella, C., Olivero, M., Lorenzato, A., Geuna, M., Adam, J., O'Flaherty, L., Rustin, P., Tomlinson, I., Pollard, P.J., and Di Renzo, M.F. (2012). Cells lacking the fumarase tumor suppressor are protected from apoptosis through a hypoxia-inducible factor-independent, AMPK-dependent mechanism. Mol. Cell. Biol. *32*, 3081–3094.

Barnham, K.J., Masters, C.L., and Bush, A.I. (2004). Neurodegenerative diseases and

oxidative stress. Nat. Rev. Drug Discov. *3*, 205–214.

Bartz, F., Kern, L., Erz, D., Zhu, M., Gilbert, D., Meinhof, T., Wirkner, U., Erfle, H., Muckenthaler, M., Pepperkok, R., et al. (2009). Identification of cholesterol-regulating genes by targeted RNAi screening. Cell Metab. *10*, 63–75.

Bazan, N.G. (2005). Lipid signaling in neural plasticity, brain repair, and neuroprotection. Mol. Neurobiol. *32*, 89–103.

Bian, J.-T., Zhao, H.-L., Zhang, Z.-X., Bi, X.-H., and Zhang, J.-W. (2008). Association of NAD(P)H:quinone oxidoreductase 1 polymorphism and Alzheimer's disease in Chinese. J. Mol. Neurosci. *34*, 235–240.

Bogdan, A.R., Miyazawa, M., Hashimoto, K., and Tsuji, Y. (2016). Regulators of iron homeostasis: new players in metabolism, cell death, and disease. Trends Biochem. Sci. *41*, 274–286.

Boutry, M., Branchu, J., Lustremant, C., Pujol, C., Pernelle, J., Matusiak, R., Seyer, A., Poirel, M., Chu-Van, E., Pierga, A., et al. (2018). Inhibition of Lysosome Membrane Recycling Causes Accumulation of Gangliosides that Contribute to Neurodegeneration. Cell Rep. *23*, 3813–3826.

Chang, D., Nalls, M.A., Hallgrímsdóttir, I.B., Hunkapiller, J., van der Brug, M., Cai, F., International Parkinson's Disease Genomics Consortium, 23andMe Research Team, Kerchner, G.A., Ayalon, G., et al. (2017). A meta-analysis of genome-wide association studies identifies 17 new Parkinson's disease risk loci. Nat. Genet. *49*, 1511–1516.

Chen, J.A., Wang, Q., Davis-Turak, J., Li, Y., Karydas, A.M., Hsu, S.C., Sears, R.L., Chatzopoulou, D., Huang, A.Y., Wojta, K.J., et al. (2015). A multiancestral genome-wide exome array study of Alzheimer disease, frontotemporal dementia, and progressive supranuclear palsy. JAMA Neurol. *72*, 414–422.

Chen, X., Rzhetskaya, M., Kareva, T., Bland, R., During, M.J., Tank, A.W., Kholodilov, N., and Burke, R.E. (2008). Antiapoptotic and trophic effects of dominant-negative forms of dual leucine zipper kinase in dopamine neurons of the substantia nigra in vivo. J. Neurosci. *28*, 672–680.

Cipolla, C.M., and Lodhi, I.J. (2017). Peroxisomal Dysfunction in Age-Related Diseases. Trends Endocrinol. Metab. *28*, 297–308.

Colacurcio, D.J., and Nixon, R.A. (2016). Disorders of lysosomal acidification-The emerging role of v-ATPase in aging and neurodegenerative disease. Ageing Res. Rev. *32*, 75–88.

Delgado-Camprubi, M., Esteras, N., Soutar, M.P., Plun-Favreau, H., and Abramov, A.Y. (2017). Deficiency of Parkinson's disease-related gene Fbxo7 is associated with impaired mitochondrial metabolism by PARP activation. Cell Death Differ. *24*, 120–131.

Doll, S., Proneth, B., Tyurina, Y.Y., Panzilius, E., Kobayashi, S., Ingold, I., Irmler, M., Beckers, J., Aichler, M., Walch, A., et al. (2017). ACSL4 dictates ferroptosis sensitivity by shaping cellular lipid composition. Nat. Chem. Biol. *13*, 91–98.

Dong, X.-P., Cheng, X., Mills, E., Delling, M., Wang, F., Kurz, T., and Xu, H. (2008). The

type IV mucolipidosis-associated protein TRPML1 is an endolysosomal iron release channel. Nature *455*, 992–996.

Dubreuil, M.M., Morgens, D.W., Okumoto, K., Honsho, M., Contrepois, K., Lee-McMullen, B., Traber, G.M., Sood, R.S., Dixon, S.J., Snyder, M.P., et al. (2020). Systematic Identification of Regulators of Oxidative Stress Reveals Non-canonical Roles for Peroxisomal Import and the Pentose Phosphate Pathway. Cell Rep. *30*, 1417-1433.e7.

Edens, B.M., Vissers, C., Su, J., Arumugam, S., Xu, Z., Shi, H., Miller, N., Rojas Ringeling, F., Ming, G.-L., He, C., et al. (2019). FMRP Modulates Neural Differentiation through m6A-Dependent mRNA Nuclear Export. Cell Rep. *28*, 845-854.e5.

Filomeni, G., De Zio, D., and Cecconi, F. (2015). Oxidative stress and autophagy: the clash between damage and metabolic needs. Cell Death Differ. *22*, 377–388.

Finkel, T., and Holbrook, N.J. (2000). Oxidants, oxidative stress and the biology of ageing. Nature *408*, 239–247.

Gallagher, M.D., and Chen-Plotkin, A.S. (2018). The Post-GWAS Era: From Association to Function. Am. J. Hum. Genet. *102*, 717–730.

Gao, S., Yan, L., Wang, R., Li, J., Yong, J., Zhou, X., Wei, Y., Wu, X., Wang, X., Fan, X., et al. (2018). Tracing the temporal-spatial transcriptome landscapes of the human fetal digestive tract using single-cell RNA-sequencing. Nat. Cell Biol. *20*, 721–734.

Gilbert, L.A., Horlbeck, M.A., Adamson, B., Villalta, J.E., Chen, Y., Whitehead, E.H., Guimaraes, C., Panning, B., Ploegh, H.L., Bassik, M.C., et al. (2014). Genome-scale CRISPR-mediated control of gene repression and activation. Cell *159*, 647–661.

Glaros, E.N., Kim, W.S., Quinn, C.M., Wong, J., Gelissen, I., Jessup, W., and Garner, B. (2005). Glycosphingolipid accumulation inhibits cholesterol efflux via the ABCA1/apolipoprotein A-I pathway: 1-phenyl-2-decanoylamino-3-morpholino-1-propanol is a novel cholesterol efflux accelerator. J. Biol. Chem. *280*, 24515–24523.

Grubman, A., Pollari, E., Duncan, C., Caragounis, A., Blom, T., Volitakis, I., Wong, A., Cooper, J., Crouch, P.J., Koistinaho, J., et al. (2014). Deregulation of biometal homeostasis: the missing link for neuronal ceroid lipofuscinoses? Metallomics *6*, 932–943.

Gu, C., Chen, C., Wu, R., Dong, T., Hu, X., Yao, Y., and Zhang, Y. (2018). Long Noncoding RNA EBF3-AS Promotes Neuron Apoptosis in Alzheimer's Disease. DNA Cell Biol. *37*, 220–226.

Guerrero-Gómez, D., Mora-Lorca, J.A., Sáenz-Narciso, B., Naranjo-Galindo, F.J., Muñoz-Lobato, F., Parrado-Fernández, C., Goikolea, J., Cedazo-Minguez, Á., Link, C.D., Neri, C., et al. (2019). Loss of glutathione redox homeostasis impairs proteostasis by inhibiting autophagy-dependent protein degradation. Cell Death Differ. *26*, 1545–1565.

Hallett, P.J., Engelender, S., and Isacson, O. (2019). Lipid and immune abnormalities causing age-dependent neurodegeneration and Parkinson's disease. J. Neuroinflammation *16*, 153.

Han, C., Liu, Y., Dai, R., Ismail, N., Su, W., and Li, B. (2020a). Ferroptosis and its potential role in human diseases. Front. Pharmacol. *11*, 239.

Han, X., Zhou, Z., Fei, L., Sun, H., Wang, R., Chen, Y., Chen, H., Wang, J., Tang, H., Ge, W., et al. (2020b). Construction of a human cell landscape at single-cell level. Nature.

Harbison, R.D., Dwivedi, C., and Evans, M.A. (1976). A proposed mechanism for trimethylphosphate-induced sterility. Toxicol. Appl. Pharmacol. *35*, 481–490.

Hart, T., Tong, A.H.Y., Chan, K., Van Leeuwen, J., Seetharaman, A., Aregger, M., Chandrashekhar, M., Hustedt, N., Seth, S., Noonan, A., et al. (2017). Evaluation and Design of Genome-Wide CRISPR/SpCas9 Knockout Screens. G3 (Bethesda) *7*, 2719–2727.

Hauser, M., Yan, R., Li, W., Repina, N.A., Schaffer, D.V., and Xu, K. (2018). The Spectrin-Actin-Based Periodic Cytoskeleton as a Conserved Nanoscale Scaffold and Ruler of the Neural Stem Cell Lineage. Cell Rep. *24*, 1512–1522.

Hiraiwa, M., Martin, B.M., Kishimoto, Y., Conner, G.E., Tsuji, S., and O'Brien, J.S. (1997). Lysosomal proteolysis of prosaposin, the precursor of saposins (sphingolipid activator proteins): its mechanism and inhibition by ganglioside. Arch. Biochem. Biophys. *341*, 17–24.

Hocsak, E., Szabo, V., Kalman, N., Antus, C., Cseh, A., Sumegi, K., Eros, K., Hegedus, Z., Gallyas, F., Sumegi, B., et al. (2017). PARP inhibition protects mitochondria and reduces ROS production via PARP-1-ATF4-MKP-1-MAPK retrograde pathway. Free Radic. Biol. Med. *108*, 770–784.

Horlbeck, M.A., Gilbert, L.A., Villalta, J.E., Adamson, B., Pak, R.A., Chen, Y., Fields, A.P., Park, C.Y., Corn, J.E., Kampmann, M., et al. (2016). Compact and highly active next-generation libraries for CRISPR-mediated gene repression and activation. Elife *5*.

Huang, B., Wang, W., Bates, M., and Zhuang, X. (2008). Three-dimensional super-resolution imaging by stochastic optical reconstruction microscopy. Science *319*, 810–813.

Ihry, R.J., Salick, M.R., Ho, D.J., Sondey, M., Kommineni, S., Paula, S., Raymond, J., Henry, B., Frias, E., Wang, Q., et al. (2019). Genome-Scale CRISPR Screens Identify Human Pluripotency-Specific Genes. Cell Rep. *27*, 616-630.e6.

Imaizumi, Y., Okada, Y., Akamatsu, W., Koike, M., Kuzumaki, N., Hayakawa, H., Nihira, T., Kobayashi, T., Ohyama, M., Sato, S., et al. (2012). Mitochondrial dysfunction associated with increased oxidative stress and α-synuclein accumulation in PARK2 iPSC-derived neurons and postmortem brain tissue. Mol. Brain *5*, 35.

Jain, I.H., Calvo, S.E., Markhard, A.L., Skinner, O.S., To, T.-L., Ast, T., and Mootha, V.K. (2020). Genetic screen for cell fitness in high or low oxygen highlights mitochondrial and lipid metabolism. Cell *181*, 716-727.e11.

Julien, J.P., and Mushynski, W.E. (1998). Neurofilaments in health and disease. Prog. Nucleic Acid Res. Mol. Biol. *61*, 1–23.

Kim, G.H., Kim, J.E., Rhie, S.J., and Yoon, S. (2015). The role of oxidative stress in neurodegenerative diseases. Exp. Neurobiol. *24*, 325–340.

Kügler, S., Straten, G., Kreppel, F., Isenmann, S., Liston, P., and Bähr, M. (2000). The X-linked inhibitor of apoptosis (XIAP) prevents cell death in axotomized CNS neurons in vivo. Cell Death Differ. *7*, 815–824.

Lake, B.B., Chen, S., Sos, B.C., Fan, J., Kaeser, G.E., Yung, Y.C., Duong, T.E., Gao, D., Chun, J., Kharchenko, P.V., et al. (2018). Integrative single-cell analysis of transcriptional and epigenetic states in the human adult brain. Nat. Biotechnol. *36*, 70–80.

Langfelder, P., and Horvath, S. (2008). WGCNA: an R package for weighted correlation network analysis. BMC Bioinformatics *9*, 559.

Langmead, B., Trapnell, C., Pop, M., and Salzberg, S.L. (2009). Ultrafast and memory-efficient alignment of short DNA sequences to the human genome. Genome Biol. *10*, R25.

Le Pichon, C.E., Meilandt, W.J., Dominguez, S., Solanoy, H., Lin, H., Ngu, H., Gogineni, A., Sengupta Ghosh, A., Jiang, Z., Lee, S.-H., et al. (2017). Loss of dual leucine zipper kinase signaling is protective in animal models of neurodegenerative disease. Sci. Transl. Med. *9*.

Liao, Y., Wang, J., Jaehnig, E.J., Shi, Z., and Zhang, B. (2019). WebGestalt 2019: gene

set analysis toolkit with revamped UIs and APIs. Nucleic Acids Res. *47*, W199–W205.

Lin, M.T., and Beal, M.F. (2006). Mitochondrial dysfunction and oxidative stress in neurodegenerative diseases. Nature *443*, 787–795.

Li, J., Cao, F., Yin, H.-L., Huang, Z.-J., Lin, Z.-T., Mao, N., Sun, B., and Wang, G. (2020). Ferroptosis: past, present and future. Cell Death Dis. *11*, 88.

Li, M., Zhao, X., Wang, W., Shi, H., Pan, Q., Lu, Z., Perez, S.P., Suganthan, R., He, C., Bjørås, M., et al. (2018). Ythdf2-mediated m6A mRNA clearance modulates neural development in mice. Genome Biol. *19*, 69.

Luu, B., Ellisor, D., and Zervas, M. (2011). The lineage contribution and role of Gbx2 in spinal cord development. PLoS ONE *6*, e20940.

Mair, B., Tomic, J., Masud, S.N., Tonge, P., Weiss, A., Usaj, M., Tong, A.H.Y., Kwan, J.J., Brown, K.R., Titus, E., et al. (2019). Essential gene profiles for human pluripotent stem cells identify uncharacterized genes and substrate dependencies. Cell Rep. *27*, 599-615.e12.

Martinez-Morales, P.L., Quiroga, A.C., Barbas, J.A., and Morales, A.V. (2010). SOX5 controls cell cycle progression in neural progenitors by interfering with the WNT-beta-catenin pathway. EMBO Rep. *11*, 466–472.

Mathys, H., Davila-Velderrain, J., Peng, Z., Gao, F., Mohammadi, S., Young, J.Z., Menon, M., He, L., Abdurrob, F., Jiang, X., et al. (2019). Single-cell transcriptomic analysis of Alzheimer's disease. Nature *570*, 332–337.

Ma, Q. (2013). Role of nrf2 in oxidative stress and toxicity. Annu. Rev. Pharmacol. Toxicol. *53*, 401–426.

Méndez-Gómez, H.R., and Vicario-Abejón, C. (2012). The homeobox gene Gsx2 regulates the self-renewal and differentiation of neural stem cells and the cell fate of postnatal progenitors. PLoS ONE *7*, e29799.

Mochizuki, Y., Park, M.K., Mori, T., and Kawashima, S. (1995). The difference in autofluorescence features of lipofuscin between brain and adrenal. Zool. Sci. *12*, 283–288.

van Muiswinkel, F.L., de Vos, R.A.I., Bol, J.G.J.M., Andringa, G., Jansen Steur, E.N.H., Ross, D., Siegel, D., and Drukarch, B. (2004). Expression of NAD(P)H:quinone oxidoreductase in the normal and Parkinsonian substantia nigra. Neurobiol. Aging *25*, 1253–1262.

Muraro, M.J., Dharmadhikari, G., Grün, D., Groen, N., Dielen, T., Jansen, E., van Gurp, L., Engelse, M.A., Carlotti, F., de Koning, E.J.P., et al. (2016). A Single-Cell Transcriptome Atlas of the Human Pancreas. Cell Syst. *3*, 385-394.e3.

Muto, Y., Nishiyama, M., Nita, A., Moroishi, T., and Nakayama, K.I. (2017). Essential role of FBXL5-mediated cellular iron homeostasis in maintenance of hematopoietic stem cells. Nat. Commun. *8*, 16114.

Nacarelli, T., Azar, A., and Sell, C. (2014). Inhibition of mTOR Prevents ROS Production Initiated by Ethidium Bromide-Induced Mitochondrial DNA Depletion. Front Endocrinol (Lausanne) *5*, 122.

Ndayisaba, A., Kaindlstorfer, C., and Wenning, G.K. (2019). Iron in Neurodegeneration - Cause or Consequence? Front. Neurosci. *13*, 180.

Niedzielska, E., Smaga, I., Gawlik, M., Moniczewski, A., Stankowicz, P., Pera, J., and Filip, M. (2016). Oxidative stress in neurodegenerative diseases. Mol. Neurobiol. *53*, 4094–4125.

Ou, Y., Wang, S.-J., Li, D., Chu, B., and Gu, W. (2016). Activation of SAT1 engages polyamine metabolism with p53-mediated ferroptotic responses. Proc Natl Acad Sci USA *113*, E6806–E6812.

Patel, M. (2016). Targeting oxidative stress in central nervous system disorders. Trends Pharmacol. Sci. *37*, 768–778.

Puri, V., Jefferson, J.R., Singh, R.D., Wheatley, C.L., Marks, D.L., and Pagano, R.E. (2003). Sphingolipid storage induces accumulation of intracellular cholesterol by stimulating SREBP-1 cleavage. J. Biol. Chem. *278*, 20961–20970.

Raina, A.K., Templeton, D.J., Deak, J.C., Perry, G., and Smith, M.A. (1999). Quinone reductase (NQO1), a sensitive redox indicator, is increased in Alzheimer's disease. Redox Rep. *4*, 23–27.

Ramsey, C.P., Glass, C.A., Montgomery, M.B., Lindl, K.A., Ritson, G.P., Chia, L.A., Hamilton, R.L., Chu, C.T., and Jordan-Sciutto, K.L. (2007). Expression of Nrf2 in neurodegenerative diseases. J. Neuropathol. Exp. Neurol. *66*, 75–85.

Reczek, C.R., Birsoy, K., Kong, H., Martínez-Reyes, I., Wang, T., Gao, P., Sabatini, D.M., and Chandel, N.S. (2017). A CRISPR screen identifies a pathway required

for paraquat-induced cell death. Nat. Chem. Biol. *13*, 1274–1279.

Reho, J.J., Guo, D.-F., and Rahmouni, K. (2019). Mechanistic target of rapamycin complex 1 signaling modulates vascular endothelial function through reactive oxygen species. J. Am. Heart Assoc. *8*, e010662.

van Roermund, C.W., Hettema, E.H., Kal, A.J., van den Berg, M., Tabak, H.F., and Wanders, R.J. (1998). Peroxisomal beta-oxidation of polyunsaturated fatty acids in Saccharomyces cerevisiae: isocitrate dehydrogenase provides NADPH for reduction of double bonds at even positions. EMBO J. *17*, 677–687.

Rosengren, L.E., Karlsson, J.E., Karlsson, J.O., Persson, L.I., and Wikkelsø, C. (1996). Patients with amyotrophic lateral sclerosis and other neurodegenerative diseases have increased levels of neurofilament protein in CSF. J. Neurochem. *67*, 2013–2018.

Ross, D., and Siegel, D. (2017). Functions of NQO1 in cellular protection and coq10 metabolism and its potential role as a redox sensitive molecular switch. Front. Physiol. *8*, 595.

Rouault, T.A. (2013). Iron metabolism in the CNS: implications for neurodegenerative diseases. Nat. Rev. Neurosci. *14*, 551–564.

Sandhoff, K., and Harzer, K. (2013). Gangliosides and gangliosidoses: principles of molecular and metabolic pathogenesis. J. Neurosci. *33*, 10195–10208.

SantaCruz, K.S., Yazlovitskaya, E., Collins, J., Johnson, J., and DeCarli, C. (2004). Regional NAD(P)H:quinone oxidoreductase activity in Alzheimer's disease.

Neurobiol. Aging *25*, 63–69.

Schmitt-John, T., Drepper, C., Mussmann, A., Hahn, P., Kuhlmann, M., Thiel, C., Hafner, M., Lengeling, A., Heimann, P., Jones, J.M., et al. (2005). Mutation of Vps54 causes motor neuron disease and defective spermiogenesis in the wobbler mouse. Nat. Genet. *37*, 1213–1215.

Schulz, A., Sekine, Y., Oyeyemi, M.J., Abrams, A.J., Basavaraju, M., Han, S.M., Groth, M., Morrison, H., Strittmatter, S.M., and Hammarlund, M. (2020). The stress-responsive gene GDPGP1/mcp-1 regulates neuronal glycogen metabolism and survival. J. Cell Biol. *219*.

Seibler, P., Burbulla, L.F., Dulovic, M., Zittel, S., Heine, J., Schmidt, T., Rudolph, F., Westenberger, A., Rakovic, A., Münchau, A., et al. (2018). Iron overload is accompanied by mitochondrial and lysosomal dysfunction in WDR45 mutant cells. Brain *141*, 3052–3064.

Shen, L., and Jia, J. (2016). An Overview of Genome-Wide Association Studies in Alzheimer's Disease. Neurosci. Bull. *32*, 183–190.

Shin, Y.J., Cho, D.Y., Chung, T.Y., Han, S.B., Hyon, J.Y., and Wee, W.R. (2011). Rapamycin reduces reactive oxygen species in cultured human corneal endothelial cells. Curr. Eye Res. *36*, 1116–1122.

Sies, H., Berndt, C., and Jones, D.P. (2017). Oxidative Stress. Annu. Rev. Biochem. *86*, 715–748.

Slowik, A., Tomik, B., Wolkow, P.P., Partyka, D., Turaj, W., Malecki, M.T., Pera, J.,

Dziedzic, T., Szczudlik, A., and Figlewicz, D.A. (2006). Paraoxonase gene polymorphisms and sporadic ALS. Neurology *67*, 766–770.

Sudarshan, S., Sourbier, C., Kong, H.-S., Block, K., Valera Romero, V.A., Yang, Y., Galindo, C., Mollapour, M., Scroggins, B., Goode, N., et al. (2009). Fumarate hydratase deficiency in renal cancer induces glycolytic addiction and hypoxia-inducible transcription factor 1alpha stabilization by glucose-dependent generation of reactive oxygen species. Mol. Cell. Biol. *29*, 4080–4090.

Terman, A., and Brunk, U.T. (1998). Lipofuscin: mechanisms of formation and increase with age. APMIS *106*, 265–276.

Terman, A., and Brunk, U.T. (2004). Lipofuscin. Int. J. Biochem. Cell Biol. *36*, 1400–1404.

Tian, R., Gachechiladze, M.A., Ludwig, C.H., Laurie, M.T., Hong, J.Y., Nathaniel, D., Prabhu, A.V., Fernandopulle, M.S., Patel, R., Abshari, M., et al. (2019). CRISPR Interference-Based Platform for Multimodal Genetic Screens in Human iPSC-Derived Neurons. Neuron *104*, 239-255.e12.

Tsang, A.H.K., Lee, Y.-I., Ko, H.S., Savitt, J.M., Pletnikova, O., Troncoso, J.C., Dawson, V.L., Dawson, T.M., and Chung, K.K.K. (2009). S-nitrosylation of XIAP compromises neuronal survival in Parkinson's disease. Proc Natl Acad Sci USA *106*, 4900–4905.

Unsain, N., Higgins, J.M., Parker, K.N., Johnstone, A.D., and Barker, P.A. (2013). XIAP regulates caspase activity in degenerating axons. Cell Rep. *4*, 751–763.

Wang, Y., Santa-Cruz, K., DeCarli, C., and Johnson, J.A. (2000). NAD(P)H:quinone oxidoreductase activity is increased in hippocampal pyramidal neurons of patients with Aalzheimer's disease. Neurobiol. Aging *21*, 525–531.

Wan, W., You, Z., Zhou, L., Xu, Y., Peng, C., Zhou, T., Yi, C., Shi, Y., and Liu, W. (2018). mTORC1-Regulated and HUWE1-Mediated WIPI2 Degradation Controls Autophagy Flux. Mol. Cell *72*, 303-315.e6.

Ward, D.M., and Cloonan, S.M. (2019). Mitochondrial iron in human health and disease. Annu. Rev. Physiol. *81*, 453–482.

Ward, M.E., Chen, R., Huang, H.-Y., Ludwig, C., Telpoukhovskaia, M., Taubes, A., Boudin, H., Minami, S.S., Reichert, M., Albrecht, P., et al. (2017). Individuals with progranulin haploinsufficiency exhibit features of neuronal ceroid lipofuscinosis. Sci. Transl. Med. *9*.

Weber, R.A., Yen, F.S., Nicholson, S.P.V., Alwaseem, H., Bayraktar, E.C., Alam, M., Timson, R.C., La, K., Abu-Remaileh, M., Molina, H., et al. (2020). Maintaining iron homeostasis is the key role of lysosomal acidity for cell proliferation. Mol. Cell *77*, 645-655.e7.

Welsbie, D.S., Yang, Z., Ge, Y., Mitchell, K.L., Zhou, X., Martin, S.E., Berlinicke, C.A., Hackler, L., Fuller, J., Fu, J., et al. (2013). Functional genomic screening identifies dual leucine zipper kinase as a key mediator of retinal ganglion cell death. Proc Natl Acad Sci USA *110*, 4045–4050.

Weltner, J., Balboa, D., Katayama, S., Bespalov, M., Krjutškov, K., Jouhilahti, E.-M.,

Trokovic, R., Kere, J., and Otonkoski, T. (2018). Human pluripotent reprogramming with CRISPR activators. Nat. Commun. *9*, 2643.

Wolf, F.A., Angerer, P., and Theis, F.J. (2018). SCANPY: large-scale single-cell gene expression data analysis. Genome Biol. *19*, 15.

Xu, D., Bureau, Y., McIntyre, D.C., Nicholson, D.W., Liston, P., Zhu, Y., Fong, W.G., Crocker, S.J., Korneluk, R.G., and Robertson, G.S. (1999). Attenuation of ischemia-induced cellular and behavioral deficits by X chromosome-linked inhibitor of apoptosis protein overexpression in the rat hippocampus. J. Neurosci. *19*, 5026–5033.

Yadav, R.S., and Tiwari, N.K. (2014). Lipid integration in neurodegeneration: an overview of Alzheimer's disease. Mol. Neurobiol. *50*, 168–176.

Yan, Y., and Finkel, T. (2017). Autophagy as a regulator of cardiovascular redox homeostasis. Free Radic. Biol. Med. *109*, 108–113.

Yilmaz, A., Peretz, M., Aharony, A., Sagi, I., and Benvenisty, N. (2018). Defining essential genes for human pluripotent stem cells by CRISPR-Cas9 screening in haploid cells. Nat. Cell Biol. *20*, 610–619.

Yuan, H., Li, X., Zhang, X., Kang, R., and Tang, D. (2016). Identification of ACSL4 as a biomarker and contributor of ferroptosis. Biochem. Biophys. Res. Commun. *478*, 1338–1343.

Zhao, L.Y., Niu, Y., Santiago, A., Liu, J., Albert, S.H., Robertson, K.D., and Liao, D. (2006). An EBF3-mediated transcriptional program that induces cell cycle arrest

and apoptosis. Cancer Res. *66*, 9445–9452.

Yang X, Scheid S, Lottaz C (2020). OrderedList: Similarities of Ordered Gene Lists. R package version 1.59.1

Publishing Agreement

It is the policy of the University to encourage open access and broad distribution of all theses, dissertations, and manuscripts. The Graduate Division will facilitate the distribution of UCSF theses, dissertations, and manuscripts to the UCSF Library for open access and distribution. UCSF will make such theses, dissertations, and manuscripts accessible to the public and will take reasonable steps to preserve these works in perpetuity.

I hereby grant the non-exclusive, perpetual right to The Regents of the University of California to reproduce, publicly display, distribute, preserve, and publish copies of my thesis, dissertation, or manuscript in any form or media, now existing or later derived, including access online for teaching, research, and public service purposes.

DocuSigned by:
Tian, Ruilin
ADF407655DCD4CE...
Author Signature

6/1/2020
Date